Sea-ice strength and internal stresses from in-situ measurements

Yukie Hata

Doctor of Philosophy

Department of Atmospheric and Oceanic Science

McGill University
Montréal, Québec
December 2017

A thesis submitted to McGill University in Partial fulfillment of the requirements of the degree of Doctor of Philosophy

Acknowledgment

I would love to thank everyone who has helped me getting where I am today. Special thanks go to Bruno Tremblay, who facilitates, animates, accompanies, and inspires me. I am grateful for his patience, honesty, joyfulness, open mind, and critical thinking. This work would never have been finished without his encouragements, insights, advices, and supports. Comments and feedback from Jacqueline Richter-Mange, Jennifer Hutchings, Bob Newton, Frédéric Dupont, Adrienne Tivy, and several anonymous reviewers are appreciated and were very helpful.

Over the last six years, I spend time with amazing people who make me grow and learn important lessons both in academic and personal. I thank them all for making my time at McGill University fruitful and helping me go through difficult moments. Special thanks go to Olivier Asselin, Mathieu Plant, Line Bourdages, and James Williams for their time for so many interesting discussions on something related to our researches and on something not related to the researches at all, to Patricia DeRepentigny, Mathilde Jutras, Amélie Bouchat, and Charles Brunette for making the lunch time at McGill merrier, and their advice and help.

Financial supports from the ArcTrain Canada (funded by Natural Sciences and Engineering Research Council of Canada, NSERC), Québec-Océan, and CanSISE (Canadian Sea Ice and Snow Evolution Network) are gratefully acknowledged. I also thank Ferring Pharmaceuticala for the generous grant that made the buoys deployments possible.

I also thank my dear friends, Sujaya Neupane, Andrea Salguero, Munirih Campbell, Lorraine Pritchard, Stan Phillips, and Emiko Murakami for cooking me warm comforting meals, uplifted conversations, and encouraging me to keep going when I struggled with the research and life in general. I am grateful for the support of my parents, who always keep me in their mind and lower my stress level by listening me. I could not have finished writing this thesis without them providing me a psychologically healthy and safe atmosphere through their relaxed and warm characters.

Abstract

A knowledge of sea-ice dynamics is key to achieving proper Arctic climate simulations. The goal of this thesis is to lay the foundation for a three-dimensional ice dynamics model that considers both thermal and dynamic stresses. This thesis presents in-situ observations from buoys deployed in the Canadian Arctic Archipelago (CAA). In the CAA, the sea ice is landfast for approximately six months in winter. In a first step, we have analyzed in-situ data from a sea-ice stress buoy deployed in the Viscount Melville Sound. Results demonstrate that thermal stress is the dominant source of internal stress in the CAA with few short-lived important dynamic stress events caused by ice floe collisions in the free drift season prior to the landfast season. This is in contrast with similar internal sea-ice stress measurements made in the Arctic Ocean, in which both dynamic and thermal stresses are of similar magnitude. Prior to landfast ice onset, the thermal stresses are isotropic, as hypothesized in prior analyses of ice internal stress data measured in the Arctic Ocean. After landfast ice onset, however, the thermal stresses become anisotropic. Results from the buoy data, together with results from a 1.5D thermal stress model (forced with simulated internal sea-ice temperatures), demonstrate that the anisotropy in thermal stress arises from land confinement induced by the coastline in the direction of the short-axis of the channel. Results from the model are in good agreement with the observed stress in the direction of both principal stresses. They suggest that anisotropy in thermal stress could impact the mode of failure of sea ice in the CAA. The results also suggest that viscous creep stress relaxation is important and acts on time scale of several days, which is longer than the time scale (several hours) suggested from the previous measurements. In a second step, we derive estimates of the sea-ice compressive strength parameter (P^*) based on a simple force balance and known external forcing (surface air-ice and ice-ocean stresses) and whether sea ice drifts under the action of these external loads or not. Results from a proof of concept experiment using internally consistent data from a fully coupled ice-ocean model (the Regional Ice Operation Prediction System, RIOPS) demonstrate that it is indeed possible to estimate P^*, which is a known quantity in the model, from the simple force balance presented. When the same method is applied to in-situ observations and reanalysis data, the method only produces meaningful bounds of P^* ($= 94.4 \pm 4.4$ kN/m^2) when the pack ice is mostly composed of first-year ice with little multi-year ice present. This P^* estimate is approximately three times the value currently used in the modelling community. This highlights the fact that the ice drift measured at a point may not be representative of the ice behaviour on average in a region. For instance, results suggest that larger tidal ocean currents in the region are enough to prevent a landfast ice cover to develop locally while the pack ice is mostly landfast on larger scales. The failures of the method when it is applied to some buoy data also suggest that there may be error in the surface forcing from the CGRF (Canadian Meteorological Center's Global Deterministic Prediction System Reforecast). The analysis of these errors is left for future work. Results discussed in this thesis highlight the importance of thermal stresses in sea-ice models. The only forcing required by a thermal stress model is the internal temperature profile. Therefore, a thermal stress model could be implemented in current sea-ice thermodynamic models with a little effort. It would then be coupled with the dynamical part of the model by developing yield criteria for ice failure that are a function of the total (dynamical and thermal) stresses at a point rather than the depth average internal stress as currently done in the community.

Abrégé

Cette thèse présente l'analyse d'observations enregistrées par des bouées déployées dans l'Archipel Arctique Canadien (AAC), où la glace de mer consiste en un couvert de glace de rive pendant approximativement six mois par année. En premier lieu, les contraintes internes enregistrées sur place par une bouée déployée dans le détroit du Vicomte de Melville sont analysées. Cette étude démontre que les contraintes thermiques dominent les forces internes de la banquise dans l'AAC, et ce malgré la présence de quelques évènements où de fortes contraintes dynamiques de courte durée (occasionnées par la collision de morceaux de banquise durant la période de dérive) ont été enregistrées. Ces résultats diffèrent des observations obtenues par des bouées similaires déployées dans l'océan Arctique, qui indiquent plutôt une équivalence en magnitude entre les contraintes de source thermique et de source dynamique. Pendant la période de dérive, les contraintes thermiques mesurées dans l'AAC présentent une isotropie qui concorde avec les analyses pour l'océan Arctique. Les contraintes thermiques deviennent cependant anisotropes après la transition vers le régime de glace de rive. En combinant ces résultats avec des simulations provenant d'un modèle de glace à 1.5 dimensions forcé avec des températures internes simulées, il est démontré que cette anisotropie découle du confinement de la glace de rive par les berges du chenal. Les contraintes simulées par le modèle, dans chacun des axes principaux, concordent bien avec celles observées par les bouées. Les résultats de cette étude suggèrent que le mode de fracture de la glace de rive dans l'AAC peut être affecté par l'anisotropie des contraintes thermiques. De plus, il est observé que la relaxation visqueuse des contraintes due au fluage de la glace ne devient importante que sur une échelle temporelle de l'ordre de plusieurs jours, ce qui est plus long que l'ordre suggéré par les mesures en laboratoire (quelques heures). En second lieu, nous avons obtenu des valeurs approximatives pour le paramètre de résistance à la compression de la glace de mer (P^*) à partir de l'équilibre des forces, en se basant sur l'état observé de la dérive de la glace (dérive ou glace de rive) et en utilisant un forçage (friction aux interfaces glaceatmosphère et glace-océan) connu. Afin de démontrer qu'il est possible de déterminer P^* à partir du simple équilibre des forces, la méthode proposée est appliquée sur les données d'un modèle de glace entièrement couplé à l'océan (Regional Ice Operation Prediction System, RIOPS), dans lequel P^* est une variable connue. En appliquant cette méthode sur les données d'observations et de réanalyses, des limites physiques sont établies pour restreinte la plage de valeur de P^* ($= 94.4 \pm 4.4$ kN/m^2) lorsque la glace est composée principalement de glace annuelle. Cette plage de valeur correspond approximativement au triple de la valeur couramment utilisée dans la communauté de modélisation. Les résultats cette étude suggèrent que les mesures de dérive à un point précis peuvent ne pas correspondre au comportement moyen de la glace dans une région. Par exemple, il est montré que dans une région principalement recouverte de glace de rive, la présence de courants de marée plus forts peut être suffisante pour prévenir le développement de la glace de rive localement. Dans le cas de certaines bouées, l'échec de la méthode proposée suggère la présence d'erreurs dans les forçage de surface du CGRF (Canadian Meteorological Center's Global Deterministic Prediction System Reforecast), et l'analyse de ces erreurs est laissé comme projet futur. Les résultats discutés dans cette thèse soulignent l'importance des contraintes thermiques pour la modélisation de la glace de mer. Le profil de température interne de la glace étant le seul forçage nécessaire dans un modèle de contraintes thermiques, il serait possible de l'implémenter dans un modèle thermodynamique de glace de mer. Ce modèle thermodynamique pourrait ensuite être couplé à une composante dynamique par le développement de limites de contraintes en fonctions des contraintes totales (dynamiques + thermiques) en un point, plutôt qu'en fonction des contraintes internes moyennées sur l'épaisseur, comme il est couramment utilisé dans la communauté.

Contributions of authors

Chapter 2 is based on a paper published in Journal of Geophysical Research, co-authored by Prof. Bruno Tremblay. The manuscript presents the analysis of internal sea-ice stress data obtained from an ice stress buoy deployed in the Viscount Melville Sound in the Canadian Arctic Archipelago by Prof. Bruno Tremblay. I analyzed the buoy data and wrote the paper. Prof. Bruno Tremblay provided edits to the manuscript and continuous supervision during this work. Chapter 3 is based on a paper published in Journal of Geophysical Research. The paper is also co-authored by Prof. Bruno Tremblay. In this paper, we introduce a 1.5D anisotropic sigma-coordinate thermal stress model. I developed the model, performed the simulations and wrote the paper. Prof. Bruno Tremblay advised me for the research and performed throughout editing of the manuscript. Chapter 4 is based on a paper that will be submitted to Journal of Geophysical Research. It is co-authored by Prof. Bruno Tremblay and Dr. Frédéric Dupont from Environment and Climate Change Canada. In this manuscript, sea-ice drift data from buoys are used in conjunction with a fully coupled ice-ocean model in order to derive estimates of sea-ice mechanical strength. I performed the analysis and wrote the paper. Prof. Bruno Tremblay provided advises on the research and edited the manuscript. Dr. Frédéric Dupont generously shared insightful criticism and the fully coupled ice-ocean model data used in this analysis.

Statement of originality

The original contributions of this thesis are as follows:

1) In-situ internal sea-ice stress data measured by an Ice Stress Buoy deployed in the Canadian Arctic Archipelago (CAA) demonstrate that the thermal stresses in sea ice are anisotropic in winter, or landfast season. To the best of our knowledge, this is the first time that anisotropic thermal stresses have been observed in sea ice. The presence of anisotropy in internal sea-ice stresses implies that shear stresses are present in sea ice associated with surface air temperature changes. This finding challenges basic assumptions made in the community that internal thermal stresses are isotropic, and they can be removed from the total stresses to extract the internal stresses induced by dynamical stresses.

2) We demonstrate that the cause of anisotropic thermal stress is land confinement. When the ice temperature decreases and tensile stresses are induced, the magnitudes of sea-ice internal stresses are larger in the direction perpendicular to the coastline than in the direction parallel to the coastline. This suggests that land confinement is responsible for the anisotropy in thermal stress in the CAA.

3) We develop a 1.5D thermal stress model that includes the land confinement effect and allows us to simulate internal anisotropic thermal stresses. The model accurately reproduces the anisotropic thermal stresses that are observed in the CAA when the model is forced with observed air temperature. This result confirms the hypothesis that land confinement is responsible for anisotropic thermal stresses in the CAA. This model will form the basis for a 3-D sea-ice dynamic model, in which the vertical dependence of stresses with depth will be considered in the failure criterion. This will reflect a new direction for research in the sea-ice dynamics modeling community.

4) In-situ stress data reveal the presence of residual compressive stresses at the beginning of the melt season, when the sea-ice internal temperature is nearly isothermal.

The results suggest a viscous creep relaxation time scale of several days. This is supported by the 1.5D thermal stress model, which simulates well the observations when the relaxation time constant is set to eight days.

5) We estimate the geophysical sea-ice strength (P^*) from sea-ice drift data obtained in the CAA. The estimated P^* of 94.4 ± 8.8 kN/m^2 is based on the sea-ice velocity observed with one buoy, which happen to remain in a region characterized by a high correlation between ice and wind velocity (i.e. uniform ocean currents and uniform first year ice thickness are assumed). This estimated P^* is three times larger than the value commonly used in the sea-ice models (27.5 kN/m^2).

6) One buoy observes landfast onset much later in winter in 2009-2010 than the onset observed with another buoy in winter in 2013-2014. The two buoys are separated by only 10 km in a region where similar first-year ice thicknesses are simulated in both winters in 2009-2010 and 2013-20014. In fact, the buoy that observes the later landfast onset was located in a region where tidal current is believed to be stronger. Therefore, we presume that the difference in tidal current within 10 km distance is enough to keep the buoy in motion until late winter.

Contents

List of Figures

List of Tables

Chapter 1

Introduction

The presence of sea ice and snow in the Arctic has a critical impact on global climate. Sea-ice and snow cover reductions, which have been associated with anthropogenic forcing, alter surface albedo [*Curry et al.*, 1994], atmospheric and oceanic circulation via salt, moisture and heat fluxes at the ocean-ice-atmosphere boundary [*Kwok et al.*, 2013; *Overland and Wang*, 2009], and cloud cover due to weaker surface inversions or a more humid atmosphere [*Screen et al.*, 2013]. These changes are all possible causes of Arctic amplification[a], which has been observed from satellites [*Comiso*, 2003], in-situ observations [*Manabe and Stouffer*, 1996], and reanalysis datasets [*Greversen et al.*, 2008; *Screen and Simmonds*, 2010]. The presence of sea ice also impacts on ecosystems [e.g. *Arrigo et al.*, 2012; *Tynan and DeMaster*, 1997], local Inuit communities [e.g. *George et al.*, 2004], and the tourism industry [e.g. *Stewart et al.*, 2009]. These implications highlight the importance of accurately simulating sea ice for future projections.

A knowledge of sea-ice dynamics is key to achieving proper Arctic climate simulations. Firstly, the sea-ice dynamics affects the sea-ice thickness distribution and, therefore, ocean-atmosphere heat fluxes. A sea-ice model that includes dynamics will simulate thicker ice in the Lincoln and Beaufort seas and thinner ice on the Eurasian coastline due to a dominant wind pattern blowing ice away from the Eurasian continent

---

[a] warming at the high latitude is larger compared to the global average

and towards North America and Greenland [*Hibler*, 1979]. Secondly, sea ice export from the Arctic constitutes a freshwater flux into the Greenland/Iceland/Norwegian seas, where deep convection is present [*Schmith and Hansen*, 2003]. Finally, the deformation in the sea-ice fields often takes place along narrow and active leads where divergence (open water formation) or convergence (ridge building) occurs. This affects the salt, moisture, and heat fluxes between the ocean and the atmosphere and, ultimately, the ocean thermohaline circulation [*Richter-Menge et al.*, 2001].

In the seminal sea-ice dynamics model of *Coon et al.* [1974], sea ice is considered to behave as an elastic-plastic isotropic material with no bi-axial tensile strength, since sea ice is heavily fractured and opens easily in divergence (the Arctic Ice Dynamics Joint Experiment, AIDJEX). Elastic deformations are small and reversible; plastic deformations are larger and non-reversible. Elastic deformations are negligible compared to plastic deformation, yet they make the numerical treatment of the resulting governing differential equation difficult to solve. To address this, *Hibler* [1979] sought to simulate the elastic deformation in sea ice as very small deformations or creeping flow. This model is referred to as the Viscous-Plastic (VP) model. In this model, when internal stresses are smaller than the sea-ice strength in compression, tension, or shear, ice behaves as a highly viscous fluid; when ice is under stresses equal to the sea-ice strength, it behaves as a plastic solid. Using this approach creates simpler equations to solve – this is why the VP model has become the most widely-used rheology in current sea-ice dynamics models.

More recently, *Tremblay and Mysak* [1997] simulated sea ice as a granular material, based on observations that demonstrate the pattern of deformation in sea ice is analogous to that of sand or clay – two materials that have been simulated with success using a granular rheology. In this model, shear deformation, with some convergence or divergence (dilatation), occurs along sea-ice leads at some angle from the main axis of loading, demonstrating static friction that resisted the motion. *Hunke and Dukowicz* [1997] developed the Elastic-Viscous-Plastic (EVP) model and added an elastic term to the VP model of *Hibler* [1979]. The term carries the information (internal stresses) in the sea-ice domain effectively and allows for an explicit treatment of the resulting differential equations.

Tsamados et al. [2013] added the anisotropic sea-ice rheology of *Wilchinsky and Feltham* [2006] to the EVP model of *Hunke and Lipscomb* [2008] in order to account for the fact that sea-ice leads (and therefore sea-ice strength) aligned themselves in specific directions with respect to the wind forcing. In recent years, the Elasto-Brittle (EB) rheology was introduced by *Girard et al.* [2011a]. This model is based on linear elastic theory and lead to a realistic representation of the mode of the fracture of sea ice under the action of winds and ocean currents. The plastic deformations, however, are affected by a parameterization of damage that is more crude. *Bouillon and Rampal* [2015] later implemented a Lagrangian finite-element scheme, coupled a thermodynamic model to the EB model, and also provides a parameterization for the damage and healing associated with sea-ice deformation.

Recent developments in sea-ice dynamic models also include an improved numerical solver, and more physically based parameterizations. For instance, *Zhang and Hibler* [1997] suggested a line successive, over-relaxation method (LSOR) for the solution of the linearized momentum equation as opposed to the successive relation method suggested by *Hibler* [1979]. Later, *Lemieux et al.* [2010] proposed the Jacobian-Free Newton-Krylov method to improved the convergence of the full non-linear problem. Finally, *Tsamados et al.* [2014] developed a parameterization for the surface stresses acting on sea ice, that takes into account sea-ice roughness and presence of melt ponds. This is based on observations collected during the Surface Heat Budget of the Arctic Ocean (SHEBA) field campaign [*Andreas et al.*, 2010]. This parameterization is included in the Los Alamos Sea Ice Model (CICE) version 5, and leads to an improved simulation of sea-ice cover, particularly in regards to sea-ice age [*Hunke*, 2014]. All of the models described here consider sea ice to be a two-dimensional material with vertically averaged mechanical stress and yield criteria that depend on the mean ice thickness (or ice thickness distribution in the case of a multi ice thickness category model) and ice concentration. Observations, however, demonstrate that thermal stresses vary with depth of sea ice and are at least as large as dynamical stresses. These three-dimensional effects are presently ignored in sea-ice models.

Thermal stress is the stress that develops when gradients in temperature are present within a material. In sea ice, it is caused by changes in surface air temperature. Previous observations illustrate that thermal stresses are of the same order of magnitude as dynamic stresses [e.g. *Tucker and Perovich*, 1992; *Lewis et al.*, 1994; *Richter-Menge and Elder*, 1998]. Thus, when large thermal stresses are present, thermal cracking can trigger sea-ice ridging, lead opening, and shear failure [*Evans and Untersteiner*, 1971]. Thermal stress creates a vertical structure on the depth-independent dynamic stress. For this reason, thermal stresses can have a significant impact on the dynamics of sea ice, and should be considered in a complete sea-ice rheological model.

Furthermore, it is now recognized that the sea-ice strength may depend not only on the mean ice thickness and ice concentration, but also on ice temperature or the total brine volume of sea ice [e.g. *Johnston*, 2006; *Timco and Johnston*, 2002; *Timco and O'Brien*, 1994]. *Timco and O'Brien* [1994] derived the flexural strength of ice as a function of brine volume using data from experiments conducted both in the field and in a laboratory. The flexural strength of sea ice, in turn, is related to the compressive strength that ice can withstand before fracturing and ridging. Later, *Johnston* [2006] demonstrated that the sea-ice borehole strength decreases significantly with total brine volume and, therefore, with temperature. After the ice reaches the freezing point temperature, which roughly coincides with the onset of the brine volume drainage, the weakening stops. These results suggest that the parameterization of sea-ice strength as a function of depth-dependent ice temperature may improve the sea-ice models. Both the implementation of thermal stress and the parameterization of sea-ice strength as a function of ice temperature require a vertical coordinate, therefore, the development of a three-dimensional model is inevitable.

The impacts of ice temperature on the sea-ice strength can be important especially on the onset and breakup of landfast sea ice. Landfast sea ice is defined as sea ice that is immobile for a specified time interval, and extends from a coastline or a region of grounded sea ice [*Barry et al.*, 1979]. Landfast ice covers 1.8×10^6 km^2 (∼20 %) of the Arctic Ocean and has an average annual duration of more than seven months [*Yu et al.*, 2014]. The presence of landfast ice is important for: local Inuit communities who use it as a hunting and fishing platforms [*George et al.*, 2004]; and local ecosystems, because it alters the pattern of migration and nutritional status of fish and marine mammals [e.g. *Tynan and DeMaster*, 1997; *Macdonald et al.*, 1995]. Landfast ice is also important to a high-latitude climate, because it moves the location of deep water formation father offshore at the edge of the continental shelf [*Itkin et al.*, 2015], and relocates the ice edge and polynya to a higher latitude at the end of the melt season [*Reimnitz et al.*, 1994]. In the East Siberian, Laptev, and Kara seas, the landfast sea ice extends northward as far as 500 km from the coasts despite offshore winds [*Reimnitz et al.*, 1994]. This broad extent is due to the tensile strength of sea ice and the presence of islands offshore of the coast [*König Beatty and Holland*, 2010], and the grounding of sea ice in shallow water areas [*Selyuzhenok et al.*, 2015; *Lemieux et al.*, 2015; *Haas et al.*, 2005]. Along the Alaskan coast, the landfast sea-ice extent is much smaller, approximately 50-km wide [*Barry et al.*, 1979], and is stable due to ice anchoring on the ocean floor at its outer edge along the ∼20-m isobaths – or the stamukhi zone [*Mahoney et al.*, 2007]. In the Canadian Arctic Archipelago (CAA), the sea ice is landlocked (i.e. attached to the shore on all sides) and is stable mainly because of its compressive strength [*Melling*, 2002]. Current sea-ice models correctly simulate landfast (landlocked) sea ice in the CAA. However, simulated timing of landfast ice onset and breakup are not yet very accurate [*Lemieux et al.*, 2015; *Sou and Flato*, 2009].

The goal of this thesis is to lay the foundation for a three-dimensional ice dynamics model that considers both thermal and dynamic stresses. We suggest that a three-dimensional ice dynamics model would provide a more physically based failure criteria, and therefore, resulting in more accurate deformation fields. We begin this investigation with a detailed analysis of in-situ internal sea-ice stresses measurements in the CAA. In the second stage of research, we develop a thermodynamic model that considers variations in temperature and internal sea-ice thermal stresses, and compare the results from this model with in-situ observations. Finally, we use the landfast ice onset and breakup events from several buoys deployed in the CAA as part of our Canadian Arctic Buoy Program to infer the mechanical strength properties of landfast sea ice.

The thesis is organized as follows. In Chapter 2, we present the internal sea-ice stress data from the landfast sea ice in the CAA. The results reveal that thermal stresses are as large as dynamical stresses, and are anisotropic during the landfast season within sea ice because of land confinement in the narrow passages of the CAA [*Hata and Tremblay*, 2015a]. In Chapter 3, we present an anisotropic thermal stress model that simulates thermal stresses within the sea ice under land confinement (i.e. in the narrow channel) [*Hata and Tremblay*, 2015b]. The model simulates well the observed sea-ice thermal stresses with three layers in the ice and one layer in the snow. This result highlights the importance of properly simulated snow depth and temperature dependent physical properties of sea ice. In Chapter 4, we estimate the compressive strength of sea ice from the sea-ice velocity obtained in the CAA, following the method developed by *Pritchard* [1976] and later adopted by *Tremblay and Hakakian* [2006]. Finally, we present concluding remarks and a description of future work in Chapter 5.

Chapter 2

Anisotropic internal thermal stress in sea ice from the Canadian Arctic Archipelago

This chapter includes the investigations of the characteristics of internal sea-ice stress in the Canadian Arctic Archipelago throughout the year, including the sea-ice drift and landfast ice seasons. This chapter consists of a paper published in the Journal of Geophysical Research: Hata, Y. and Tremblay, L. B. (2015), Anisotropic internal thermal stress in sea ice from the Canadian Arctic Archipelago, J. Geophys. Res, 120, **8**, p5457–5472, doi:10.1002/2015JC010819.

Anisotropic Internal Thermal Stress in Sea Ice from the Canadian Arctic Archipelago

Y. Hata [1], and L. B. Tremblay [1]

[1] Department of Atmospheric and Oceanic Science, 805 Sherbrooke Street West,
McGill University, Montreal, Quebec, Canada. H3A 0B9

Abstract

Results from an Ice Stress Buoy deployed near the center of a multi-year floe in the Viscount Melville Sound of the Canadian Arctic Archipelago between 10 October 2010 and 17 August 2011 are presented. The position record indicates the landlocked season was approximately 5 months, from 18 January to 22 June, when the sea ice was fast to Melville Island and Victoria Island. Thermal stresses (ranging from -84 to 66 kPa) dominate the internal stress record, with only a few dynamic stress events ($\sim$50 kPa) recorded before the landlocked season. Intriguingly, the thermal stresses are isotropic before the landlocked ice onset and anisotropic during the landlocked season. Two possible causes to explain anisotropy in thermal stresses are considered: preferred c-axis alignment of the ice crystal, and land confinement associated with the nearby coastline. The orientation of the principal stresses indicates that land confinement is responsible for the anisotropy. The stress record also clearly shows the presence of residual compressive stresses at the melt onset, suggesting a viscous creep relaxation time constant of several days. Finally, results show an interesting reversal in the sign of the correlation (from negative to positive) between surface air temperature and thermal stress after the onset of surface melt. We attribute this to the onset of water infiltration within sea ice after which colder night temperature leads to re-freezing and compressive stresses. To the best of the authors' knowledge, this is the first time that anisotropic thermal stresses have been reported in sea ice.

2.1 Introduction

Internal sea-ice stresses are induced by winds, ocean currents, floe-floe interactions, and surface air temperature fluctuations [*Tucker and Perovich*, 1992]. Early on, researchers have been mainly interested in estimating ridge building forces and loads on offshore structures for engineering applications [e.g. *Comfort et al.*, 1992; *Richter-Menge and Elder*, 1998]. To this end, they have focused on sea-ice motion and the resulting dynamical stresses. More recently, the emphasis has shifted towards bridging the gap between large scale mechanical properties of sea ice and the magnitude of internal dynamic stresses from in-situ measurements for the purpose of validating or proposing new sea-ice rheological models [e.g. *Lewis and Richter-Menge*, 1998; *Hutchings et al.*, 2010]. A clear understanding of the effect of thermal stresses on the mechanical behaviour of sea ice in the context of large scale sea-ice modeling, however, is still lacking.

In the seminal sea-ice dynamics model of *Coon et al.* [1974], the sea ice is considered to behave as an elastic-plastic isotropic material with no bi-axial tensile strength since sea-ice leads are assumed to open freely in divergence (the Arctic Ice Dynamics Joint Experiment, AIDJEX). Later, *Hibler* [1977, 1979] introduced the viscous plastic sea-ice model in which small elastic reversible deformations are approximated by viscous creep, while maintaining the no-tensile strength (AIDJEX) assumption. This led to a much simpler numerical solution of the governing equation and the VP model quickly became the standard sea-ice model used in the community. Later improvements mainly focused on the development of more efficient numerical solvers [e.g. *Hunke and Dukowicz*, 1997; *Zhang and Hibler*, 1997; *Lemieux et al.*, 2008; *Lemieux and Tremblay*, 2009], and the constitutive equation representing sea-ice interactions remained mostly the same [exceptions: *Girard et al.*, 2011b; *Sulsky and Schreyer*, 2004; *Tremblay and Mysak*, 1997]. Note, however, that different numerical approaches allow for the simulation of landfast ice when tensile strength of sea ice is included [see for instance *König Beatty and Holland*, 2010]. Recently, it has been recognized that the AIDJEX assumptions of no tensile strength and material isotropy are inadequate [*Coon et al.*, 2007] and anisotropic rheologies, either with or without tensile strength, have been developed [e.g. *Sulsky and Schreyer*, 2004; *Wilchinsky and Feltham*, 2006]. Note that in all models cited above, thermal effects in the sea-ice rheology are not considered.

Early field campaigns aimed at measuring internal sea-ice stresses took place on multi-year ice in the southern Beaufort Sea in the spring of 1986, 1989 and 1991 [*Croasdale et al.*, 1988; *Comfort and Ritch*, 1990; *Comfort et al.*, 1992]. These campaigns focused mainly on dynamic stresses, in particular, on large scale pack-ice driving force on structures and the estimation of multi-year ice compressive strength. *Croasdale et al.* [1988] provided an estimate of the sea-ice compressive strength of 52 kN/m from a ridge building event that occurred in the proximity of their stress sensors. *Comfort and Ritch* [1990] reported ridge building forces ranging from 150 to 700 kN/m, and *Comfort et al.* [1992] reported a mean ridge building force of 30 kN/m with a range of 8 to 71 kN/m.

In the fall of 1988 (18 September to 25 November), *Tucker and Perovich* [1992] deployed bi-axial wire stress sensors [*Cox and Johnson*, 1983] on first-year and multi-year ice about 300 km northeast of Svalbard, as part of the Coordinated Eastern ARctic EXperiment (CEAREX). The authors report the presence of open water in the vicinity of the floe from visual observations. Two sources of internal ice stress were identified from the measurements: dynamic stresses (tides, inertial oscillation, and floe-floe collision induced by wind) and thermal stresses. Their results show that dynamic ice stresses in multi-year ice floes decrease with distance from the floe edge — from about 180 kPa at the edge of a 1.5 km diameter floe to about 30 kPa 200 m in the interior of the floe. The stress induced by tidal or inertial oscillation ranged between 20 kPa and 50 kPa. They also show that thermal stresses are well simulated using the simple 1D thermal stress model of *Bogorodsky et al.* [1972], in which thermal stresses are assumed to be isotropic and viscous creep is not considered, despite clear evidence of viscous creep stress relaxation (see their Figure 6).

The first stress measurements on first-year landfast sea ice in the Canadian Arctic

Archipelago (CAA) were done southwest of Cornwallis island in March of 1992 using bi-axial wire stress sensors [*Lewis et al.*, 1994]. In this field campaign, they artificially increased the rate of change of internal sea-ice temperature, and therefore thermal stresses, by mechanically removing the snow cover from the ice. The observed thermal stresses (assumed to be equal to the averaged normal stress) are well simulated by the 1D thermal stress model of *Bogorodsky et al.* [1972], in which viscous creep was included [*Lewis*, 1993]. *Lewis et al.* [1994] report tensile stresses in first-year ice as large as 120 kPa when surface air temperature changed from -25°C to -31°C, following the removal of the snow cover. This shows the sensitivity of internal thermal stresses with changes in the snow cover depth.

In the winter of 1993-94 (7 October to 21 March), *Richter-Menge and Elder* [1998] deployed bi-axial wire stress sensors in the Beaufort Sea as part of the Sea Ice Mechanics Initiative (SIMI). The observed major principal stresses (defined as positive in compression) show higher frequency content, typical of dynamic stresses, at the edge of the floe than in the interior, which is dominated by thermal stresses. *Richter-Menge and Elder* [1998] proposed two methods to separate the thermal and dynamic stresses. They first assumed that high-frequency stresses (periods of the order of hours) represent ice-motion induced stresses and lower frequency stresses (periods of the order of days) represent thermal stresses. This separation based on frequency was, however, unsuccessful as the residual ice-motion-induced stress still had a high correlation with ice temperature. They then assumed that the minor principal stress (highly correlated with surface ice temperature) represents the thermal stress and the difference between the principal stresses represents the dynamic stresses. The resulting ice-motion-induced stresses exhibit both high and low frequency variation and they argue that this method provides a good first-order approximation of thermal and dynamic stresses. Finally, they discuss the seasonality of the observed internal stresses in the Beaufort Sea, with a dominance of thermal stresses in the fall and a dominance of ice-motion-induced stresses in the winter.

Several bi-axial wire stress sensors were deployed on a 3-km-diameter multi-year ice floe during the Surface HEat Budget of Arctic Ocean (SHEBA) field experiment (October 1997 to April 1998) in the Beaufort Sea [*Richter-Menge et al.*, 2002a]. This study focuses only on dynamic stresses, obtained by removing the thermal stress from the total stress time series following the method proposed by *Richter-Menge and Elder* [1998]. The spatially averaged dynamic stress during the SHEBA experiment is 25 kPa with a maximum value around 60 kPa (compression). The thermal stresses range between -60 and 50 kPa [see Figure 2 in *Weiss et al.*, 2007]. Their results and of *Richter-Menge et al.* [2002b] also show that dynamic stresses observed in the interior of the floe are related to the ice deformation at the regional scale, i.e. internal sea-ice stresses increase during periods of ice convergence, and the internal sea-ice stress decreases during periods of divergence.

Five bi-axial wire stress sensors were deployed in first-year and multi-year ice in the Beaufort Sea during the Sea ice Experiment: Dynamic Nature of the Arctic [SEDNA, 5 April to 25 May 2007: *Hutchings et al.*, 2010]. The stress results confirm the hypothesis of *Richter-Menge and Elder* [1998] that the minor principal stress (positive in compression) represents thermal stress and that the difference in principal stresses provides a good estimate of the maximum shear stress associated with ice motion, although it is suggested that more field work is required to confirm that thermal stresses are isotropic. The maximum reported dynamic stress component is approximately 40 kPa, with an average of 10 kPa. The thermal stresses range from -20 to 70 kPa [*Hutchings et al.*, 2010]. Note that, in all studies cited above, the thermal stresses are of the same order of magnitude as the dynamic stresses, and thermal stresses are assumed to be isotropic.

In this paper, we present internal ice stress data from an internal Ice Stress Buoy (ISB) deployed in the Viscount Melville Sound in the CAA (10 October 2010 - 15 July 2011). This is the second ISB deployed in the CAA, after the first measurement by *Lewis et al.* [1994]. The prominent landlocked regime in this region of the Arctic is very different from the previously recorded internal ice stresses in the Beaufort and Lincoln Seas, where the sea ice was in constant motion due to wind forcing [e.g.

Comfort et al., 1992; *Tucker and Perovich*, 1992; *Richter-Menge and Elder*, 1998; *Richter-Menge et al.*, 2002a].

The observed stresses presented in this paper are dominated by thermal stresses that are well correlated with surface air temperature. Furthermore, we show that the difference in principal stresses (assumed to be equal to the dynamic stress in previous studies) is also correlated with surface air temperature during the landlocked ice season which calls into question the assumption of isotropy of thermal stress in the CAA. We consider two hypotheses to explain the anisotropy in thermal stress: land confinement and c-axis alignment of sea-ice crystals with surface ocean currents [e.g. *Tucker et al.*, 1987; *Weeks and Gow*, 1980; *Kovacs and Morey*, 1978; *Stander and Bernard*, 1989]. The data presented provide the first reported evidence (to the authors' knowledge) of anisotropy in landlocked sea-ice thermal stresses.

The manuscript is structured as follows. In section 2.2, we give a general description of the deployment, the sea-ice stress sensor and the ice stress buoy. The position and stress records are discussed in section 2.3. The conclusions are summarized in section 2.4.

2.2 Field Measurement Program

2.2.1 Buoy Deployment

An Ice Stress Buoy (ISB) and a Surface Velocity Profiler (SVP) were deployed on a multi-year sea-ice floe on 10 October 2010 at 74°15'N, 108°05'W in the Viscount Melville Sound of the CAA (Figures 2.1 and 2.2). This region is part of the Parry Channel which connects the Arctic Ocean to the west and Baffin Bay to the east. The deployment was conducted with the logistical support of the Amundsen ice breaker, a research vessel operated by the Canadian Coast Guard, as part of ArcticNet leg 3b (7 - 22 October 2010). The instrumented multi-year ice floe was approximately 2 km in diameter, and covered with old rounded ridges and several refrozen melt ponds.

The sea-ice thickness measured at three different locations, within approximately 10 m, ranged from 1.87 m at the ISB stress sensor location to 3.35 m. The ISB was deployed on a local high-point to avoid having the buoy sit in a melt pond during the following melt season [see installation manual for the CRREL ISB, B. Elder]. The floe was surrounded by water covered with a thin layer of newly formed grease ice. The air temperature on the day of deployment was -5.1 °C.

Figure 2.1: RADARSAT-2 ScanSAR image of the Viscount Melville Sound on 11 October 2010. The location of the deployment is indicated by the red dot. Data and Products ©MacDonald Dettwiler and Associates Ltd. (2010) — All Rights Reserved. RADARSAT is an official mark of the Canadian Space Agency.

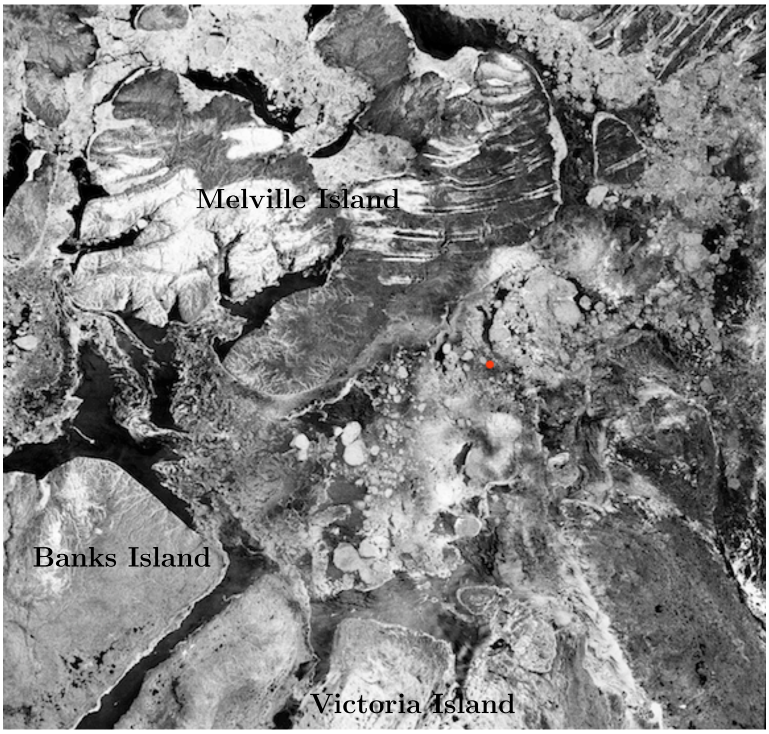

The ISB was installed by drilling a 4 inch (10.16 cm) hole in the floe down to 3 feet (91.44 cm) depth. A 2 inch (5.08 cm) hole was then drilled from the base of the 4 inch hole, to the ocean, to allow water to fill the cavity. The stress sensor was attached to a PVC pipe, and a wood dowel going through the PVC pipe was used to rest the instrument on the ice surface. The sensor-pipe assembly hung vertically down (like a pendulum) from the wood dowel, allowing it to freeze in a vertical position. The stress

Figure 2.2: Observed buoy drift from 10 October 2010 to 17 August 2011. Specific dates referred to in the text are also included. The landlocked season is from 18 January to 22 June 2011. Zoom in of (b) the first drifting season (10 October 2010 - 18 January 2011) and (c) second drifting season (22 June - 17 August 2011). The black solid box delimits the area over which the wind data presented in Figure 2.7 is averaged (73° N, 114° W - 75° N, 108° W).

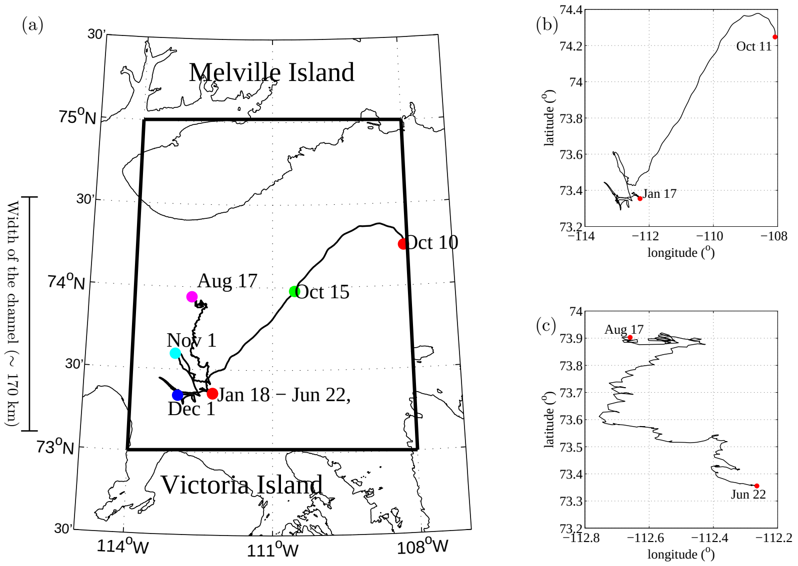

sensor was deployed 20.3 cm below the 34.3 cm deep freeboard, i.e. at the depth of 54.6 cm from the ice surface(see Figure 2.3a). The buoy hub was set in the ice about 4 m away from the stress sensor, using a 3 foot (91.44 cm) long 10 inch (25.40 cm) diameter auger. The buoy compass was aligned with the Magnetic North Pole, and the stress sensor (wire 1: see section 2.2.2) was also aligned with the Magnetic North Pole using a handheld compass. The stress sensor was connected to the buoy hub by a 6-m-long cable (see Figure 2.3a).

The ISB ran autonomously and transmitted data through the ARGOS satellite system every hour, until the buoy stopped transmitting on 17 August 2011. This allowed for the continuous collection of hourly internal ice stresses (at 54.6 cm depth), air temperatures, ice temperatures (at 54.6 cm depth), location, and compass angle over a period of 10 months. The ISB failed to report its position on several occasion starting on 13 July. The blank in the time series were filled with position reported by the SVP deployed a few meters away. We note that when the buoy was landlocked, it

Figure 2.3: Schematic of (a) the Ice Stress Buoy and (b) the stress sensor. α is the angle between the minor principal stress (σ_2) and wire 1. Wire 1 was aligned with the Magnetic North Pole using a handheld compass during the deployment. The declination angle (δ) between the Magnetic North Pole and the Geographic North Pole in 2010 is approximately 17° in the CAA.

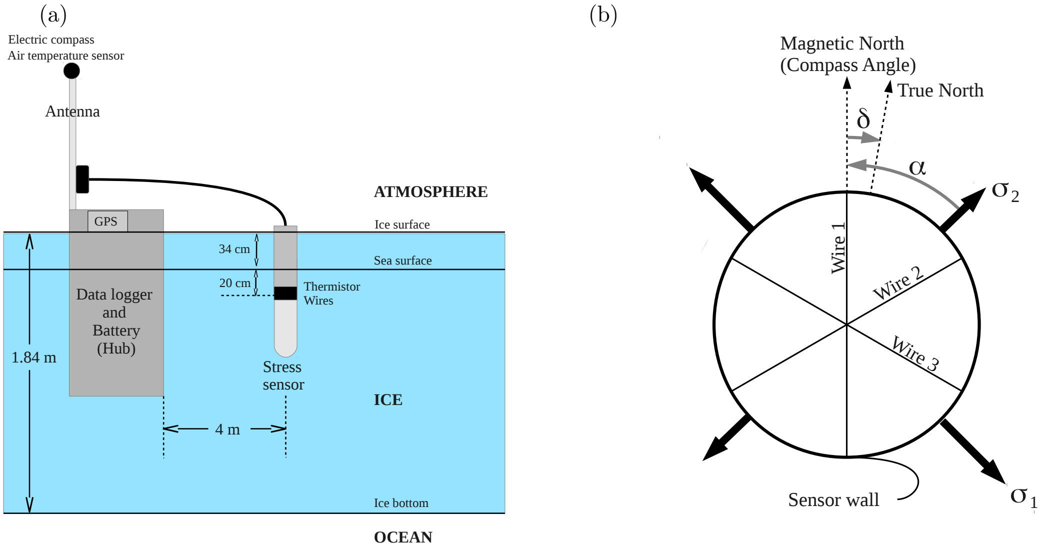

was located near the north shore of Victoria Island where the coastline to the south is aligned in the northwest-southeast direction (Figure 2.2a, cf. section 2.3.1).

2.2.2 Internal Ice Stress Buoy (ISB) and Surface Velocity Profiler (SVP)

The ISB was manufactured by the Cold Regions Research and Engineering Laboratory (CRREL), and the SVP was manufactured by MetOcean. The ISB is equipped with a stress sensor (model 4350 from GEOKON), a thermistor used to measure the ice temperature at the depth of the sensor, and a thermistor used to measure 2-m air temperatures (model 107-L05 from Campbell Scientific) (see Figure 2.3a). The accuracy of both thermistors is 0.01 °C. The buoy is also equipped with a Global Positioning System (GPS: model 9601-DGS-LP from NAL Research Corporation) giving the position of the buoy (latitude and longitude) with an accuracy of 10 m and an electric compass (model EZ-Compass-3A V from Advanced Orientation Systems, Inc.) that measures the orientation of the buoy (wire 1) with respect to the Magnetic

North Pole with a resolution of 0.08°. The ISB is powered by a lithium battery (TLP-93181/D/OCN2) manufactured by Tadiran Battery. The battery and the data logger (CR1000-ST-SW-NC from Campbell Scientific, Inc.) are included in the buoy hub.

The stress sensor used in this study is a biaxial vibrating wire stress sensor originally designed by *Cox and Johnson* [1983]. This sensor was successfully used in other Arctic field programs [e.g., *Tucker and Perovich*, 1992; *Richter-Menge and Elder*, 1998] and consists of a stiff steel cylinder, 25 cm long, 5.7 cm in diameter, and a wall thickness of 1.6 cm. There are three wires and a magnetic coil inside the cylinder. Wires are set 120° from each other across the cylinder diameter (see Figure 2.3b) and the coil is located under the wires. The wires are plucked by the magnetic coil, inducing a vibration; the periods of each vibrating wire are recorded as raw data.

The elastic deformation of the steel cylinder is related to the period of vibration of each wire and the stresses in the material (in this case sea ice) are calculated from the cylinder deformation and its Young's modulus [*Cox and Johnson*, 1983]. This calculation gives the principal stresses (σ_1 and σ_2) and the angle between the minor principal stress (σ_2) and wire 1 (defined positive clockwise). A thermistor located in the proximity of the wires and attached to the cylinder wall is used to correct for thermal effect on the period of vibration. This correction is done during data post-processing. The error on the principal stresses has been reduced from 20 kPa to an estimated 5 kPa for a loading range between 0 and 2 MPa, with the use of a superior data-logging system [*Cox and Johnson*, 1983; *Tucker and Perovich*, 1992] (see also campbellsci.com). The error in the stress angle is 5°. The conceivable factors for degrading the measurement are the installation and the ice melting around the sensor.

The stress sensor is calibrated in the laboratory prior to deployment. To this end, the relationship between cylinder deformation and period of vibration of each wire, the temperature sensitivity of the wires, and the period of vibration of each wire at 0°C under no load condition are characterized. The laboratory tests are done in an air-filled pneumatic sleeve that applies uniform, hydrostatic pressure. The sleeve is located in a temperature-controlled environmental chamber. The zero-reading of the sensor is sensitive. It can change during shipment and installation, and drifts during the course of a field experiment [*Richter-Menge and Elder*, 1998]. Ideally, wire periods would be recorded in the field when no mechanical stresses are applied on the sea-ice floe and no significant temperature variations are present. A final calibration would also be made at the end of the experiment by cutting out a block of ice around the sensor when no internal ice stresses are present. This could not be done, however, as the ISB was not recovered.

In this study, we have applied a linear correction to the periods of vibration between 12 October 2010 (Julian Day 285; 2 days after deployment date) and 15 July 2011 (JD 561), 16 days (approximately twice as long as the viscous creep relaxation time constant) after the ice temperature at the depth of the stress sensor reaches the melting temperature of 0°C for the first time. We use the sensor output on that day as the first anchor point corresponding to zero stress despite the fact that some thermal stresses must have been present when the sensor was installed on 10 October when the air temperature was -5.1°C. The second zero-stress anchor point is set on 15 July (JD 561), 16 day after the melt onset.

The output from the stress sensor is used to calculate the direction of the principal stresses (σ_1 and σ_2) with respect to wire 1 (see Figure 2.3b). The angle between the principal stresses and Geographical North Pole were calculated from the electrical compass record and a constant magnetic declination angle of 17° between the Magnetic North Pole and the Geographic North Pole in the Viscount Melville Sound in 2010-11. The compass reading from the ISB was not constant during the landlocked ice season. Instead the reading was correlated with surface air temperature, contrary to the manufacturer specifications (see Figure 2.4a). While the input voltage of the surface air temperature sensor — whose wire passed just beside the compass on the antenna mast — was programmed to be zero during compass reading, we hypothesize that this may not have been the case. Tension on the wire of the air temperature sensor would produce a magnetic field around the wire and alter the magnetic compass reading. We applied a temperature correction to the compass reading based on a piecewise linear fit between surface air temperature and raw compass reading during the landlocked season when the orientation of the ISB with respect to the Magnetic North Pole was constant. Results from this exercise show that the floe rotated by 10° counterclockwise prior to being landlocked on 18 January (JD 383) (see Figure 2.4b). Note that there is a sudden shift on JD 530 and a return to pre-JD-530 values on JD 544. The fact that there is no ice motion — as per the GPS data — and that the angle is nearly constant before, during and after the shift suggest a problem in the raw compass angle data as opposed to real rotations of the ice floe.

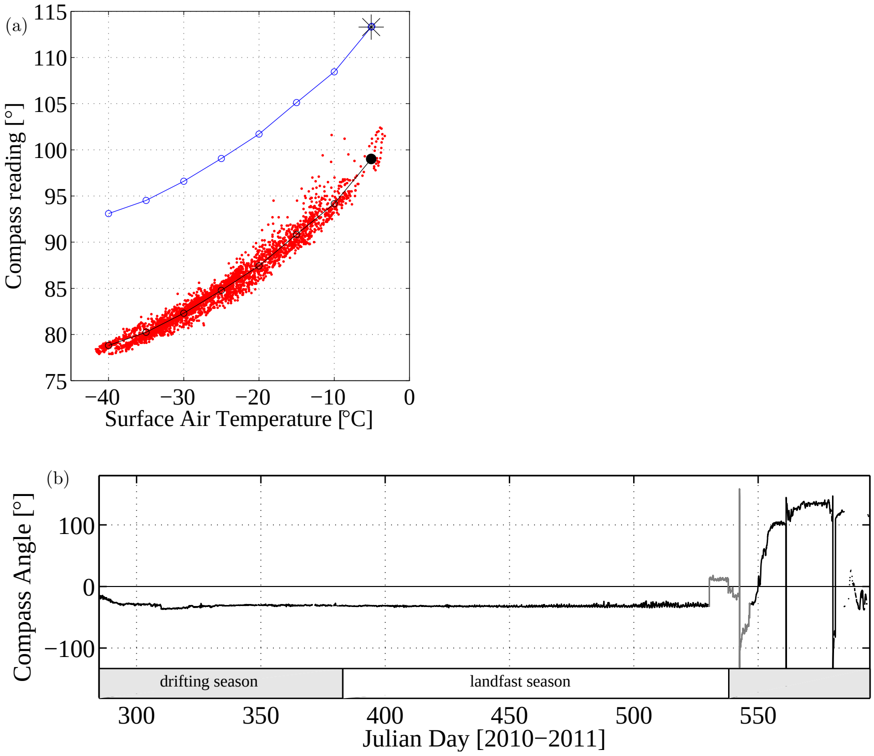

Figure 2.4: (a) Raw compass reading (red dots) as a function of surface air temperature during the landlocked season (JD 383 - 556). While the compass was aligned with the Magnetic North Pole at deployment, the initial reading was 113 ° (marked by the star symbol in panel a) when the surface (1 m) air temperature was -5.1 °C). We apply a temperature correction (thin blue line) to the raw compass angles derived from a piecewise linear fit between the raw angles and the surface air temperature (thin black line), with a constant offset of 15 degrees (counterclockwise), equal to 113° - 98°, the angle from the piecewise liner fit extrapolated to -5.1 °C, the air temperature at deployment (solid black dot in a). (b) Buoy orientation relative to the Geographic North Pole after correction. The gray line in the figure shows the data measured when a problem in the compass reading presumably exits (see section 2.2.2).

2.3 Results and Discussion

2.3.1 Ice Motion and Landlocked Ice Season

The ISB was deployed approximately 70 km from the south shore of Melville island and 120 km from the north shore of Victoria island (see Figure 2.2a). During the full 10-month life of the buoy, the floe drifted a total distance of 640 km, from 74°15’ N, 108°05’ W to 73°59’ N, 112°38’ W between 10 October 2010 and 17 August 2011 (JD 283 - 594).

After deployment, the ISB drifted 140 km southwest for the first 12 days (JD 283 - 295) with an average speed of 4.2 km/day, almost parallel to the southern coast of Melville Island. Between 23 October and 18 January (JD 296 - 383), the floe moved in the northwest and southeast direction. The landlocked season starts on 18 January (JD 383), when the floe stopped drifting. The end of the landlocked season on 22 June 2011 (JD 538) is defined as the moment when the floe starts to rotate as per the compass angle time series (see Figure 2.4b). Note that the floe starts drifting soon after on 28 June 2011 (JD 544) as per the GPS time series (see Figure 2.5). From 18 January to 22 June (JD 383 - 538) the ice was landlocked, and GPS readings from the ISB were constant, except on 10 April (JD 465), when a velocity of 1.4 cm/s (corresponding to a displacement of 52 m in an hour) was observed (see Figure 2.5). Analysis of the co-deployed SVP drift, however, indicate that this is a false recording. The ISB position indeed was the same after and before this anomalous reading. This is the only obvious false recording of the 10-month time series. All other changes in position recorded by the ISB during the landlocked season are within the measurement error of the GPS, therefore, they are indifferentiable from zero. Between 22 June and 17 August (JD 538 - 594), the ISB drifted approximately 70 km northward with an average speed of 0.5 km/day.

Figure 2.5: Time series of floe drift speed calculated from observed ISB GPS locations — not including the SVP data used to substitute the false recording and missing ISB data.

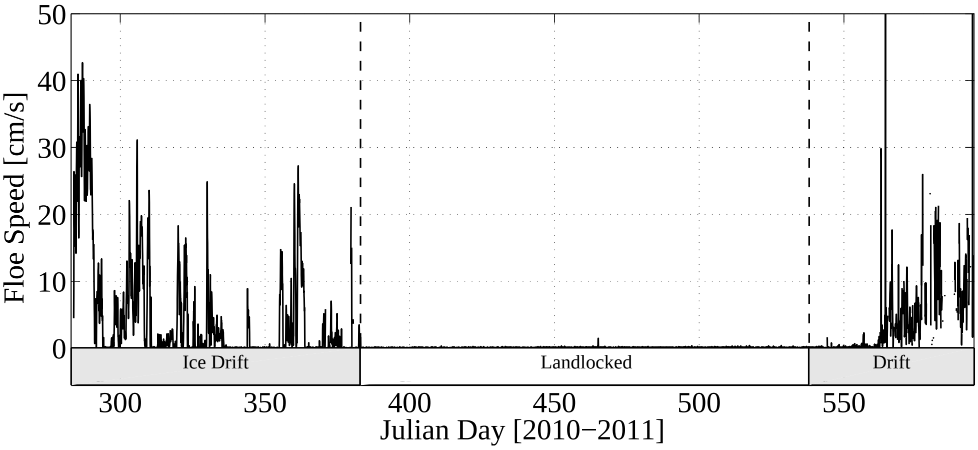

2.3.2 Internal Ice Stresses

The ISB measures the principal stresses (σ_1 and σ_2) and the direction of the principal stresses with respect to the Magnetic North Pole. Note that the mean normal and maximum shear stresses (σ_I and σ_{II} — i.e. the stress invariants) are equal to the average of the two principal stresses and the difference between the two principal stresses divided by two, respectively.

The internal stress data from the ISB, measured at a depth of 54.6 cm from the ice surface, range from -84 kPa (compressive) to 66 kPa (tensile), with 60 % of the stresses being positive (tensile: see Figure 2.6a). The magnitude of the stresses measured at this site are similar to the stresses measured in previous field campaign: CEAREX (∼150 kPa) [*Tucker and Perovich*, 1992] and SIMI (∼60 kPa) [*Richter-Menge and Elder*, 1998]. After deployment, the stress data shows that the stress sensor was subjected to compressive stresses of around -30 kPa as the seawater in the 4 inch (10.16 cm) borehole froze around the sensor (see the insert in Figure 2.6a). A few days after the deployment, the compressive stresses were relieved via viscous creep. Following *Richter-Menge and Elder* [1998] and *Hutchings et al.* [2010], we first estimate dynamic stresses as the difference between σ_1 and σ_2 assuming thermal stresses are isotropic and their magnitudes are equal to σ_1 (see Figure2.7a).

Table 2.1: Important dates. [a]The date for snow melt onset and ice melt onset are from a simulation of the 1D multi-layer sigma-coordinate thermodynamic model of *Huwald et al.* [2005] forced with the observed 1-m surface air temperatures.

Event	**Julian Date**	**Calendar Date**
Deployment	283	10 October 2010
Polar night	310-400	6 November 2010 - 4 February 2011
Landlocked onset	383	18 January 2011
Snow melt onset [a]	524	8 June 2011
Ice melt onset [a]	526	10 June 2011
Reversal of the correlation between ice temperature and thermal stresses	530	14 June 2011
Landlocked break-up	538	22 June 2011
Ice reaches isothermal condition (0°C)	545	29 June 2011
Noisier internal stress measurement	559	13 July 2011
Ice melt reaches sensor depth	561	15 July 2011
Buoy Death	594	17 August 2011

Dynamic Stresses

We first note that the difference in principal stresses $\sigma_2 - \sigma_1$, often interpreted as the dynamic stress, does not correlate with wind speed during the landlocked season (r = -0.01) or drift season (r = 0.17) (see Figure 2.7). The correlation remains low even if we perform a running-average on the data with a time window of a few days to keep only synoptic scale variability, or if we only consider data points when the wind direction is close to perpendicular with the nearby coastlines. Instead, $\sigma_2 - \sigma_1$ shows high-frequency fluctuations (indicative of dynamic stresses) between 19 and 23 November (JD 323 - 327), and between 14 December and 6 January (JD 348 - 371). We interpret these sudden high-frequency peaks in stresses with floe collisions during the drift season.

The surface air-ice stress is the dominant source of dynamic stress during the landlocked season, when no inertial oscillations or collisions between floes occur. The ocean current velocities in the Viscount Melville Sound are small [*Prinsenberg and Pettipas*, 2008; *Wang et al.*, 2012] and induce relatively low ice stresses. A scale analysis of the total force induced by the wind over a given fetch is equal to $\boldsymbol{\tau}_a L = \rho_a C_a |\mathbf{U}_a|^2 L$

Figure 2.6: (a) Time series of the major (σ_1: red line) and the minor (σ_2: blue line) principal stresses, (b) surface air (1 m: blue line) and wire (red line) temperatures, and (c) corrected angle between the minor principal stress (σ_2) and Geographic North Pole, defined positive clockwise and ranging between ± 90°. Note that the stress angle, shown in (c), is only meaningful when the stress states are anisotropic ($\sigma_1 \neq \sigma_2$). The insert in (a) shows a zoom-in on the stress for the first few days when the sensor set in the ice.

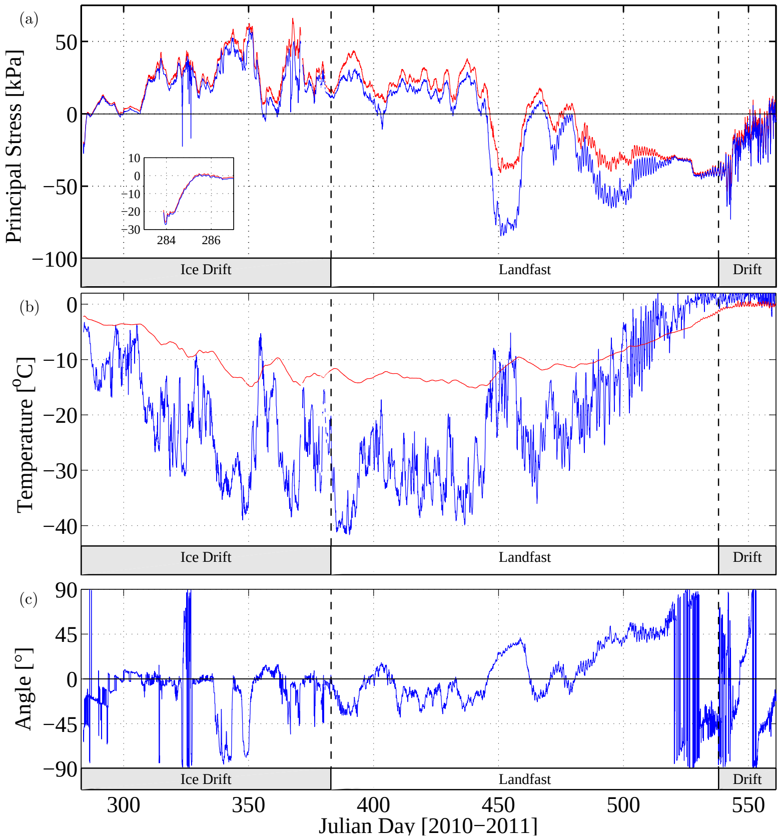

[*McPhee*, 1975], where $\boldsymbol{\tau}_a$ is the surface wind stress, ρ_a (1.3 kg/m^3) is the air density, C_a (3.5×10^{-3} unitless) is the air-ice drag coefficient and $|\mathbf{U}_a|$ is the surface wind speed. For a characteristic wind speed $|\mathbf{U}_a| = 7$ m/s and fetch L = 170 km (the width of the channel), the total surface wind stress is 37 kN. Such wind induced dynamic stresses are much larger than the sensitivity of the stress sensor and should be recorded by the ISB. This suggests that ISBs do not record the slowly varying internal stresses associated with surface wind stresses, and instead only record stresses resulting from mechanical failure and floe-floe interaction.

During the drift season (JD 284 - 383 and JD 538 - 561), the power spectrum of

Figure 2.7: Time series of (a) the difference between the major and minor principal stresses, (b) mean wind speed, and (c) mean wind angle over the region defined in Figure 2.2. The wind data is from the Canadian Meteorological Center's (CMC) Global Deterministic Prediction System (GDPS) [*Smith et al.*, 2013]. The wind speed and σ_2-σ_1, often used as a good first estimate of dynamic stress [e.g. *Hutchings et al.*, 2010], are not correlated (r = -0.01 during the landlocked season, r = 0.17 during the drift seasons).

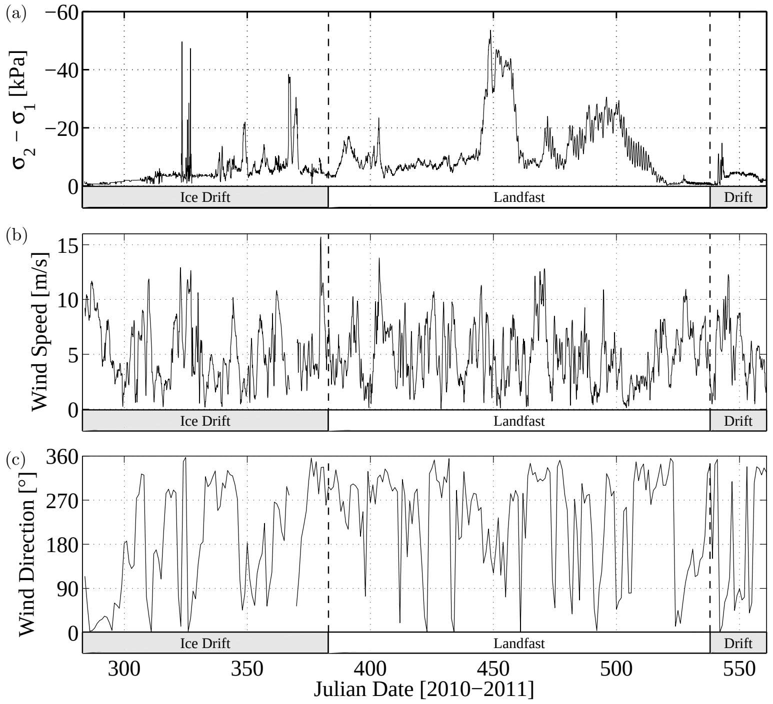

$\sigma_2 - \sigma_1$, calculated using a continuous wavelet transform, shows a weak peak at a frequency of 2 day^{-1} associated with tidal and/or inertial oscillations (see Figure 2.8a). Indeed, the position record of the ISB shows drift tracks in the shape of hairpins during both drift season (JD 283 - 383 and JD 538 - 594; see Figures 2.2b and 2.2c). A continuous wavelet transform analysis of the floe-drift vectors shows an appreciable peak at frequencies between 1.8 and 2.1 day^{-1}, confirming the presence of tidal/inertial oscillations (see Figures 2.8c and 2.8d). At a latitude of 73°N, the inertial oscillation and tidal signal frequencies are 1.92 day^{-1} and 1.94 day^{-1}, respectively. Following *Gimbert et al.* [2012], we calculated the signed Fourier Transform of the buoys velocities. The results confirm that both inertial oscillation (only negative frequency due to clockwise rotation) and tidal oscillation (both positive and negative frequencies) are present (see

Figure 2.9).

Figure 2.8: Wavelet power spectrum analysis of (a) σ_2 - σ_1, (b) air temperature, and the (c) u- and (d) v-component of the multi-year ice floe drift. Note that a log scale is used on the y-axis. The thick black contour indicates the 5% significance level against red noise and a lighter shade shows the cone of influence subject to edge effects.

(a) $\sigma_1 - \sigma_2$

(c) Buoy drift (u)

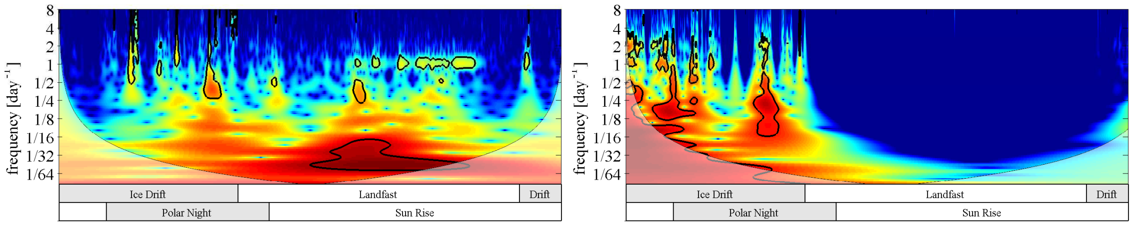

(b) T$_a$

(d) Buoy drift(v)

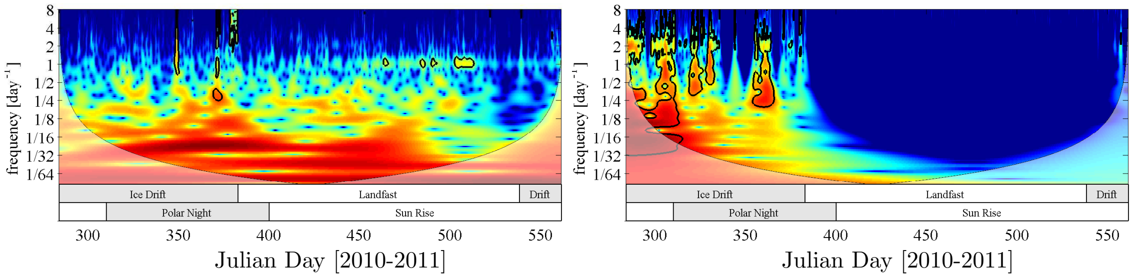

During the landlocked season (JD 383 - 538), there is by definition no inertial oscillations (1.92 day^{-1}) and there is no peak at the tidal frequency (1.94 day^{-1}). The absence of a tidal signal in the second stress invariant ($\sigma_2 - \sigma_1$) during the landlocked season is presumably due to its smaller magnitude. This is in contrast with previous observations by *Tucker and Perovich* [1992] (see their Figure 14), who reported 25-50 kPa stresses associated with tidal and inertial oscillations. When the pack ice is mobile, tides and inertial oscillations result in divergent and convergent sea-ice drift, and hence sea-ice collisions occur [*Holloway and Proshutinsky*, 2007]. For the landlocked sea ice in the CAA, tides do not cause floe collisions. Consequently, the stresses induced by tides are not recorded by the sensor.

Figure 2.9: Signed fourier spectrum analysis on the floe drift for (a) JD 283 - 383 and (b) JD 538 - 594. Note that the analysis on the second drift period (JD 538 -594) is done using 3-hourly position record of the SVP because the ISB failed to record its position frequently during this period. This limits the frequency range resolved from the data to ± 2 day^{-1}.

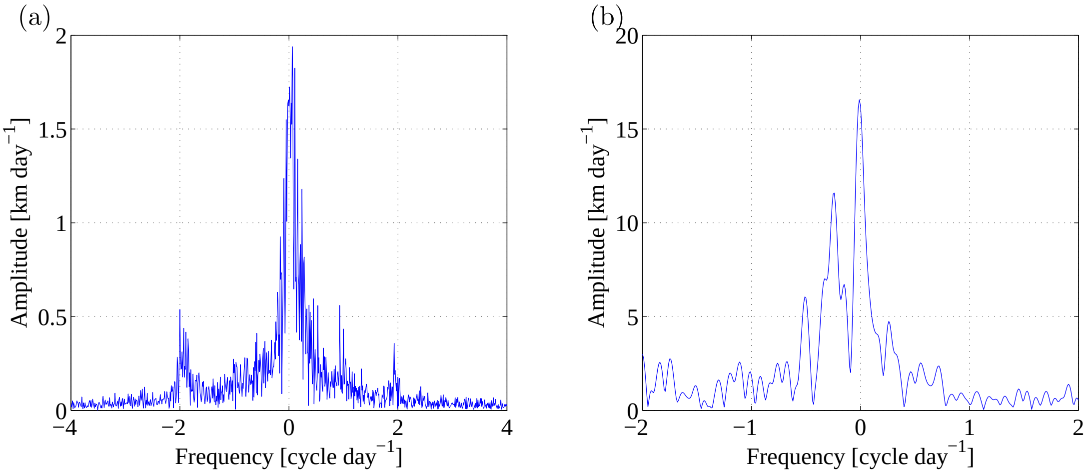

Thermal Stresses

When air temperature changes, the temperature signal is transmitted through the ice and damped with depth from the surface to the ice base, which remains at the freezing point temperature of -1.8°C. This vertical temperature gradient results in a different amount of thermal contraction or expansion with depth. In the absence of gravitational pull or buoyancy, a floe would bend and curl concave upward due to the vertical differences in horizontal strain, but because of the large aspect ratio (floe length over floe depth), the floe remains flat [*Lewis*, 1993]. As a result, tensile and compressive stresses develop in the upper and lower parts of a floe, respectively, when surface air temperature decreases.

Thermal stress is the dominant source of internal stresses in the ISB stress record. When the surface temperature decreases (increases) associated with the diurnal, synoptic or seasonal cycle, tensile (compressive) stress develops in the upper part of the sea ice. The magnitude of the thermal stress fluctuations associated with the diurnal, synoptic, and seasonal cycle in temperature is approximately 10 kPa, 60 kPa, and 40 kPa (see Figure 2.6a). The correlation coefficients (r) between surface air temperature and the observed principal stresses (σ_1 and σ_2) for the full 8-month period are -0.76 and -0.63, respectively (see Table 2.2 and Figure 2.10). These results are similar to previous measurements made at a mean depth of 22 cm in drifting multi-year ice by *Richter-Menge* [1997] and *Richter-Menge and Elder* [1998]. The maximum lagged correlation (r) between air temperature and σ_1 (σ_2) is -0.78 (-0.66) for a 26 (26) hour lag, the time scale required for the temperature signal to reach the stress sensor at 55 cm depth.

Table 2.2: Correlation coefficients (r) between air temperature and ice temperature at the sensor depth (-55 cm), and the principal stresses (σ_1, σ_2 and $\sigma_2 - \sigma_1$) from 10 October 2010 (JD 283) to 15 July 2011 (JD 561). The values inside of parentheses are the maximum lagged correlation coefficients (r). ^{a}The correlation coefficients (r) between air temperature and $\sigma_2 - \sigma_1$ is calculated for the landlocked season only (JD 383 - 538) and using the band-pass filtered surface air temperature and $\sigma_2 - \sigma_1$.

	σ_1	σ_2	$\sigma_2 - \sigma_1$
T_{air}	-0.76 (-0.78: 26 hours)	-0.63 (-0.66: 26 hours)	-0.65 ^{a}
T_{ice}	- 0.57	-0.39	—

The continuous wavelet spectrum analyses of the principal stresses (results not shown) and air temperature time series (Figure 2.8b) show two peaks, one at frequencies between 0.3 and 0.5 day^{-1} (synoptic scale) and the other at a frequency of 1 day^{-1} (diurnal cycle). The peak associated with synoptic variability is present during the entire record. The diurnal frequency peak in σ_1, σ_2, and surface air temperature is present after 4 February 2011 (JD 400), when the Sun rises above the horizon in the Viscount Melville Sound.

Fifteen days after the beginning of the melt season (JD 528), or two days after complete snow melt, we observed a change in the sign of the correlation between the diurnal cycle in surface air temperature and the recorded internal stresses, from negative (cooling leading to tensile stresses) to positive (cooling leading to compressive stresses) (see Figure 2.11). We interpret the timing of the change in the stress-temperature correlation as the onset of water infiltration through the ice. After this time, melt water

Figure 2.10: (a) Major (σ_1) and (b) minor (σ_2) principal stresses as a function of surface air temperature.

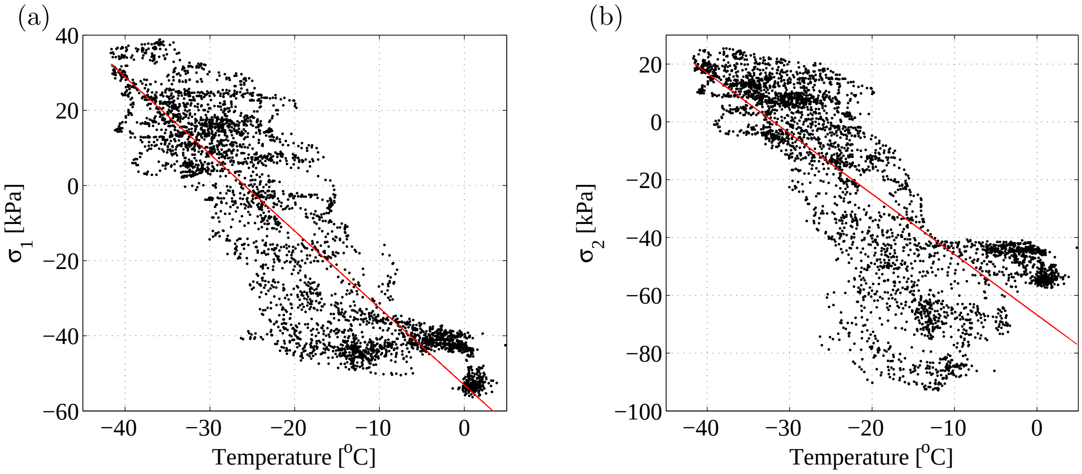

penetrating to the depth of the sensor freezes and expands during the night, causing compressive stresses recorded by the sensor (in a manner similar to the compressive stresses recorded when the stress sensor was set in ice on 10 October 2010).

Figure 2.11: Zoom in of the surface air temperature and observed first stress invariant ($\sigma_I = \frac{\sigma_1+\sigma_2}{2}$) (a) before and (b) after the start of the melt season. Note that the sign of the correlation between the two fields reverses between the two time period. We hypothesize that this reversal is due to the start of water infiltration within the sea ice.

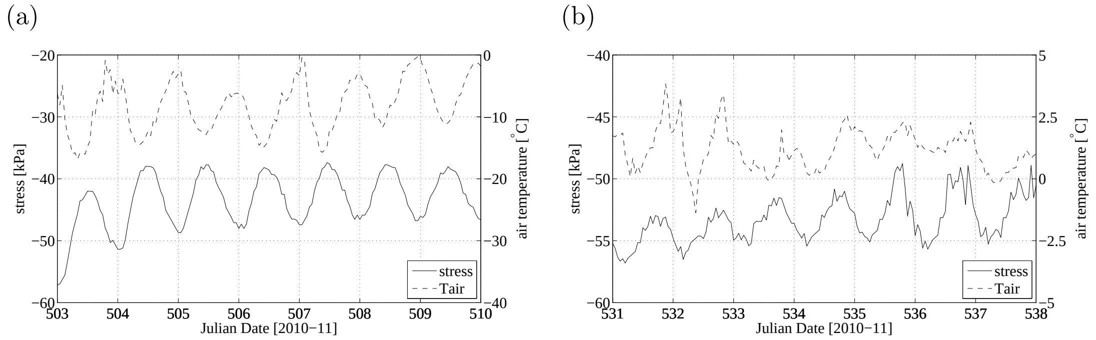

While the multi-year ice floe is drifting (JD 283 - 382), the thermal stresses are isotropic (σ_1 and σ_2 are approximately equal, see Figure 2.6a), in accord with the assumption made by *Lewis et al.* [1994], *Richter-Menge and Elder* [1998] and *Hutchings* *et al.* [2010]. In this case, the magnitude of the local normal stresses are the same in any reference coordinate system. Therefore, there are no significant shear stresses. During the landlocked season (JD 383 - 538), differences between the two principal stresses appear. During that period, we observe low frequency fluctuations in the band-pass filtered $\sigma_2 - \sigma_1$ that correlates with the band-pass filtered surface air temperature (r = -0.65 , see Table 2.2). This implies anisotropy in thermal stresses. In this case, the magnitude of the local normal stresses on two perpendicular planes is different in different reference coordinate systems and shear stresses are present (except on the principal stress axes, by definition).

Two possible factors can explain the difference in principal stresses after the onset of the landlocked season. The first is a preferred c-axis alignment of the sea-ice crystals in the direction of the surface ocean currents resulting in different Young's modulus and therefore different thermal stresses in the direction perpendicular and parallel to the coastline. The second is land confinement in the north - south direction, the direction perpendicular to the long axis of the channel.

The c-axis is the axis of the common crystal structure of sea ice, the direction in which the ice growth rate and the Young's Modulus is also largest. C-axis alignment has been observed in the Arctic in the Greenland Sea [*Tucker et al.*, 1987], Kara Sea [*Cherepanov*, 1971], Alaskan coastline [*Weeks and Gow*, 1980; *Kovacs and Morey*, 1978], Pond Inlet [*Stander and Bernard*, 1989] and in Allen Bay near Resolute [*Parsons et al.*, 1986]. *Weeks and Gow* [1978] propose that c-axis alignment could be used to derive the mean direction of surface ocean currents in perennially ice covered such as the CAA. When the c-axis of ice crystals aligns, the directional dependency of the Young's modulus becomes important, leading to differences in principal stresses.

A typical difference in principal stresses due to the preferred c-axis alignment is equal to $\Delta E \ \alpha \ \Delta T$, where ΔE [0.3E, *Schulson*, 1999] is the difference in Young's modulus in the direction parallel and perpendicular to the c-axis, α (5×10^{-5}) is the coefficient of thermal expansion and ΔT (-5°C, JD 450; Figure 2.6b) is a characteristic ice temperature change at the sensor depth. For a range of observed Young's Modulus between 0.3 and 10 GPa, this leads to a difference in principal stress ranging from 22.5 kPa to 750 kPa.

A typical difference in principal stress due to land confinement is equal to $E \frac{\Delta L}{L} = E \alpha \Delta T$, where ΔL is the thermal contraction of an ice slab of length L (170 km, the width of the channel) associated with a characteristic temperature drop ΔT (approximately -5°C). For a range of Young's Modulus between 0.3 and 10 GPa, this corresponds to differences in principal stress ranging from 75 kPa to 2500 kPa.

The stresses caused by both c-axis and land confinement are therefore large enough to explain the observed difference in principal stress during the landlocked ice season, peaking at 50 kPa on JD450. However, the orientation of the minimum principal stress (σ_2) with respect to the Geographic North Pole will be different in the two cases. In the case of the preferred c-axis alignment, the larger stress (in magnitude) will be in the direction parallel to the coastline (northwest-southeast), since this is the direction with the larger Young's modulus. This implies an angle of 45° between the minimum principal stress (σ_2) and the Geographic North Pole at the location of the ISB during the landlocked season when the stresses are tensile (see Figure 2.12). When the stresses are compressive, the angle between the minimum principal stress (σ_2) and the Geographic North Pole will be -45°.

In the case of land confinement during the landlocked season, basal friction between the ice and the ocean floor at the coastline will result in more positive (negative) stresses in the direction perpendicular to the coastline when the surface air temperature decreases (increases). This implies an angle of -45° between the minimum principal stress (σ_2) and the Geographic North Pole when the stresses are tensile and an angle of 45° between the minimum principal stress (σ_2) and the Geographic North Pole when the stresses are compressive (see Figure 2.12). The stress angle data from the ISB shows an angle of approximately -45° between σ_2 and the Geographical North Pole when the temperature decreases and the ice is under tensile stress (Figures 2.6a, 2.6b, 2.6c; JD 385 - 390, JD 408 - 445). When the ice is warming and under compressive stress, the angle turns to approximately 45° (Figures 2.6a, 2.6b, and 2.6c; JD 395 -

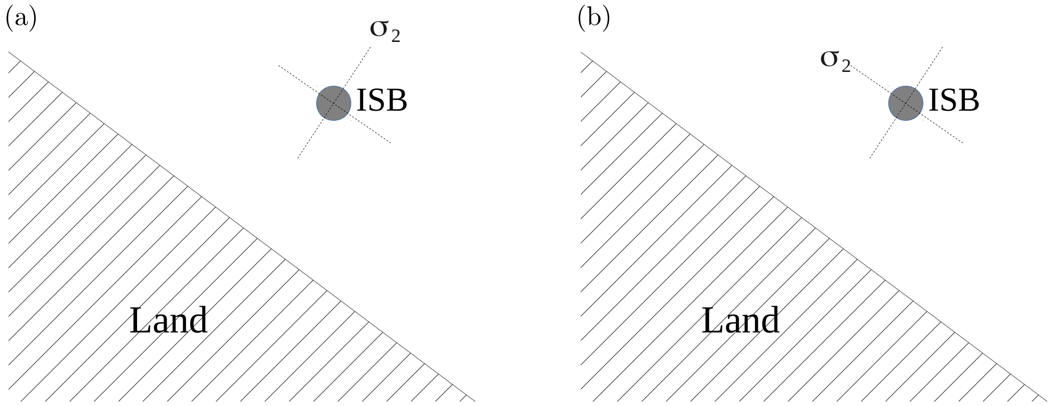

Figure 2.12: Direction of the minor principal stress (σ_2) with respect to the coastline for the case where c-axis alignment (a) and land confinement is responsible for the anisotropy. This is for the case where the surface air temperature is decreasing.

405, JD 450 - 460). Note that the angle data is not well defined in the drift seasons when the stresses are isotropic ($\sigma_1 = \sigma_2$) and there is no directional dependence. We conclude that land confinement, rather than c-axis alignment, is responsible for the difference in principal stresses.

We estimate the ice anchoring force by multiplying the difference in principal stress and by a typical ice thickness of first year ice. Assuming a first-year sea-ice thickness of approximately 2 m, the anchoring force ranges between 35 and -110 kN. Note that the principal stress axis reverse when the stresses change from compressive to tensile, since σ_1 and σ_2 are the minimum and maximum stresses.

Finally, why ISBs can record slowly varying (synoptic time scale) stresses induced by surface air temperature changes when they cannot record stresses induced by surface winds in the absence of fractures and floe collisions remains an open question.

2.4 Conclusions and Future Work

An internal Ice Stress Buoy (ISB) was deployed on multi-year ice in the Viscount Melville Sound on 10 October 2010. A nearly 9 months (10 October 2010 to 15 July 2011) internal sea-ice stress time series and 10 months (10 October 2010 to 17 August

2011) position record was collected. The GPS record from the ISB indicates that the landlocked ice season in the Viscount Melville Sound was approximately 5 months, from 18 January to 21 June 2011.

The observed stress data are highly correlated with changes in surface air temperature and not significantly correlated with the magnitude or the direction of the wind speed. This is in part explained by the smaller wind fetch, the attenuation of dynamic stress from the floe edge to its interior [e.g. *Tucker and Perovich*, 1992; *Richter-Menge and Elder*, 1998], but more importantly because ISBs record dynamic stresses induced by fracture and the resulting floe-floe collisions. The internal stress time series show a few dynamic stress events characterized by high-frequency changes in the recorded internal ice stresses associated with floe-floe collisions before the landlocked season between 10 October 2010 and 17 January 2011 (JD 283 - 382).

The magnitude of the internal thermal stress ranges between -84 and 66 kPa. The magnitude of the dynamic stresses range between -49 and 0 kPa. When the surface air temperature drops, tensile stress develops at the sensor depth (and compressive stress develops in the lower part of the ice slab). This is due to the thermal contraction in the upper part of the ice while the ice in contact with the surface ocean remains isothermal at the freezing point temperature.

Before the sea ice became landlocked, the internal thermal stresses were nearly isotropic. During the landlocked season, significant differences between σ_1 and σ_2 were recorded, yet σ_1 and σ_2 remained highly correlated with surface air temperature. This shows that thermal stresses in landlocked ice in the CAA are not isotropic.

We consider two possible causes to explain anisotropy in thermal stresses: preferred c-axis alignment in the ice crystal with surface ocean currents in coastal water leading to different material properties along and normal to the c-axis, and land confinement in the northeast-southwest direction associated with the nearby coastlines. The orientation of the principal stress time series with respect to the Geographic North Pole indicates that the effect of land confinement dominates over the effect of the c-axis alignment.

The internal ice stress time series also clearly shows the presence of residual compressive stresses at the beginning of the melt season when the sea-ice internal temperature is nearly isothermal. The observed internal stress time series suggests a viscous creep relaxation time scale of several days. Recall that a time period equal to four or five time constants are must be elapse for the residual stresses to return to zero in a simple first order differential equation of the form $\frac{\partial \sigma}{\partial t} = -\frac{1}{\tau}\sigma$, where τ is the relaxation time constant. This is longer than previously reported values in the literature (8 days compared with 5 days). This result is also supported by modeling evidence from a 1.5D thermal stress model (results presented in a companion paper in the same issue).

Results also show an interesting reversal in the sign of the correlation (from negative to positive) between diurnal fluctuations in surface temperatures and the recorded internal stresses 55 cm beneath the ice surface during the melt season. We attribute this change in the sign of the correlation to the onset of water infiltration within the the sea ice (at least to the depth of the sensor). This water freezes at night, expands and lead to compressive stresses at the sensor depth in a manner similar to the compressive stress that develops when the stress sensor first sets in after installation.

The relative magnitude of thermal stresses compared to the dynamic stresses in the CAA suggests that they may be important to consider in sea-ice rheological models developed for this region. Moreover, the anisotropy in internal stress induced by land confinement (or ice anchoring on nearby shores) leads to differences in internal stresses as large as 50 kPa when large changes in temperature occur. This again will have an impact on the mode of failure of landlocked ice, the shape of the landlocked ice edge, and the timing and location of landlocked ice onset and breakup in the CAA.

Future work addressing some of the questions that are raised in the present analysis should focus on deployment of ISBs on first-year landlocked ice to eliminate the added complexity of stress transmission between first-year and multi-year ice. In particular, measurements of internal stresses at different depth within first-year ice (above and below the zero thermal stress boundary within sea ice, as was done in multi-year ice by *Tucker and Perovich* [1992]; *Richter-Menge and Elder* [1998]) should be conducted to further test the hypothesis that ice anchoring on the shore line is responsible for anisotropy. We would expect the vertically integrated thermal stress in landlocked ice to be in tension (compression) when the surface air temperature cools (warms), as opposed to zero as in the case of coastal landfast ice that has a free boundary in the offshore direction. In addition, we propose to repeat the measurements in a different region of the CAA to confirm the results presented in this paper and to core sea ice to verify if c-axis alignment is indeed present in sea ice within the Archipelago. Finally, we suggest deploying several ice stress buoys on first-year ice in the same region to investigate the spatial variability of thermal and dynamic stress recorded by the stress sensor. We would expect to see a high correlation in thermal stress recorded by different buoys if there are no spatial variability in air temperature, wind, and snow cover depth. In multi-year ice, previous studies have shown that there is a wide variation in the magnitude between dynamic stresses measured even on the same floe a few kilometres apart. Whether this is also the case for thermal stresses measured in first-year ice remains an open question.

2.5 Response to the external examiner

External examiner comment 1: *Landlocked vs landfast.*

The thesis introduces the terms landlocked ice to describe a sub-category of landfast ice that is confined on multiple sides by landmasses. I find this to be a valuable concept that could be usefully applied outside the CAA, but I feel the term needs to be more clearly defined. For example, perhaps there is a minimum length of confining coastline or a maximum distance between landmasses in order for landfast ice to qualify as being landlocked (or some combination of these two parameters). After having been appropriately defined, I further recommend the term is used consistently throughout the following text. In its current form, the thesis appears to use the term landlocked and landfast interchangeably.

Response: We use the word 'landlock sea ice' for sea ice that is attached to land on more than one sides (channel, fjord, inlet, etc.). Landlock sea ice can be observed when the length scale in compression or shear is larger than the sea ice compressive or shear strength. For instance in the context of compressive failure (ridging), a domain of size L would have characteristic compressive stress equal to $\tau_a L = P^*$, where τ_a is surface air drag, L is length scale, and P^* is ice compressive strength. So landlock sea ice in this context is valid for domain size that are less than P^*/τ_a = 27,500 / 0.1 = 275 km. In the context of shear deformation, the characteristic stress would be equal to $\tau_a L = S^* = P^*/2e$, where S^* is shear strength and e is an aspect ratio of yeild curve. So landlock sea ice in this context is valid for domain size of $L = P^*/(2e\tau_a)$ = 27,500/2/2/0.1 = 70 km. Whether the smaller or larger length scale determines the presence or absence of landlock sea ice will depend on the geometry. For instance, the length scale for a channel will be determined by the shear deformation and that of a domain with solid boundaries on all four sides will be determined by the normal (ridge) deformation.

The term landfast was eliminated from the Chapter 4 in all places for consistency.

External examiner comment 2: *Refreezing and melting of ice around stress buoy.*

In the final sentence of the penultimate paragraph of page 18, the text states "The conceivable factors for degrading the measurement are the installation and the ice melting around the sensor". These are important considerations that I feel warrant greater attention. Specifically, from what is described in section 2.2.1, the stress buoy was deployed in an over-sized hole, which was flooded with seawater. Based on the dimensions stated in the text, this would have resulted in a 2.1-cm thick "jacket" of refrozen ice surrounding the sensor. Due to the enhanced rate of freezing within the hole and reduced exchange with the ocean below, this ice is likely to have had significantly higher bulk salinity than the surrounding ice floe. I feel it would be important to consider how this might affect the stress coupling between the sensor and the floe.

In addition to be surrounded by a jacket of higher porosity ice, the sensor itself will *have been prone to vertically conducting heat in and out of the ice floe. During the melt season, this will lead to enhanced melting around the sensor and I would therefore expect the sensor to create a preferential pathway for both heat and melt water. This could potentially amplify the diurnal signals observed in the stress record, particularly the "reverse" signal observed during the melt season. These mechanisms should also be discussed in the context of how they might affect the interpretation of certain features in the stress record, particularly diurnal variations.*

Response: This is an interesting point. We see no correlation between the wind stress and the measured internal ice stress. We only see internal sea ice stress recorded when deformation occur and floe-floe collision takes place. This alludes to the fact that the stresses are not being transmitted to the sensor for slowly varying surface air stresses and only for collision (much shorter time scales). I see two reasons for this type of behavior: viscous creep around the sensor that prevents the synoptic scale changes in winds to be transmitted and recorded by the buoy; or higher porosity in the jacket of sea ice that refroze around the sensor after deployment which prevents stresses from being transmitted. The in-situ derived viscous creep relaxation time constant from our measurements is 8 days, implying that some viscous creep will take place during the synoptic scale variation in surface winds. Since the synoptic time scale is not that much longer than the viscous creep relaxation time constant, we would still expect to see some correlation between the winds and the measured in-situ stresses. This suggests that viscous creep may not be responsible for this effect. However, as the refrozen ice around the sensor flushes its salt, we should see an increasingly good connection between the far away stress field and the recorded stress field at the buoy as the winter progresses. But we see no such things, again suggesting that this is not responsible for the observed lack of correlation between the surface wind stress and the recorded internal stress. All in all, we do not have a good explanation for this phenomenon. We are funded to deploy ice stress buoys along the Labrador coast in landfast sea ice. We will test the ISB in a block of salty ice at the National Research Center in Ottawa prior or after the deployment. We will do test with pure ice, salty ice and higher porosity ice within the refrozen ice jacket; and with salty ice and refrozen ice around the sensor that had time to drain its salt to regain the same salinity as the surrounding ice. We hope that these laboratory tests will help us answer these questions. This is work that will be done in the next year or two.

External examiner comment 3: *Tide cracks.*

At the top of the last paragraph on P31, the text indicates that "basal friction between the ice and the ocean floor at the coastline" is responsible for locking the ice to the land. While this may be accurate when the ice is compressed against the coast, it does not account for the presence of a tide crack, which will tend to decouple the floating ice from its grounded margin under tension. As a result, I would expect to see a greater level of anisotropy under compression than under tension and this appears to be what the stress record indicates during the landlocked season. Unfortunately, the dependence of σ_1 - σ_2 *on the sign of the principal stress is not discussed anywhere in the text. I recommend this relationship be discussed in the context of tide cracks at the boundaries of the landlocked ice.*

Instead, the text states there are "low frequency fluctuations in the band-pass filtered σ_1 - σ_2 *that correlates with the band-pass filtered surface air temperature". No mechanism is put forward that might explain this correlation and instead I suspect the correlation is actually related to the presence of the tide crack. That is, when the ice was warm it was under compression and the tide crack was closed, leading to a high level of anisotropic stress. On the other hand, when the ice was cold, it was under tension and the tide crack "relieved" some of the anisotropy. I recommend investigating whether the correlation between* σ_1 - σ_2 *and air temperature still holds if calculated separately for compressive and tensional events.*

Response: We thank the examiner for this comment. We do indeed see a higher correlation between the internal stress anisotropy and air temperature for cases when the temperature is warming (i.e. compressive stresses at the coast where the tidal crack is present) as suggested by the reviewer. We will re-run the model with the same boundary condition (i.e. no further deformation at land-fast ice onset in the direction perpendicular to the coastline) for cases when the temperature is warming and we will allow for some deformation when the temperature is cooling (tensile stress at the tidal crack). We will vary the fractional amount of axial deformation for cases when the temperature is cooling to best match the data. This will serve as a further proof of concept of this idea. We will write a note to JGR to describe the use of this new boundary condition and present the correlations between air temperature and stress anisotropy separately for cases with warming and cooling of the atmospheric temperature as well. We will invite the external examiner to be a co-author on this paper.

Chapter 3

A 1.5D anisotropic sigma-coordinate thermal stress model of landlocked sea ice in the Canadian Arctic Archipelago

A thermal stress model that simulates the anisotropic thermal stress observed in the Canadian Arctic Archipelago is presented in this chapter. This model is developed since the importance of thermal stress and its anisotropy are highlighted by the observation presented in Chapter 2 [*Hata and Tremblay*, 2015a]. This chapter consists of a paper published in the Journal of Geophysical Research: Hata, Y. and Tremblay, L. B. (2015), A 1.5D anisotropic sigma-coordinate thermal stress model of landlocked sea ice in the Canadian Arctic Archipelago, J. Geophys. Res., 120, **12**, p8251–8269, doi:10.1002/2015JC010820

A 1.5D anisotropic sigma-coordinate thermal stress model of landlocked sea ice in the Canadian Arctic Archipelago

Y. Hata [1], and L. B. Tremblay [1]

[1] Department of Atmospheric and Oceanic Science, 805 Sherbrooke Street West,
McGill University, Montreal, Quebec, Canada. H3A 0B9

Abstract

We present a 1.5D thermal stress model that takes into account the effect of land confinement, which causes anisotropy in thermal stresses. To this end, we fix the total strain in the direction perpendicular to the coastline to its value at landlocked ice onset. This prevents thermal expansion in the direction perpendicular to the coastline and therefore induces larger thermal stresses in this direction. The simulated stresses best match the observations, when a Young's Modulus of 0.5 GPa and a relaxation time constant of 8 days are used. This simulation gives root mean square errors of 13.0 kPa and 13.1 kPa ($\sim$15 %) in the major and minor principal stresses, respectively. The simulated anisotropic component of thermal stress also generally agrees with observations. The optimal Young's Modulus is in the low range of reported values in the literature and the optimal relaxation time constant (8 days) is larger than the largest relaxation time constant reported in the literature (5 days). A series of experiments are done to examine the model sensitivity to vertical resolution, snow cover, and the parameterizations of Young's Modulus and viscous creep. Results show that a minimum of one and three layers in the snow and ice, respectively, is required to simulate the thermal stresses within 15 % error of the value assessed with the higher resolution control simulation. This highlights the importance of resolving the internal snow and ice vertical temperature profile in order to properly model the thermal stresses of sea ice.

3.1 Introduction

Thermal stresses develop when gradients in temperature are present within a material. In sea ice, they result directly from changes in surface air temperature (e.g. diurnal, synoptic, and seasonal). Thermal stresses in sea ice are typically large because the basal ice temperature is fixed at the surface ocean freezing point temperature [*Schmidt et al.*, 2004] and also because the time scale for temperature adjustment within the ice [order of months, *Tremblay*, 1996] is relatively long compared to the diurnal and synoptic time scale and of the same order as seasonal time scales for thick ice, leading to large vertical temperature gradients locally. As a result, ice surface cooling results in tensile stresses in the upper part of an ice slab and compressive stresses in the lower part. When large thermal stresses are present, thermal cracking can trigger sea-ice ridging, lead opening, and shear failure [*Evans and Untersteiner*, 1971]. In fact, thermal stresses create a vertical structure on the depth-independent dynamic stress and reduce the critical dynamic stress that is required to induce ice failure and deformation. For this reason, thermal stresses can have a significant impact on the dynamics of sea ice, and should be considered in a complete sea-ice rheological model.

The importance of thermal stresses and in particular thermal (surface tension) cracks on the sea-ice rheology was recognized when the first realistic sea-ice dynamic model were constructed [*Coon et al.*, 1974]. *Milne* [1972] suggested that the spacing of pressure ridging in the Arctic Ocean could be explained by thermal pre-stressing and flexural stress in a flexural-gravity standing wave. Following *Milne* [1972], *Xie and Farmer* [1991] recorded under-ice noise using a three-dimensional array of hydrophones. The results show approximately one thousand thermal cracking events within a 1-km radius from 5.5 minute recordings conducted every 30 minutes over a period of 6 hours following a surface air temperature drop from 0°C to - 20°C. Their results show that the source of the noise was predominantly multi-year ice because of its low salinity and brittle nature [*Evans and Untersteiner*, 1971].

The first linear elastic thermal stress model was proposed by *Evans and Unter-*

steiner [1971] to study homogeneous axisymmetric ice slab. The model results show that thermal cracks can occur if the floe diameter is larger than 190 m for a 20°C temperature difference between the surface and basal ice temperature. Stress relaxation via viscous creep of ice is not included in their model, and therefore the diameter of floes that experience thermal cracking may be underestimated. *Bogorodsky et al.* [1972] developed an elastic thermal stress model to study the relationship between internal thermal stresses and changes in surface air temperature. Later, *Tucker and Perovich* [1992] compared their in-situ stress measurements with the simulated thermal stresses by the 1D model of *Bogorodsky et al.* [1972]. The model was in good general agreement with the observations, despite some discrepancies attributed to the absence of viscous creep relaxation in the model. Shortly after, *Lewis* [1993] developed a 1D thermal stress model that include viscous creep relaxation. The results from this model are in a good agreement with observed stresses from the Canadian Arctic Archipelago (CAA) [*Lewis et al.*, 1994]. *Lewis* [1995] also considered the effect of a pre-existing flaw on the internal stress state simulated by the model. His results show that the inclusion of flaws in the sea ice eliminates most of the high-frequency stress variations in better agreement with observations, but only when stresses are compressive.

In all the models developed until now, thermal stresses are assumed to be isotropic. *Hutchings et al.* [2010], however, state that this assumption still needs to be validated with measurements in the field. While this assumption is likely valid for the mobile pack ice, it may not be applicable to landfast sea ice in interior waters (i.e. landlocked sea ice) such as the CAA, where land confinement occurs and possibly c-axis alignment of the ice crystal structure is present [*Weeks and Gow*, 1980]. When land confinement or c-axis alignment is present, the major and minor principal stresses are not equal (anisotropic stress state). This gives rise to shear stresses on planes of all orientations, except those of the principal stresses (perpendicular and parallel to the axis of the channel). In the narrow passages of the CAA (see Figure 3.1), the larger principal stress (in magnitude) acts on a plane that is roughly parallel to the coastline, while the smaller principal stress acts on a plane that is roughly perpendicular to the coastline.

The difference in principal stresses can be as large as 50 kPa (Hata and Tremblay, paper in the same issue) and therefore is an important factor to consider when simulating the landlocked ice cover (e.g. the landlocked ice edge, its onset and break up).

Figure 3.1: Map of the Canadian Arctic Archipelago. The red dot indicates the location of the Ice Stress Buoy deployment.

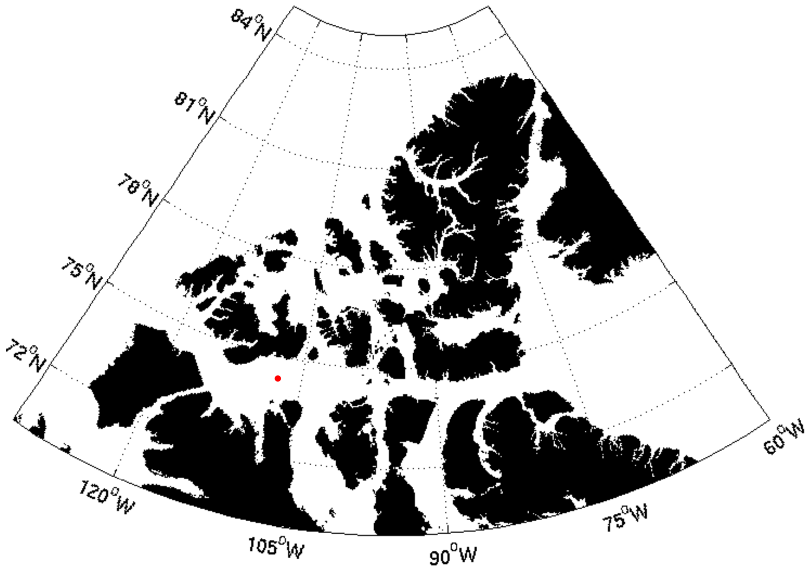

In this manuscript, we present a 1.5D anisotropic thermal stress model that takes into account the land confinement effect. Note that the anisotropy in this model does not arise because of anisotropy in material properties but rather because of change in the lateral boundary condition along the coastline when the ice is landlocked. The model is forced with the internal ice/snow temperature profile simulated by the sigma-coordinate multi-layer thermodynamic model of *Huwald et al.* [2005] and with a simple linear internal temperature profile. The simpler model is used to gain a better understanding of the sensitivity of the model with respect to ice stiffness (Young's Modulus), a parameter that is not constrained by observations. Our long-term goal is to develop a sea-ice rheological model that includes thermal effect as well as the effect of ice grounding along coastlines (land confinement). We hypothesize that such a model will better capture the dynamics of landlocked ice, including the onset, break up, and the temporal evolution of the landlocked ice edge during the cold season.

The outline of the manuscript is as follows. In section 3.2, we develop the governing equations for the 1.5D anisotropic thermal stress model. The atmospheric fields used to force the thermal stress model are presented in section 3.3. In section 3.4, we give a general description of the internal stress data collected in the Viscount Melville Sound of the CAA (Hata and Tremblay, paper in the same issue) that are used to validate the thermal stress model. Results from the thermal stress model forced with a simple linear and a full non-linear internal sea-ice temperature profiles are presented in section 3.5. Sensitivity studies of the anisotropic thermal stress model to the vertical resolution of the internal temperature profile, the snow depth, and the parameterizations of viscous creep and Young's Modulus are presented in section 3.6. The conclusions are summarized in section 3.7. Finally, an analytical solution for the thermal stress model forced with a linear internal temperature profile is presented in Appendix A.

3.2 A 1.5D anisotropic Sigma-Coordinate Thermal Stress Model

3.2.1 Model Equations

In the following, we present a 1.5D anisotropic thermal stress model describing the temporal evolution of horizontal internal ice stresses. This model allows for anisotropy in thermal stresses, induced by land confinement, by using different boundary conditions on the total strain in the direction perpendicular and parallel to the coastline. For the isotropic case ($\epsilon_{11} = \epsilon_{22}$, $\epsilon_{12} = 0$), this model reduces to the 1D isotropic thermal stress model of *Bogorodsky et al.* [1972].

The equation of motion for a linear elastic solid can be written as:

$$\nabla \cdot \boldsymbol{\sigma} + \mathbf{f} = \rho \mathbf{a}, \tag{3.1}$$

where $\boldsymbol{\sigma}$ is the internal ice stress tensor defined as:

$$\sigma_{ij} = \lambda\delta_{ij}\left(\epsilon_{11}^{mech} + \epsilon_{22}^{mech} + \epsilon_{33}^{mech}\right) + 2\mu\epsilon_{ij}^{mech}, \tag{3.2}$$

$\mathbf{f}$ is an external force vector, ρ is ice density, $\mathbf{a}$ is the acceleration, ϵ_{ij}^{mech} are the mechanical strain components acting on a plane normal to the i^{th} direction and in the j^{th} direction, λ and μ are the Lamé constants. The Lamé constants are defined as:

$$\lambda = \frac{E\nu}{(1+\nu)(1-2\nu)}, \tag{3.3}$$

$$\mu = \frac{E}{2(1+\nu)}, \tag{3.4}$$

where E is the Young's Modulus, and ν is the Poisson ratio. Assuming that plane stress theory is applicable [e.g., *Bogorodsky et al.*, 1972; *Lewis*, 1993, here presently], stresses acting on a given plane are independent from the stresses acting on a plane below or above. Substituting $\sigma_{33} = 0$ into equation (3.2), ϵ_{33} can be written as:

$$\epsilon_{33} = -\frac{\lambda}{\lambda + 2\mu}\left(\epsilon_{11} + \epsilon_{22}\right). \tag{3.5}$$

Therefore, equation (3.2) reduces to:

$$\sigma_{ij} = \delta_{ij}\frac{E\nu}{1-\nu^2}\left(\epsilon_{11}^{mech} + \epsilon_{22}^{mech}\right) + \frac{E}{1+\nu}\epsilon_{ij}^{mech}. \tag{3.6}$$

The numerical values of all constants used in the thermal stress model are listed in Table 3.1.

In equation (3.6), we define the i^{th} and j^{th} directions parallel and perpendicular to the coastline, respectively. Therefore, the i^{th} and j^{th} direction coincide with the principal stress axes.

The mechanical strain (ϵ^{mech}) in the ice can then be written in terms of the total

Table 3.1: Constants used in the simulation for sea ice (unless specified otherwise)

Variable	Symbol	Value(s)	Reference(s)
Thermal expansion coefficient	α	5.0×10^{-5} °C^{-1}	*Johnson and Metzner* [1990]
Young's Modulus	E	0.3 - 10 GPa	*Ji et al.* [2011]; *Timco and Weeks* [2010]; *Weeks and Assur* [1967]
Stress relaxation time constant	τ	8 hours - 5 days	*Sukhorukov* [1996]
Poisson Ratio	ν	0.33	*Timco and Weeks* [2010]
Thermal conductivity	k_i	2.03 Wm^{-1}K^{-1}	*Strum et al.* [2002]
Thermal conductivity (snow)	k_s	0.2 Wm^{-1}K^{-1}	*Strum et al.* [2002]

(ϵ^{tot}) and thermal (ϵ^{th}) strain as:

$$\epsilon_{ij}^{mech} = \epsilon_{ij}^{tot} - \epsilon_{ij}^{th} = \epsilon_{ij}^{tot} - \delta_{ij}\alpha\Delta\theta, \tag{3.7}$$

where δ_{ij} is the Kronecker delta operator, α is the coefficient of thermal expansion, and $\Delta\theta$ is the difference between the ice temperature ($\theta(z)$) and the reference temperature (θ_0), where z is the depth. The reference temperature, in this case, is the melting point temperature of pure ice (0°C).

Substituting equation (3.7) into equation (3.6), we obtain,

$$\begin{aligned}
\sigma_{11} &= \frac{E}{1-\nu^2}\left[\left(\epsilon_{11}^{tot} - \alpha\Delta\theta\right) + \nu\left(\epsilon_{22}^{tot} - \alpha\Delta\theta\right)\right], \\
\sigma_{22} &= \frac{E}{1-\nu^2}\left[\left(\epsilon_{22}^{tot} - \alpha\Delta\theta\right) + \nu\left(\epsilon_{11}^{tot} - \alpha\Delta\theta\right)\right], \\
\sigma_{12} &= \frac{E}{1+\nu}\epsilon_{12}^{tot}.
\end{aligned} \tag{3.8}$$

When all stresses are thermally induced (i.e. $\sigma_{ij} = \sigma_{ij}^{th}$), the total strain ($\epsilon_{ij}^{tot}$) is written as [assuming that the vertical integral of σ_{ij} is equal to zero, *Bogorodsky et al.*, 1972]:

$$\epsilon_{ij}^{tot} = \delta_{ij} \frac{\int_b^{s_i} E\alpha\Delta\theta dz}{\int_b^{s_i} Edz}, \tag{3.9}$$

where s_i and b are the ice surface and base elevations. For a constant E and α, the right hand side of equation (3.9) reduces to $\delta_{ij}\alpha\overline{\Delta\theta}$, where $\overline{\Delta\theta}$ is the vertical mean internal ice temperature departure from θ_0. During the drifting season, as opposed to the landlocked season, thermal stresses are assumed to be isotropic [*Richter-Menge and Elder*, 1998; *Hutchings et al.*, 2010]. In this case, equations (3.9) reduces to the isotropic thermal stress equations of *Bogorodsky et al.* [1972].

Note that the thermal stresses assuming plane stress theory can be calculated using equation (3.9) independently from the equation of motion (equation 3.1). Plane stress theory also implies that $\frac{\partial\sigma_{13}}{\partial z} = 0$, i.e., thermal stresses in one layer cannot be transmitted mechanically to another layers. We will show in section 3.5 that this assumption is not strictly valid for simulating stresses induced via high frequency (i.e., diurnal time scale) fluctuations in ice surface temperature. Considering the full equation of motion (equation 3.1) including shear stresses between layers (σ_{13}, σ_{23}) is beyond the scope of the present study and will be the subject of a future paper.

To represent the effect of land confinement during the landlocked season, we fix the total strain in the direction perpendicular to the coastline (ϵ_{22}^{tot}) to its value at the time of landlocked ice onset ($t = t_{onset}$), i.e., ice is no longer allowed to shrink/expand in the direction perpendicular to the coastline when it is landlocked because of basal friction or ice anchoring on the ocean floor at the coastline. Therefore, the total strain after the landlocked onset $\epsilon_{22}^{tot}(t \geq t_{onset})$ is written as:

$$\epsilon_{22}^{tot}(t \geq t_{onset}) = \epsilon_{22}^{tot}(t = t_{onset}). \tag{3.10}$$

Substituting equations (3.9) and (3.10) into equation (3.9), we write:

$$\sigma_{11}^{th} = \begin{cases} \dfrac{E}{1-\nu}\left[\dfrac{\int_b^{s_i} E\alpha\Delta\theta dz}{\int_b^{s_i} Edz} - \alpha\Delta\theta\right], & \text{drift season} \\ \dfrac{E}{1-\nu^2}\left[\left(\dfrac{\int_b^{s_i} E\alpha\Delta\theta dz}{\int_b^{s_i} Edz} - \alpha\Delta\theta\right) + \nu\left(\epsilon_{22}^{tot}(t = t_{onset}) - \alpha\Delta\theta\right)\right], & \text{landlocked season} \end{cases} \tag{3.11}$$

$$\sigma_{22}^{th} = \begin{cases} \dfrac{E}{1-\nu}\left[\dfrac{\int_b^{s_i} E\alpha\Delta\theta dz}{\int_b^{s_i} Edz} - \alpha\Delta\theta\right], & \text{drift season} \\ \dfrac{E}{1-\nu^2}\left[\left(\epsilon_{22}^{tot}(t = t_{onset}) - \alpha\Delta\theta\right) + \nu\left(\dfrac{\int_b^{s_i} E\alpha\Delta\theta dz}{\int_b^{s_i} Edz} - \alpha\Delta\theta\right)\right]. & \text{landlocked season} \end{cases} \tag{3.12}$$

Finally, in order to include stress relaxation via viscous creep, we differentiate the above equation with respect to time and add a simple relaxation term:

$$\frac{\partial\sigma^{tot}}{\partial t} = \frac{\partial\sigma^{th}}{\partial t} - \frac{1}{\tau}(\sigma^{tot} - \sigma_o), \tag{3.13}$$

where σ^{tot} is the total stress after viscous creep relaxation is included, τ is the viscous creep relaxation time constant, and σ_o is the reference state of stress. In this case, σ_o is assumed to be equal to 0 kPa. Note that the value of the total strain during the landlocked season ($\epsilon_{22}^{tot}(t \geq t_{onset})$) only affects the temporal evolution of the stresses through the viscous creep relaxation term.

This approach of including stress relaxation differs from the more complete representation of viscous creep by Lewis [1993] who writes:

$$\frac{\partial\sigma^{tot}}{\partial t} = \frac{\partial\sigma^{th}}{\partial t} - \text{CREEP}, \tag{3.14}$$

where

$$\text{CREEP} = Bexp\left(-\frac{Q}{RT}\right)\left[\frac{\sigma}{\left(1-\sqrt{P}\right)^2}\right]^n, \tag{3.15}$$

Q is the creep activation energy [Joules/mole], R is the gas constant [Joules/mole·K], T is the ice temperature [K], σ is stress [MPa], and P is the total porosity of the ice [unitless]. The sensitivity of the results to the exact form of the viscous creep parameterization is discussed in Section 3.6.

3.2.2 Boundary Conditions

We apply Neumann boundary conditions on the total stresses (σ_{ij}^{tot}) at the ice base and surface, i.e. $\frac{\partial \sigma_{ii}^{tot}}{\partial z} = 0$ at $z = b$ and $z = s_i$. A unique solution for the stress exists, despite the use of Neumann boundary condition at both ice base and surface, because of the additional constraint that the vertical integral of the thermal stresses without land confinement is equal to zero.

3.2.3 Coordinate Transformation

Following *Huwald et al.* [2005], we introduce a sigma coordinate transformation in the governing differential equation (3.13), for the temporal evolution of the internal thermal stress. When applying this transformation, an advection term naturally appears in the equation that takes into account the redistribution of internal stresses associated with relayering, ice growth and melt. This can be written mathematically as:

$$\tilde{z} = \frac{z - b}{s_i - b} \qquad \text{or} \qquad z = \tilde{z}(s_i - b) + b. \tag{3.16}$$

In this new coordinate system, $\tilde{z}$ is equal to 0 at the ice base and equal to 1 at the ice surface. We use the chain rule of differentiation and rewrite equation (3.13) in the sigma coordinate system as:

$$\frac{\partial \tilde{\sigma}^{tot}(\tilde{z}, \tilde{t})}{\partial \tilde{t}} \frac{\partial \tilde{t}}{\partial t} + \tilde{w} \frac{\partial \tilde{\sigma}^{tot}(\tilde{z}, \tilde{t})}{\partial \tilde{z}} = \frac{\partial \tilde{\sigma}^{th}(\tilde{z}, \tilde{t})}{\partial \tilde{t}} \frac{\partial \tilde{t}}{\partial t} + \tilde{w} \frac{\partial \tilde{\sigma}^{th}(\tilde{z}, \tilde{t})}{\partial \tilde{z}} - \frac{1}{\tau} \tilde{\sigma}^{tot}(\tilde{z}, \tilde{t}), \tag{3.17}$$

where

$$\begin{aligned}\tilde{w} &= \frac{\partial \tilde{z}}{\partial t} = \frac{1}{(s_i-b)^2}\left[(z-s_i)\frac{\partial b}{\partial t} - (z-b)\frac{\partial s_i}{\partial t}\right] = \frac{\tilde{z}-1}{s_i-b}\frac{\partial b}{\partial t} - \frac{\tilde{z}}{s_i-b}\frac{\partial s_i}{\partial t}, && (3.18)\\ \tilde{t} &= t, && (3.19)\end{aligned}$$

and $\tilde{z}$, $\tilde{t}$, $\tilde{w}$, and $\tilde{\sigma}$ are the transformed variables. Differentiating equation (3.18) with respect to $\tilde{z}$, we obtain:

$$\frac{\partial \tilde{w}}{\partial \tilde{z}} = \frac{1}{h_i}\frac{\partial b}{\partial t} - \frac{1}{h_i}\frac{\partial s_i}{\partial t} = -\frac{1}{h_i}\frac{\partial h_i}{\partial \tilde{t}}, \qquad (3.20)$$

where $h_i = s_i - b$. Multiplying equation (3.17) by ice thickness ($h_i = s_i - b$), equation (3.20) by σ^{tot}, equation (3.20) by σ^{th}, and adding all together, we obtain :

$$\frac{\partial(h_i\tilde{\sigma}^{tot})}{\partial \tilde{t}} + \frac{\partial(\tilde{w}h_i\tilde{\sigma}^{tot})}{\partial \tilde{z}} = \frac{\partial(h_i\tilde{\sigma}^{th})}{\partial \tilde{t}} + \frac{\partial(\tilde{w}h_i\tilde{\sigma}^{th})}{\partial \tilde{z}} - \frac{h_i}{\tau}\tilde{\sigma}^{tot}. \qquad (3.21)$$

$\tilde{\sigma}^{th}_{11}$ and $\tilde{\sigma}^{th}_{22}$ are written as:

$$\tilde{\sigma}^{th}_{11}(\tilde{z},\tilde{t}) = \begin{cases} \dfrac{E}{1-\nu}\left(\dfrac{\int_0^1 E\alpha\tilde{\theta}d\tilde{z}}{\int_0^1 Ed\tilde{z}} - \alpha\tilde{\theta}\right), & \text{drift season} \\ \dfrac{E}{1-\nu^2}\left[\left(\dfrac{\int_0^1 E\alpha\tilde{\theta}d\tilde{z}}{\int_0^1 Ed\tilde{z}} - \alpha\tilde{\theta}\right) + \nu\left(\dfrac{\int_0^1 E\alpha\tilde{\theta}(t=t_{onset})d\tilde{z}}{\int_0^1 Ed\tilde{z}} - \alpha\tilde{\theta}\right)\right], & \text{landlocked season}\end{cases} \qquad (3.22)$$

$$\tilde{\sigma}^{th}_{22}(\tilde{z},\tilde{t}) = \begin{cases} \dfrac{E}{1-\nu}\left(\dfrac{\int_0^1 E\alpha\tilde{\theta}d\tilde{z}}{\int_0^1 Ed\tilde{z}} - \alpha\tilde{\theta}\right), & \text{drift season} \\ \dfrac{E}{1-\nu^2}\left[\left(\dfrac{\int_0^1 E\alpha\tilde{\theta}(t=t_{onset})d\tilde{z}}{\int_0^1 Ed\tilde{z}} - \alpha\tilde{\theta}\right) + \nu\left(\dfrac{\int_0^1 E\alpha\tilde{\theta}d\tilde{z}}{\int_0^1 Ed\tilde{z}} - \alpha\tilde{\theta}\right)\right], & \text{landlocked season}\end{cases} \qquad (3.23)$$

where $\tilde{\theta}$ is the coordinate transformed variable of θ.

Finally the boundary condition is rewritten in terms of $\tilde{\sigma}^{tot}_{ij}$ and the transformed coordinate $\tilde{z}$ as:

$$\frac{\partial \tilde{\sigma}^{tot}_{ij}}{\partial \tilde{z}} = 0, \qquad (3.24)$$

at $\tilde{z} = 0$ and $\tilde{z} = 1$. In the following, we drop the tilde notation for clarity.

3.2.4 Numerical Scheme

We use an explicit forward in time numerical scheme to solve equations (3.21) numerically on a C-grid with initial condition $\sigma^{tot} = \sigma^{th} = 0$ at t = 0. All scalar quantities (σ_{ij}^{tot}, σ_{ij}^{th}, θ) are defined at the grid center, and the vertical velocities (w) are defined on the node of the grid cells (see Figure 3.2). Following *Huwald et al.* [2005], two additional stresses are defined at the ice base ($\tilde{z} = 0$) and surface ($\tilde{z} = 1$) for a natural handling of the boundary condition. The Neumann boundary conditions at the ice base and surface are calculated using a second order one-sided finite difference scheme.

Figure 3.2: Schematics of the numerical grid. All tracers quantities ($\tilde{\theta}_n$, $\tilde{\sigma}_n^{tot}$, and $\tilde{\sigma}_n^{th}$) are defined at the grid center and the advective velocities associated with re-gridding ($\tilde{w}_n$) are defined at the grid nodes. n is an arbitrary number between 1 and N, where N is the number of ice layers. The forcing fields ($\tilde{\theta}_n$, $\tilde{w}_n$) are calculated using the 1D multi-layer sigma-coordinate thermodynamic model of *Huwald et al.* [2005].

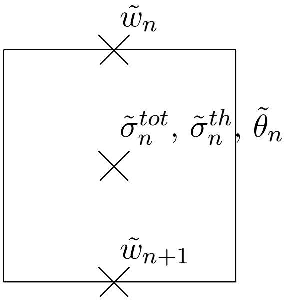

3.3 Forcing

The anisotropic thermal stress model is run offline (uncoupled) using the internal ice temperature profile from the 1D multi-layer sigma-coordinate thermodynamic sea-ice model of *Huwald et al.* [2005]. The full coupling of the thermodynamic and thermal stress model is left for future work. We apply a Neumann boundary condition at the ice or snow surface (sum of all surface heat fluxes, radiative, turbulence, and conductive heat fluxes, equal to zero) and fixed basal ice temperature equal to -1.8°C — the freezing point temperature of ocean water at 29 psu. The 1D thermodynamic model is forced with surface heat fluxes from the Canadian Meteorological Center's (CMC) Global Deterministic Prediction System (GDPS) [*Smith et al.*, 2013]. The snow, cold ice, and warm melting ice albedo are set equal to 0.9, 0.85, and 0.55, respectively. The choice of a warm ice albedo is based on a validation study using the same model and data from previous Ice Mass balance Buoy (IMB) deployments in the same region and at the same latitude (76° N) (results not shown). In all simulations (unless otherwise specified), the model uses ten vertical layers each in the snow and ice, and the snow depth (h_s) is set to a constant (h_s =13 cm) during the winter season. The optimal snow depth is set by minimizing the error between the simulated and observed internal ice temperature at the sensor depth (see section 3.5 for details). During the summer melt season, the temporal evolution of the snow depth is calculated from the imbalance of the surface heat fluxes (radiative, turbulence, and conductive heat fluxes).

3.4 Internal Ice Stress Data

The internal stress data that we use for the model validation were collected in the Viscount Melville Sound of the CAA from 10 October 2010 to 17 August 2011. The data, measured by an Ice Stress Buoy (ISB — manufactured by the Cold Regions Research and Engineering Laboratory), include the 2D horizontal major and minor principal stresses, the angle between the minor principal stress and the geographic North Pole, the 1-m air temperature, the ice temperature at the stress sensor depth (55 cm from the ice surface), and the Geographical Position System (GPS) location. The ISB was deployed on a highly deformed multi-year ice floe with the presence of old ridges and refrozen melt pond. The ice thickness at the buoy site was 1.87 m with large spatial variation in thickness over small distances. The ice thickness measured only a few meters away from the ISB was 3.35 m. The buoy data were transmitted through the ARGOS satellite system every hour until the buoy stopped transmitting on 17 August 2011.

The internal stress data, recorded by the buoy, is dominated by thermal stresses induced by diurnal, synoptic and seasonal variations in temperature, with only a few dynamic stress events characterized by higher frequency fluctuations (see Figure 3.3). This is in contrast with previous observations made in the Arctic Ocean where high-frequency fluctuations are an ubiquitous feature of the internal stress time series [e.g. *Tucker and Perovich*, 1992; *Richter-Menge and Elder*, 1998; *Hutchings et al.*, 2010]. The GPS data indicates three main dynamical regimes during the nearly 10 months record: two drifting periods from 10 October 2010 to 17 January 2011 and from 23 June to 17 August 2011, and a landlocked period from 18 January to 22 June 2011.

Figure 3.3: (a) Time series of major (σ_1: red line) and minor (σ_2: blue line) principal stresses, and (b) 1-m air (blue line) and wire (red line) temperatures. The gray shading and white area below each figures indicate the drift and landlocked seasons, as per the GPS and compass angle records from the buoy (see Hata and Tremblay in the same issue for detail).

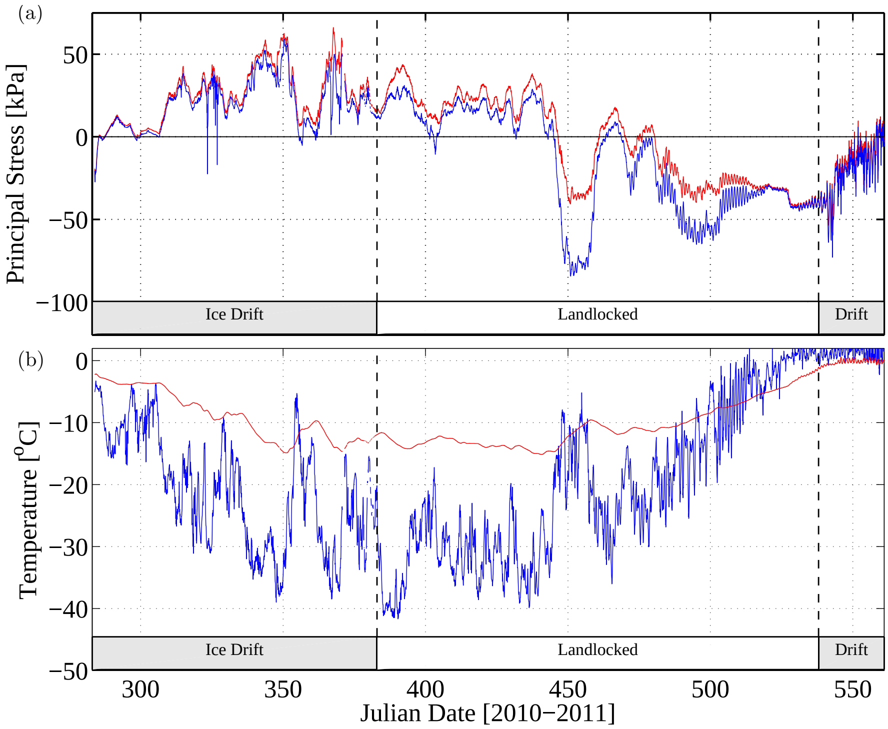

The thermal stress record during the first drift season is isotropic with the two principal stresses equal to one another, as is usually assumed in previous studies reporting internal sea-ice stresses from similar buoys in the Arctic Ocean. The thermal stress record during the landlocked ice season, however, is not isotropic. Analysis of the internal stress record suggests that land confinement in the north-south direction is responsible for the anisotropy — with smaller effects from the c-axis alignment in sea ice if at all present (Hata and Tremblay, paper in the same issue). In fact, the proximity of the land prevents thermal expansion (or contraction) of the sea ice in the direction perpendicular to the coastline. Near the end of the landlocked season, when the surface air temperature reaches 0°C, the internal stresses are again isotropic. We hypothesize that the ice is too weak at near zero temperature to adhere to the land effectively. The internal stress time series also show a residual compressive stress at the end of the winter season (beginning of the melt season) that relaxes to zero after approximately 20 days. This suggests a relaxation time constant (τ) of several days (Hata and Tremblay, paper in the same issue).

3.5 Model Results

In this section, we present the results from the anisotropic thermal stress model and use observed stress data from the ISB (see section 3.4) to derive model parameters and atmospheric forcing fields that are not well constrained by existing observations. These include the snow depth (h_s), the viscous creep relaxation time constant (τ), the Young's Modulus (E), and the exact depth of the stress sensor. The snow depth is determined by minimizing the error between simulated and observed ice temperature at the sensor depth. τ is derived from the exponential decay of the residual compressive stresses at the beginning of the melt season when the ice internal temperature is isothermal and equal to the melting point temperature. Finally, E and sensitivity of the results to the exact vertical position of the sensor are discussed using an analytical solution of equation (3.37) (see Appendix A).

The 1.5D thermal stress model contains four physical constants: the Young's Modulus (E), the thermal expansion coefficient (α), the Poisson ratio (ν), and the viscous creep relaxation time constant (τ). Of those four physical constants, α and ν are well constrained by observations [*Johnson and Metzner*, 1990; *Timco and Weeks*, 2010], and E and τ are not well constrained.

E can vary from 0.3 to 10 GPa [*Ji et al.*, 2011; *Timco and Weeks*, 2010; *Weeks and Assur*, 1967], and the viscous creep relaxation time constant (τ) — the time required for a given stress state to decrease by a factor of e^{-1} — ranges from 8 hours to 111 hours ($\sim=$ 5 days) [values reported in: *Sukhorukov*, 1996]. For both E and τ, the measured values depend on ice type, temperature, and measurement methods. For τ specifically, the value depends also on the strain rate [*Schulson*, 1999; *Lewis*, 1993]. There is also a strong coupling between the value of E and τ. For instance, a smaller value of τ means a faster relaxation of the thermal stress. Therefore, a larger value of E will be required in order to simulate fluctuations in σ that are of similar magnitude, for a given perturbation in surface temperature — and vice versa.

Two additional sources of uncertainty in the model validation include the snow depth at the ISB site and the exact depth of the stress sensor (error of ± 5 cm). The uncertainty associated with the depth of the stress sensor is discussed at the end of this section. The snow depth is inferred from the comparison of the simulated internal sea-ice temperature with the measured ice temperature at the sensor depth (55 cm from ice surface). Note that the thermistor is attached to the steel cylinder with a high thermal conductivity (24 $\mathrm{Wm^{-1}K^{-1}}$) and reacts almost instantly to changes in temperature (time constant of 40 seconds for a cylinder wall thickness of 1.6 cm, heat capacity of 450 J $\mathrm{kg^{-1}\ K^{-1}}$, and density of 8000 $\mathrm{kg/m^3}$). Simulation results from the 1D multi-layer sigma-coordinate thermodynamic model show that a snow depth of 13 cm at the ISB site gives the best match with the ice temperature measured at the sensor depth (see Figure 3.4). In the following, we assume a constant snow depth during the entire winter season for simplicity and because snow falls early in the season in this region [*Warren et al.*, 1999].

The viscous creep relaxation time constant can be determined explicitly from look-

Figure 3.4: Observed (black line) and simulated internal ice temperatures at the sensor depth (-55 ± 5 cm, gray lines) using the 1D multi-layer sigma-coordinate thermodynamic model *Huwald et al.* [2005] forced with observed 1-m surface air temperature and 13 cm snow.

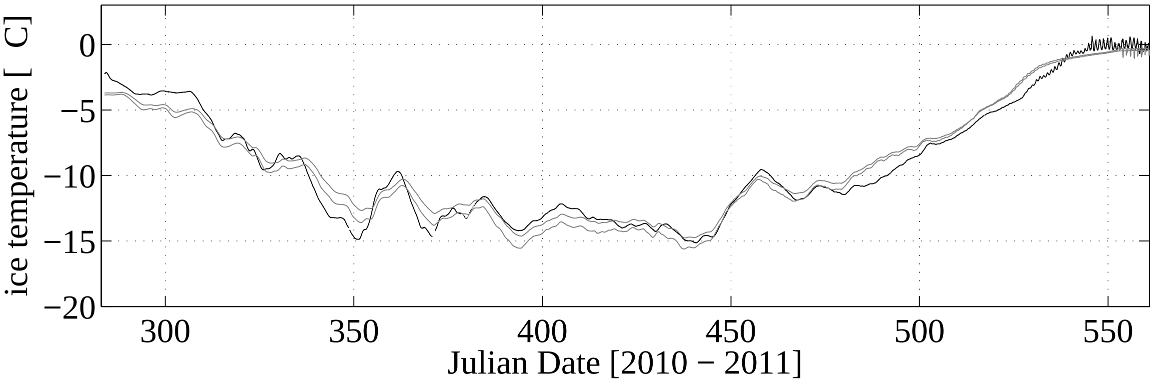

ing at the relaxation of the residual compressive stress at the beginning of the melt season. At this time, the internal sea-ice temperatures are near 0°C at all depths, and equation (3.13) reduces to a simple ordinary differential equation with an exponential decay solution. Figure 3.5 shows a zoom-in on this time period, from JD 540 to 561, for different τ values. We conclude from these results that the relaxation time constant is approximately equal to 8 days (by visual inspection of Figure 3.5).

Figure 3.5: Simulated stress relaxation for different viscous creep relaxation time constants (see inset) from the residual compressive stress of -30 kPa starting at the beginning of the melt season (JD 544). The observed major/minor, and 3-day running mean principal stresses are shown in the background in thin and thick black lines, respectively.

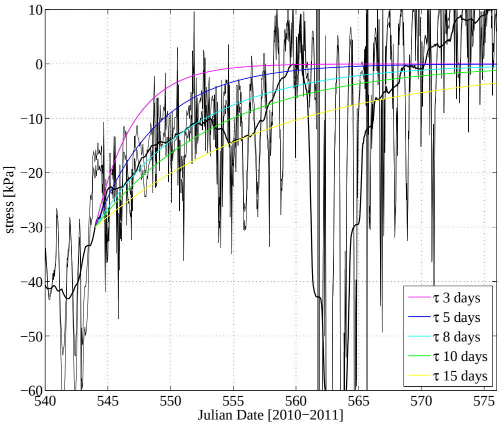

In order to get an estimate of the Young's Modulus from the observed internal stresses, we now consider a simple seasonal cycle in surface air temperature and a linear internal snow and ice temperature profile forcing the thermal stress model. The linear temperature profile assumption (i.e. ice has negligible heat capacity) is valid for low frequency fluctuations in surface air temperature such as the seasonal cycle. Using this model, we derive a simple analytical solution for σ_1 and σ_2 (see Appendix A, equation 3.37) that allow us to study the sensitivity of the simulated internal stresses to the Young's Modulus E, and to study the sensitivity of the recorded internal ice stress as a function of the sensor depth. We will see below that the estimate of the Young's modulus derived using the simple linear temperature profile assumption also gives a good match between observed and simulated stresses when the model is forced with the full 1D multi-layer sigma-coordinate thermodynamic model.

Assuming a constant Young's Modulus, a constant thermal expansion coefficient, and a surface temperature perturbation of the form $\theta_s = \Delta T sin(\omega t)$, where $\omega = \frac{\pi}{\mathfrak{T}}$ is the frequency, $\mathfrak{T}$ is the length of the winter season (262 days, see Figure 3.3b), and ΔT is the amplitude of the seasonal cycle in temperature (-40°C: see Figure 3.3b), the solution of equation (3.13) for the anisotropic and isotropic cases can be written as (see Appendix A):

$$\sigma(t) = K(z) E \frac{\omega\tau}{(\omega\tau)^2 + 1} \Delta T \left[cos(\omega t) + \omega\tau sin(\omega t) - e^{-\frac{t}{\tau}} \right], \tag{3.25}$$

where

$$K(z) = \begin{cases} -\dfrac{\alpha}{1-\nu^2} \dfrac{1}{1 + k_i h_s / k_s h_i} \left(\dfrac{1}{2} + \dfrac{z}{h_i} + \nu \left(1 + \dfrac{z}{h_i} \right) \right), & \text{direction parallel to the coastline,} \\ -\dfrac{\alpha}{1-\nu^2} \dfrac{1}{1 + k_i h_s / k_s h_i} \left(1 + \dfrac{z}{h_i} + \nu \left(\dfrac{1}{2} + \dfrac{z}{h_i} \right) \right), & \text{direction perpendicular to the coastline,} \\ -\dfrac{\alpha}{1-\nu} \dfrac{1}{1 + k_i h_s / k_s h_i} \left(\dfrac{1}{2} + \dfrac{z}{h_i} \right), & \text{isotropic,} \end{cases}$$

k_i and k_s are thermal conductivities of ice and snow, t is time starting at t = 0 on

JD 283, h_s is the snow depth, and h_i is the sea-ice thickness. In the limit when the frequency of the temperature perturbation is small compared to the relaxation time constant ($\omega\tau \ll 1$; valid for the seasonal cycle of surface temperature), equation (3.25) reduces to:

$$\sigma^{tot}(t) = K(z)E\Delta T\left(\frac{\omega}{k}\right)\left[cos(\omega t) - e^{-\frac{t}{\tau}}\right]$$

or

$$E = \frac{\sigma^{tot}(t)}{K(z)\Delta T(\omega\tau)\left[cos(\omega t) - e^{-\frac{t}{\tau}}\right]}. \tag{3.26}$$

At the beginning of the melting season (t = 262), we observed a residual compressive stress of approximately σ^{tot} = -30 kPa, induced by a combination of the seasonal cycle in temperature and viscous creep (see Figure 3.3). Substituting these values into equation (3.26) with the time of the melt onset t = 262 days, a relaxation time constant τ = 8 days and a sensor depth z = -0.55 m, we obtain an estimate of the Young's Modulus E = 0.8 GPa for the isotropic case, and E = 0.3 - 0.5 GPa for the anisotropic case (Figure 3.6).

Anisotropy in sea ice (or land confinement) leads to larger thermal stresses in both direction, parallel and perpendicular to the coastline (see Figure 3.7). In the direction perpendicular to the coastline, ice anchoring on the ocean floor at the coastline increase the tensile (compressive) stress when the sea ice cools (warms). In the direction parallel to the coastline, the stresses are also affected, to a lesser degree, via the Poisson effect (ν =0.33, see also equations 3.11 and 3.12). For this reason, an estimate of the Young's Modulus derived from a purely isotropic model will be larger (see also Figure 3.6). We conclude from these results that the optimal value of E will lie around 0.5 GPa, closer to the estimate derived from the anisotropic model.

Figure 3.7 shows the simulated internal thermal stresses at the sensor depth from the 1.5D thermal stress model, forced with a linear internal temperature profile and si-

Figure 3.6: Optimal values of the Young's Modulus and viscous creep relaxation time constant, that minimize the error between the simulated and observed residual stress of -30 kPa at the beginning of the melt season (JD 544). These curves are derived from equation (3.26), for a model forced with a linear temperature profile and sinusoidal seasonal cycle in surface air temperatures.

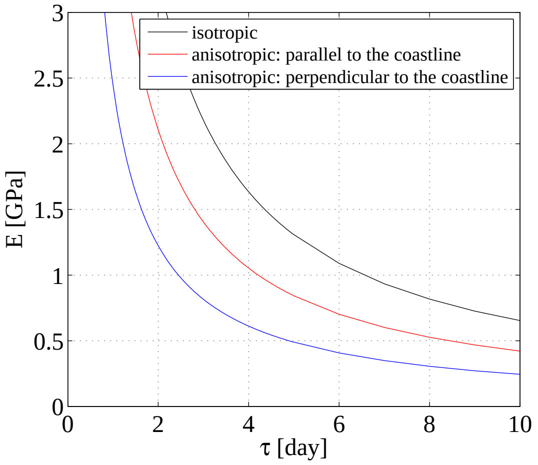

nusoidal surface air temperature (equation 3.37) for the three optimal values of Young's Modulus, $E = 0.3$ GPa, $E = 0.5$ GPa, and $E = 0.8$ GPa, derived above. In these simulations, the model is run in the isotropic mode (i.e. without land confinement) during the first drift season (JD283 - 383) and in the anisotropic mode (i.e. with land confinement) after the landlocked onset (JD 384 - 561). The best match between the simulated and observed seasonal cycle of internal stresses is indeed obtained with a Young's Modulus of around 0.5 GPa. Note that the simulated thermal stress at the beginning of the time series reaches its peak value earlier than the observed record. This is due to the fact that we have forced the model with a linear internal temperature profile. As such, the internal temperatures react instantaneously to changes in surface forcing at the beginning of the winter season, unlike an internal temperature profile derived from a thermodynamic model including thermal inertia (see Figure 3.7 and discussion below). Note again that the anisotropic thermal stresses at the sensor depth during the landlocked season, when land confinement is present, are larger in both perpendicular and parallel to the coastline.

Figure 3.8 shows the internal thermal stresses from the model forced with the

Figure 3.7: Observed stresses (σ_1: thin red, σ_2: thin blue) and analytical solution (σ_1: bold red, σ_2: bold blue) of the principal stresses at the sensor depth (-0.55 m) calculated from equation (3.13) and forced with a sinusoidal seasonal surface temperature for, a Young's Modulus of (a) 0.3 GPa, (b) 0.5 GPa, and (c) 0.8 GPa. In all cases, a relaxation time constant of 8 days is specified. During the first drift season (JD 283-383), the isotropic thermal stress model is used; after the landlocked onset (JD 384-561) the anisotropic thermal stress model is used. Note that σ_1 and σ_2 are shown here for easier comparison with the observation, despite the fact that equation (3.13) gives the stresses parallel (σ_{11}) and perpendicular (σ_{22}) to the coastline.

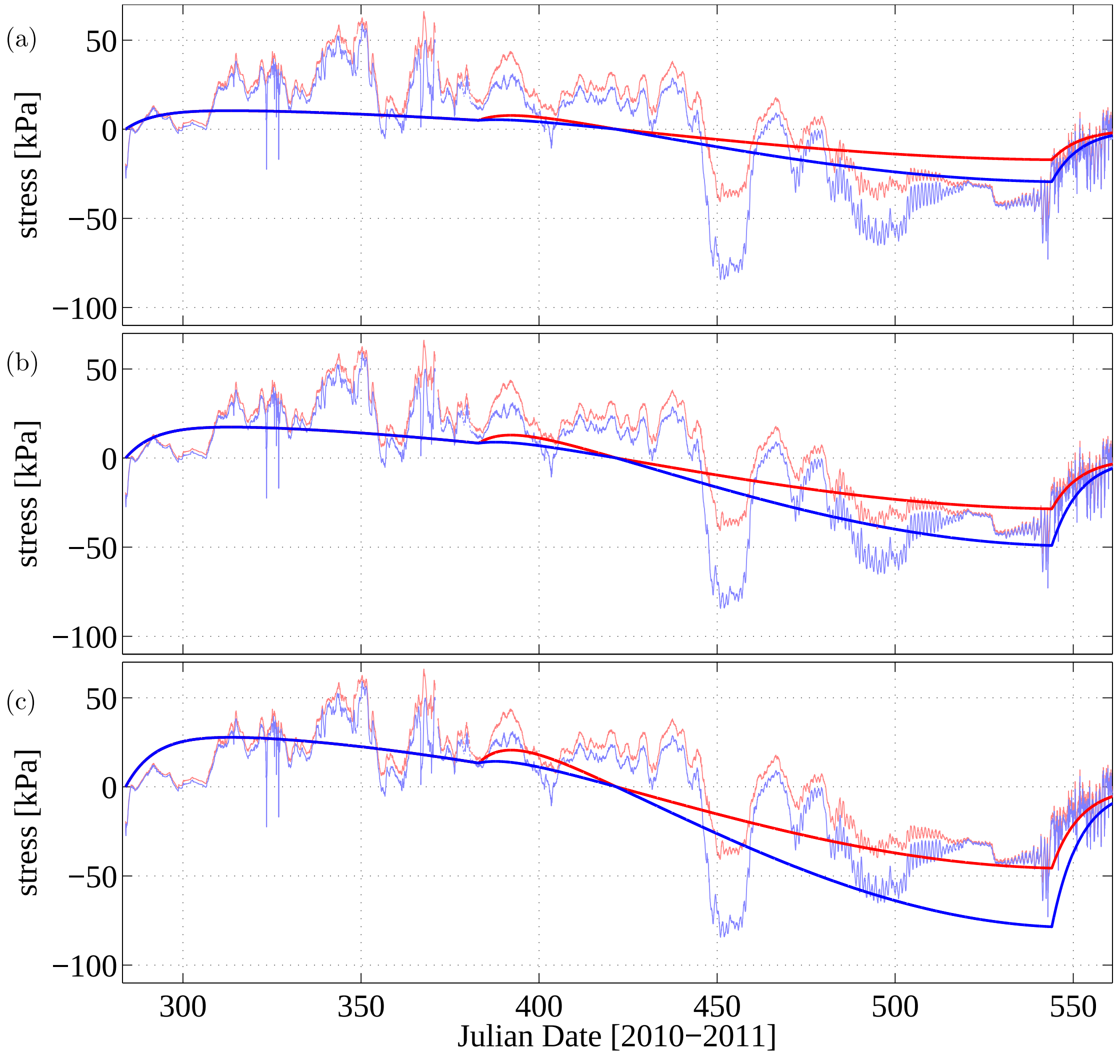

full non-linear internal temperature profile and $E = 0.5$ GPa. In general, the model simulates well seasonal and synoptic scale variability except for a bias low in the earlier drifting season suggesting a longer viscous creep relaxation time constant. The root mean square errors between simulated and measured σ_1 and σ_2 are 13.0 kPa and 13.1 kPa, respectively. The correlation (r) between measured and simulated major and minor principal stresses are 0.88 and 0.90, respectively — statistically significant at the 99 % level.

Note that, in the observation, diurnal fluctuations in temperature are not present at the sensor depth, yet, diurnal fluctuations in thermal stresses still exist. In the model and forcing, diurnal fluctuations in both temperature and stresses are absent at the sensor depth. This is particularly visible after JD 450 when diurnal fluctuation of ice surface temperature are significant and snow is present on the ice surface (see figure 3.8). There are two mechanisms by which high frequency fluctuations in thermal stresses can penetrate at a depth where fluctuations in temperature are not present. First, via the total strain (see equation 3.9), since the total strain is the function of the integral of the thermal strain from the ice base to the ice surface. Second, via mechanical stress transmission from the surface to the ice interior by the term $\frac{\partial \sigma_{13}}{\partial z}$ and $\frac{\partial \sigma_{23}}{\partial z}$ in equation (3.1).

In the present 1.5D thermal stress model and other 1D thermal stress models [e.g., *Bogorodsky et al.*, 1972; *Tucker and Perovich*, 1992; *Lewis*, 1993], surface thermal stress transmission via the total strain is included but mechanical stress transmission is neglected. The fact that the simulated magnitudes of the diurnal fluctuations at the sensor depth are much smaller than observed suggests that mechanical transmission is important at least for simulating stresses induced by diurnal fluctuations in surface temperature. Note that it might also be important for lower frequency surface temperature fluctuations (e.g., synoptic and seasonal scale fluctuations). This is beyond the scope of the present study and will be the subject of a future paper.

In Figure 3.9, we also show a simulation with a typical observed mid-range value of $E = 3$ GPa and an optimal relaxation time constant for this Young's Modulus of

Figure 3.8: (a) Observed (σ_1: bold red, σ_2: bold blue) and simulated (σ_1: thin red, σ_2: thin blue) principal stresses at the sensor depth (-0.55 m) and (b) simulated σ_1 as a function of depth. During the first drift season (JD 283 - 383), the simulated stresses are from the isotropic thermal stress model (i.e. without land confinement). After the landlocked sea-ice onset (JD 384 - 561), the stress are from the anisotropic thermal stress model (i.e. with land confinement) even after JD 517 when the surface air temperature first reaches 0°C and the internal thermal stresses are isotropic again. In all simulations, the 1.5D thermal stress model is forced with the internal ice temperature profile simulated by the multi-layer sigma-coordinate thermodynamic model of *Huwald et al.* [2005] with a 13 cm snow cover. The thermal stress model uses a Young's Modulus of 0.5 GPa and a relaxation time constant of 8 days.

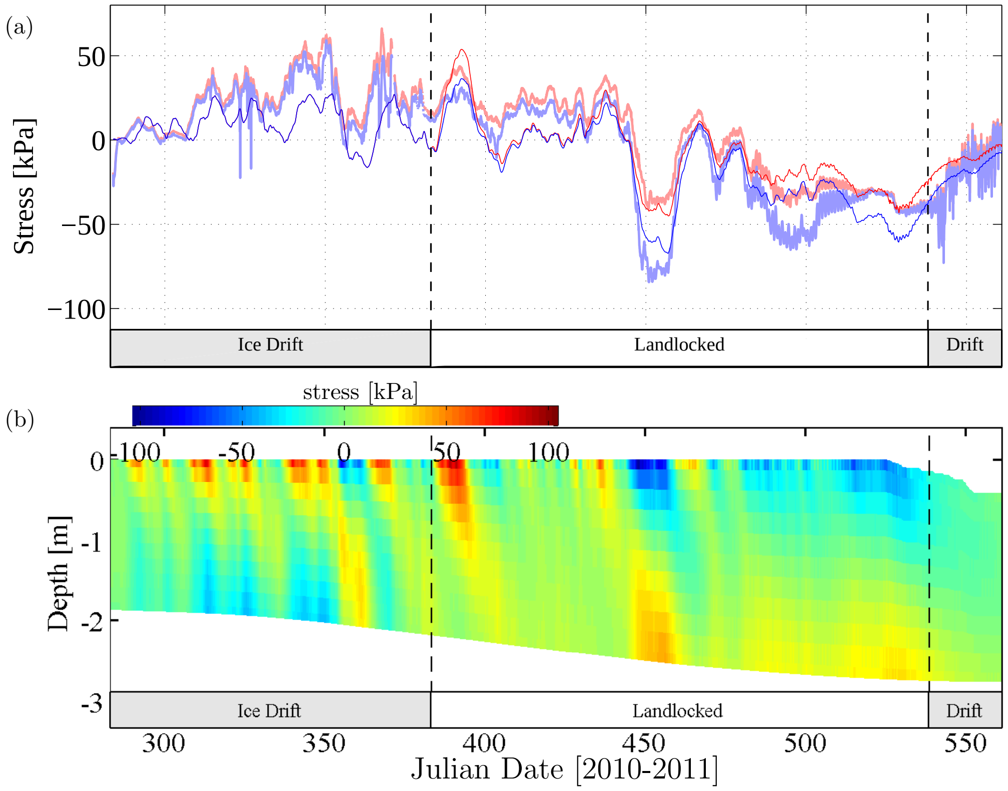

one day (See Figure 3.6) to clearly demonstrate the point that landlocked sea ice in the CAA have E and τ values that are at the low end or outside the range of reported values in the literature.

Figure 3.9: Observed (σ_1: bold red, σ_2: bold blue) and simulated (σ_1: thin red, σ_2: thin blue) principal stresses at the sensor depth (-0.55 m). During the first drift season (JD 283 - 383), the simulated stresses are from the isotropic thermal stress model (i.e. without land confinement). After the landlocked sea-ice onset (JD 384 - 561), the stress are from the anisotropic thermal stress model (i.e. with land confinement) even after JD 517 when the surface air temperature first reaches 0°C and the internal thermal stresses are isotropic again. In all simulations, the 1.5D thermal stress model is forced with the internal ice temperature profile simulated by the multi-layer sigma-coordinate thermodynamic model of *Huwald et al.* [2005] with a 13 cm snow cover. The thermal stress model uses a Young's Modulus of 3 GPa and a relaxation time constant of 1 days.

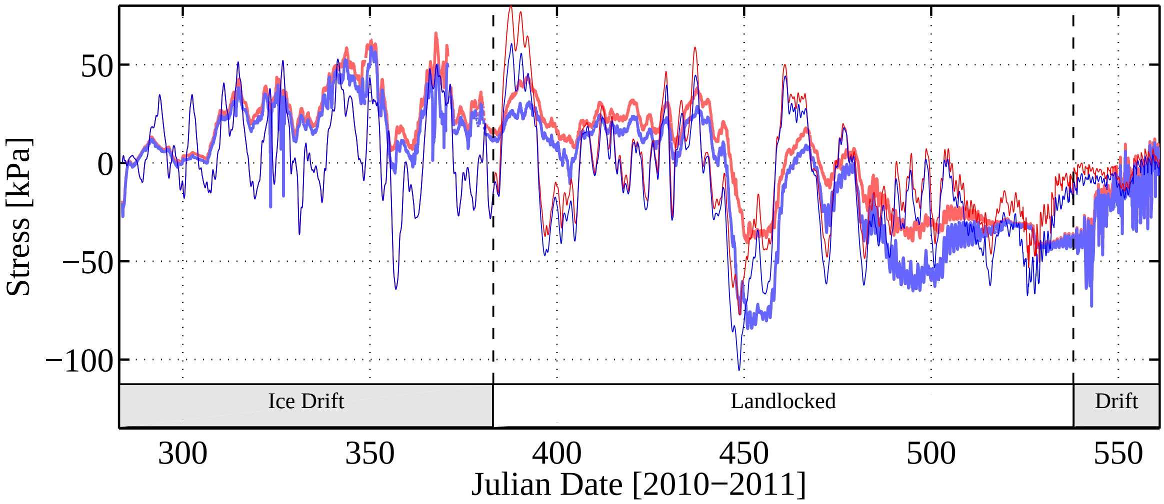

In Figure 3.10, we show the magnitude of the difference between the major and minor principal stresses ($\sigma_2 - \sigma_1$), caused by land confinement. The simulated and observed values are in good general agreement except near the end of the record when the model was still running in anisotropic mode despite the fact that the thermal stresses are again isotropic. We estimate the anchoring force on the sea ice along the coastline by multiplying $\sigma_2 - \sigma_1$ by the thickness of the first-year ice, surrounding the instrumented multi-year ice floe. The first-year ice thickness ranges from 0.74 to 1.54 m, during the period JD 383 - 538 (results not shown). Land confinement results in significant directional differences in stresses of the order of 10 kPa with maximum value of 22.8 kPa (see Figure 3.10). The corresponding ice anchoring force per unit length of coastline is up to 29.6 kNm^{-1}. This value is obtained by multiplying the maximum land confinement stress of 22.8 kPa on JD 455 by the first-year ice thickness, calculated from the 1D thermodynamics model of *Huwald et al.* [2005], of 1.3 m on the same day. These estimates can potentially be used to develop parameterization of grounding forces in coastal region when the ice keel reaches the ocean floor.

Figure 3.10: Simulated (dotted line) and observed (solid line) σ_1-σ_2. In this simulation the Young's Modulus is equal to 0.5 GPa and the relaxation time constant is 8 days.

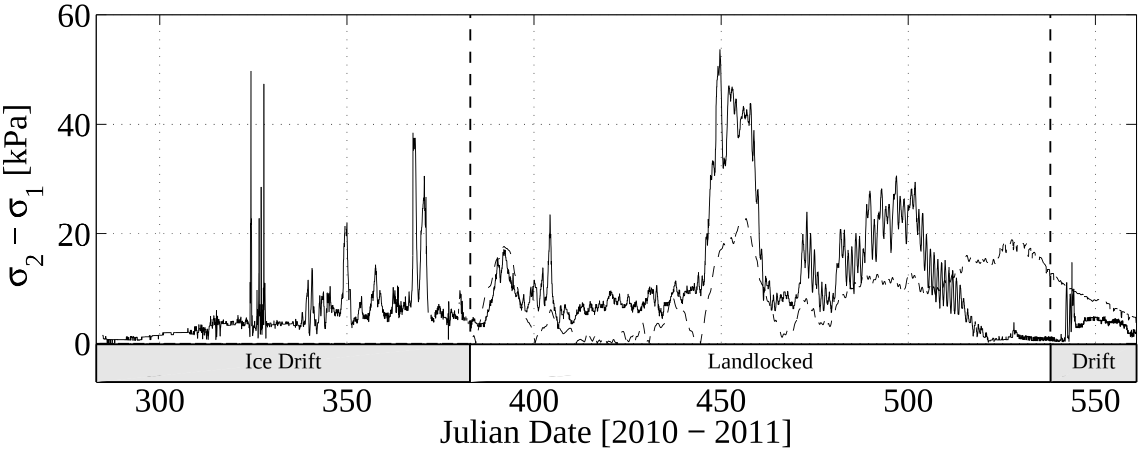

Note that the magnitude of the land confinement force is sensitive to the choice of lateral boundary condition during the landlocked season, i.e. $\epsilon_{22}(t \geq t_{onset}) = \epsilon_{22}(t = t_{onset})$. For instance if we allow some strain to be present in the direction perpendicular to the coastline, the land confinement force could be much smaller. As a result, a larger Young's Modulus would be required to match the observed difference in principal stresses. A larger Young's Modulus, however, would largely exaggerate the seasonal cycle (absolute value of the thermal stresses) in thermal stresses. The fact that the model simulates both the seasonal cycle and the difference in principal stresses suggests that the Dirichlet boundary condition of $\epsilon_{22}(t \geq t_{onset}) = \epsilon_{22}(t = t_{onset})$ is a good approximation.

Figure 3.11: Sensitivity of the Young's Modulus to changes in sensor depth, for a residual compressive stress at the beginning of the melt season $\Delta\sigma$ = -30 kPa on JD 544 and an amplitude of seasonal air temperature change ΔT = -40°C for the isotropic and anisotropic thermal stresses models.

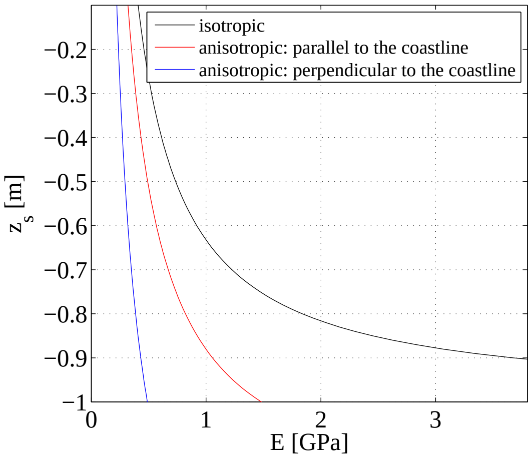

Finally, the error in the E estimate can be calculated by substituting K(z_s = -0.55 ± 5 cm) in equation (3.26). We find that the optimal E value is insensitive to the exact sensor depth location for a wide range of depth around the measured value. The error in E estimates associated with a ± 5 cm error in sensor depth is approximately 10% for the isotropic and anisotropic cases (see Figure 3.11).

3.6 Sensitivity Studies

Given that the rate of change of surface air temperature is a key factor in determining the magnitude of the maximum thermal stress in tension and compression, we perform sensitivity studies with our 1.5D anisotropic thermal stress model, reducing the number of ice and snow layers, and modifying the snow thickness in the 1D thermodynamic model used to force the thermal stress model. We also present results for two additional sensitivity studies taking into account the dependence of the Young's Modulus on sea-ice temperature, and using a viscous creep parameterization that is a function of the stress level and the sea-ice temperature [following *Lewis*, 1993].

In the first experiment, we degrade the vertical resolution in the snow and ice slabs

Table 3.2: Root mean square error (RMSE) between observed and simulated principal stresses with different number of layers in the ice (Ni) and snow (Ns).

Ns	Ni	RMSE (kPa)	
		σ_1	σ_2
10	10	13.0	13.1
4	4	16.4	15.1
3	3	17.0	15.0
1(linear)	3	16.5	13.5
2	2	17.0	14.2
1(linear)	1 (linear)	57.4	60.3

of the 1D thermodynamic model used to force the thermal stress model. This is done in order to find the minimum number of snow/ice layers required to properly simulate the internal ice stresses (error of the order of 15% of the control run value). Note that the stress relaxation time constant and Young's Modulus in this simulation are the same as in the control run presented in Figure 3.8.

For a simulation of the internal sea-ice stresses with two, three, or four layers each of the ice and snow, the root mean square error between the simulated and observed σ_1 and σ_2 increase with degrading vertical resolution. The simulation with two layers each of ice and snow shows errors of 17.0 kPa and 14.2 kPa, an increase of more than 15% when compared with the control run. Finally, for a simulation with one layer of snow and three layers of ice, the root mean square error between the simulated and observed σ_1 and σ_2 does not increase from the error in the control run. We conclude that one layer of snow and three layers of ice is sufficient to properly simulate the internal ice stresses. This is at the low end or smaller than the typical number of layers used in current Global Climate Models participating in the Climate Model Intercomparison Project Phase 5 [*Hunke et al.*, 2013]. A summary of the results from the vertical resolution sensitivity study are summarized in Table 3.2.

In the second experiment, we force the anisotropic thermal stress model with an internal temperature profile simulated by setting the snow cover depth to zero in the 1D thermodynamic model. This is done in order to show the importance of properly simulating the snow depth for the internal thermal stress level. In this simulation, the vertical resolution is the same as in the control run, i.e. ten layers in the ice. The simulated internal sea-ice stresses without snow cover show much larger amplitudes when compared with the observation (Figure 3.12c). The root mean square errors between the simulated and observed stresses are 50.3 kPa and 50.5 kPa, approximately four times larger when compared with the control simulation with snow (see Figure 3.8). When a snow cover is not present, there is no insulating effect and the surface temperature signal transmits faster and deeper within the floe. This shows the importance of a proper simulation of the snow depth over sea ice. For instance, *Lewis et al.* [1994] removed the snow cover from the sea ice in the CAA to induce thermal cracking of the underlying sea ice. This would have an impact on the strength of the pack ice and its dynamics.

In a third set of sensitivity experiments, we consider the dependence of the Young's Modulus on sea-ice temperature [*Cox*, 1984] :

$$E = E_o(1 - 0.012\ T_{ice}), \tag{3.27}$$

where T_{ice} is the ice temperature in °C and E_o is the reference Young's Modulus at $T_{ice} = 0$ °C. In this simulation, we assume $E_o = 0.5$ GPa, the optimal value decided from a comparison between observation and simulated internal stresses (see section 3.5). The results are not sensitive to this parameterization of E as a function of the ice temperature, except between JD 450 and JD 455 when a sudden decrease in surface temperature was recorded (see Figure 3.12b). In this case, the low temperature leads the higher Young's Modulus and higher (in magnitude) thermal stresses in the σ_2 component.

Finally, we consider the viscous creep parameterization of *Lewis* [1993] that depends on stress level, sea-ice temperature, and porosity (see section 3.2 for details). In this parameterization, the strain rate caused by viscous creep is larger at higher stress level and higher temperature. In winter, the sea ice is under higher stress level and lower temperature. The effect of both stress level and temperature are in opposition and the net effect is small. Thus, the seasonal dependence of viscous creep is small. The viscous creep term is very sensitive to the exact choice of n and Q parameters (see equation 3.15). In this simulation, we use $Q = 1.06 \times 10^5$ [Joules/mole], as suggested by *Lewis* [1993], and $n = 2.75$ [unitless] (n = 3.26 in *Lewis* [1993]) in order to minimize the difference between the observed and simulated stress relaxation after the ice melt onset (see also Section 3.5 and figure 3.5). The results of this sensitivity study show better agreement during the earlier drift season with higher thermal stresses. However, RMSEs are larger during the warming phase of the landlocked season (Figure 3.12c : JD 480 - 550) as the viscous creep increases with temperature increase.

3.7 Summary and Conclusions

We built on the 1D thermal stress model of *Bogorodsky et al.* [1972] and present a 1.5D thermal stress model to simulate landlocked sea ice in a channel of the Canadian Arctic Archipelago (CAA). The model takes into account the effect of viscous creep relaxation and the effect of land confinement on the internal sea-ice stresses. This is done by keeping the total deformation perpendicular to the coastline constant and equal to its value at the onset of the landlocked ice in the simulation during the landlocked ice regime. This change in boundary condition represents the effect of ice grounding on the ocean floor at the coastline. In this model, we assume that the model domain is infinite in the direction parallel to the long axis of the channel, and that the ice is free to contract and expand in that same direction. The model is validated against in-situ internal stress measurements from an Ice Stress Buoy deployed on a multi-year floe, on 10 October 2010, in the Viscount Melville Sound of the CAA (74°N , 110°W). The ice thickness at the buoy location is 1.87 m. The observations are described in details in a companion paper published in the same issue.

We first estimate the value of the viscous creep relaxation time constant from the observed relaxation of the residual compressive stress at the onset of the melt

Figure 3.12: Observed (σ_1: bold red, σ_2: bold blue) and simulated (σ_1: thin red, σ_2: thin blue) principal stresses at the sensor depth (-0.55 m) from the anisotropic thermal stress model with (a) no snow cover, (b) ice temperature dependent Young's Modulus ($E = E_o(1 - 0.012T_{ice})$, where $E_o = 0.5GPa$), and (c) with ice temperature dependent Young's Modulus and the viscous creep term of *Lewis* [1993]. Other physical constants, and vertical resolution of the model are the same as in the control run.

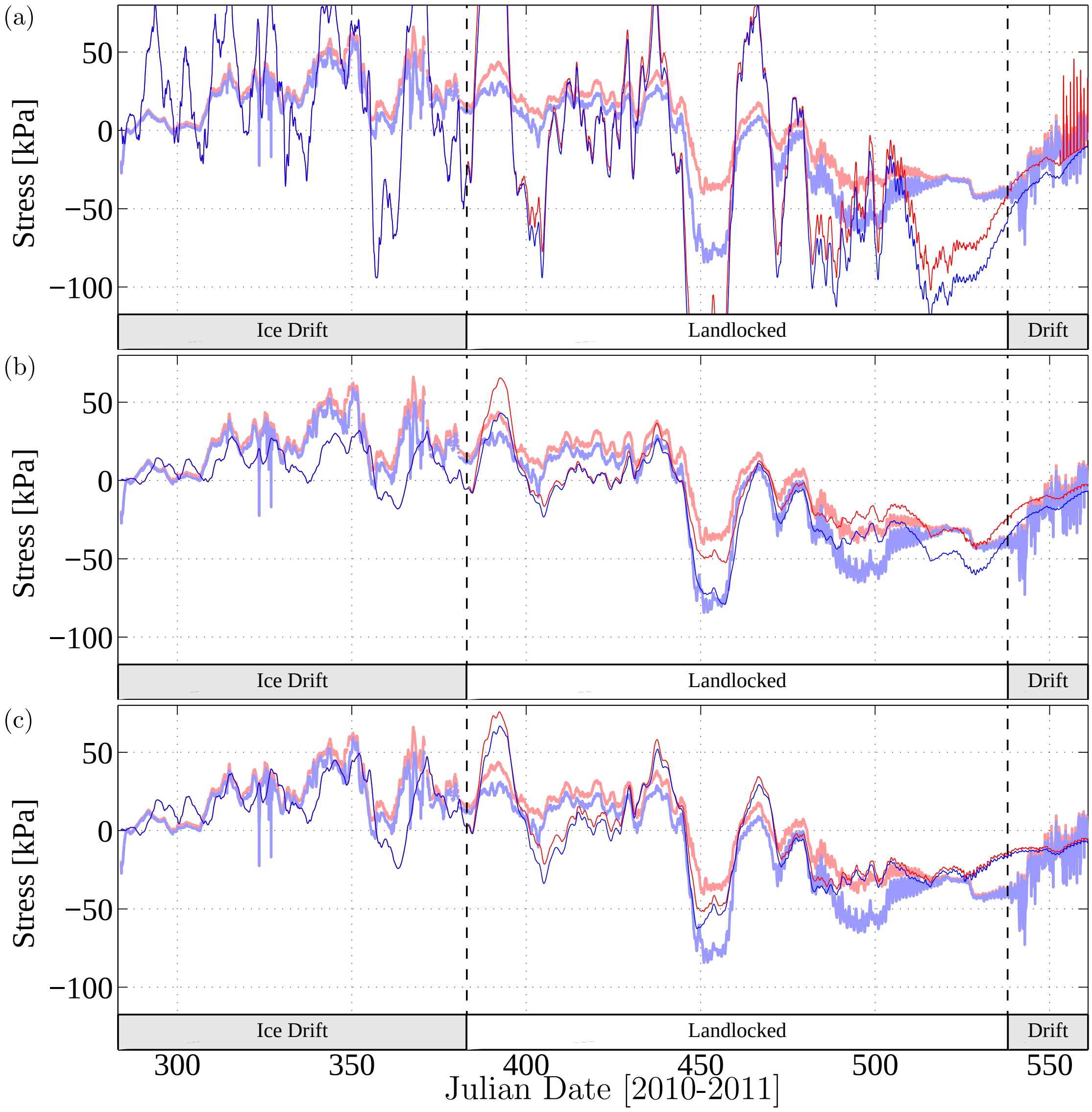

season. The observed decay of the thermal stresses during this time period shows a clear exponential decay with a time constant of approximately 8 days. This is three days longer than the longest relaxation time constant published in the literature [e.g. *Sukhorukov*, 1996].

We also present a simpler thermal stress model forced with a linear internal snow and sea-ice temperature profile assuming that the thermal inertia of ice is negligible. This assumption is valid for seasonal changes in surface air temperature, and allows us to calculate an analytical solution of the internal thermal stresses to study the sensitivity of the model to changes in sea-ice stiffness (Young's Modulus). Results show that a Young's Modulus E = 0.3 - 0.5 GPa gives the best match between the simulated and observed internal thermal sea-ice stresses for using this simpler model.

Results from the thermal stress model, forced with hourly varying surface air temperature and a non-linear internal ice temperature profile from the 1D multi-layer sigma-coordinate thermodynamic model of *Huwald et al.* [2005], show that the optimal Young's Modulus is equal to 0.5 GPa, confirming the results from the simpler linear model. This is in the lower range of observed Young's Modulus published in the literature (0.3 - 10 GPa) [e.g. *Ji et al.*, 2011; *Timco and Weeks*, 2010; *Weeks and Assur*, 1967]. The root mean square errors between simulated, using the optimal Young's Modulus and viscous creep relaxation time constant, and measured σ_1 and σ_2 are 13.0 kPa and 13.1 kPa, respectively. The difference in the principal stresses, a measure of the land confinement effect, is of the order of 10 kPa with maximum magnitude 22.8 kPa. This is significant when compared with the mean observed thermal stresses. An estimate of the maximum grounding force by ice anchor on ocean floor of 29.6 kNm^{-1} can be derived by multiplying the maximum $\sigma_2 - \sigma_1$ (22.8 kPa on JD 455) by the thickness of the first-year ice (1.3 m on the same day) surrounding the multi-year ice floe.

A sensitivity study of the model to the details of the internal temperature profile used to force the model is then presented. The vertical resolution in the snow and ice was decreased in order to find the minimum number of snow and ice layers required for the 1.5D thermal stress model to simulate internal thermal stresses with acceptable error increase (<15%). Results show that at least one layer in snow and three layers in ice must be used in order to have errors that are as small as the control run values. This is not incompatible with current vertical resolutions of sea ice and snow in thermodynamic models used in the Global Climate and regional modeling communities. In the second experiment, the snow cover was removed, to show the importance of properly simulating the snow depth on the internal thermal stress level. In this experiment, the root mean square error in the major (minor) principal stress increases from 13.0 (13.1) kPa to 50.3 (50.5) kPa. Together, these sensitivity studies highlight the importance of properly simulating the internal temperature profile to force the thermal stress model.

An additional sensitivity study of the model to the effect of a temperature dependent Young's Modulus as suggested by *Cox* [1984] is presented. Results show that considering a temperature dependent Young's Modulus leads to higher magnitude stresses only when the surface temperature changes rapidly associated with synoptic scales. Otherwise, the model is not sensitive to the parameterization of Young's Modulus. Finally, the sensitivity of the results to the parameterization of stress relaxation [*Lewis*, 1993], which depends on stress level, ice temperature, and porosity, is presented (keeping the temperature dependent Young's Modulus). In this case, results show that anisotropy in the stresses becomes smaller and the RMSEs increase during the landlocked season. No other combination of model free parameters could reduce this error. This suggests that more studies of the sea-ice viscous behaviour are required for more precise modeling of the thermal stresses of sea ice.

3.8 Appendix: 1D and 1.5D thermal stress model forced with a linear temperature profile

In the following, we derive the analytical solution of the thermal stress model forced with a linear internal temperature profile and a sinusoidal surface air temperature perturbation (e.g. diurnal, synoptic seasonal scales). We first consider equation (3.11) and (3.13) for isotropic materials,

$$\frac{\partial \sigma^{tot}}{\partial t} = \frac{E}{1-\nu}\frac{\partial}{\partial t}\left(\frac{\int_b^{s_i} E\alpha\Delta\theta dz}{\int_b^{s_i} Edz} - \alpha\Delta\theta\right) - \frac{1}{\tau}\sigma^{tot}. \tag{3.28}$$

For constant E and α (i.e. independent of depth z), equation (3.28) can be written as:

$$\frac{\partial \sigma^{tot}}{\partial t} = \frac{E}{1-\nu}\alpha\frac{\partial}{\partial t}\left(\frac{\int_b^{s_i} \Delta\theta dz}{\int_b^{s_i} dz} - \Delta\theta\right) - \frac{1}{\tau}\sigma^{tot}. \tag{3.29}$$

We assume a linear temperature profile within the snow and ice with the following boundary conditions: $\theta = 0°\text{C}$ at the ice base ($z = b$), $\theta = \theta_s(t)$ at the snow surface ($z = s_s$), and $k_s\frac{dT_s}{dz} = k_i\frac{dT_i}{dz}$ at the ice-snow interface($z = s_i$) (i.e. continuity of conductive heat flux at the snow-ice interface), where k_s and k_i are the snow and ice thermal conductivities, and T_s and T_i are the internal snow and ice temperature. The internal ice temperature can then be written as:

$$\theta(z,t) \quad = \quad \left(1 - \frac{s_i - z}{s_i - b}\right)\left(\frac{1}{1 + \frac{k_i(s_s - s_i)}{k_s(s_i - b)}}\right)\theta_s(t), \tag{3.30}$$

where $\theta_s(z,t) = \Delta T sin(\omega t)$, ΔT is the amplitude of seasonal cycle in temperature, ω ($= \pi/\mathfrak{T}$) is the frequency, and $\mathfrak{T}$ is the length of the winter season. Substituting equation (3.30) into equation (3.29), and assuming that changes in ice thickness ($\frac{d(s_i-b)}{dt}$) are small compared to changes in internal temperature we write:

$$\frac{\partial \sigma^{tot}}{\partial t} = EK\frac{\partial \theta_s(t)}{\partial t} - \frac{1}{\tau}\sigma^{tot} = EK\ \Delta T\ \omega cos(\omega t) - \frac{1}{\tau}\sigma^{tot}, \tag{3.31}$$

where

$$K = \begin{cases} -\dfrac{\alpha}{1-\nu^2} \dfrac{1}{1+k_i h_s/k_s h_i} \left(\dfrac{1}{2} + \dfrac{z}{h_i} + \nu\left(1 + \dfrac{z}{h_i}\right)\right), & \text{direction parallel to the coastline,} \\ -\dfrac{\alpha}{1-\nu^2} \dfrac{1}{1+k_i h_s/k_s h_i} \left(1 + \dfrac{z}{h_i} + \nu\left(\dfrac{1}{2} + \dfrac{z}{h_i}\right)\right), & \text{direction perpendicular to the coastline,} \\ -\dfrac{\alpha}{1-\nu} \dfrac{1}{1+k_i h_s/k_s h_i} \left(\dfrac{1}{2} + \dfrac{z}{h_i}\right), & \text{isotropic,} \end{cases}$$

h_i is the ice thickness $(s_i - b)$, and h_s is the snow depth $(s_s - s_i)$. Note that the term in $\frac{d(s_i-b)}{dt}$ in equation (3.29) is smaller than the other term but not negligible. We still neglect it for simplicity.

The solution of the homogeneous (complementary) part of equation (3.31) is

$$\sigma_h = Ae^{-\frac{t}{\tau}}, \tag{3.32}$$

where A is an arbitrary constant. The particular solution of (3.31) has the form:

$$\sigma_p = Bcos(\omega t) + Csin(\omega t). \tag{3.33}$$

Substitute σ_p into equation (3.31), we find

$$B = \frac{K\omega\frac{1}{\tau}}{\omega^2 + (\frac{1}{\tau})^2} E\Delta T, C = \frac{K\omega^2}{\omega^2 + (\frac{1}{\tau})^2} E\Delta T. \tag{3.34}$$

The general solution of equation (3.31) is therefore,

$$\sigma^{tot} = Ae^{-\frac{t}{\tau}} + \frac{K\omega}{\omega^2 + (\frac{1}{\tau})^2} E\Delta T \left[kcos(\omega t) + \omega sin(\omega t)\right]. \tag{3.35}$$

Considering the following initial condition $(\sigma(t = 0) = 0)$, we obtain

$$A = -\frac{K\omega\frac{1}{\tau}}{\omega^2 + (\frac{1}{\tau})^2} E\Delta T. \tag{3.36}$$

The final solution for the stresses as a function of the relaxation time constant can be written as (with some reordering):

$$\sigma^{tot}(t) = KE\frac{(\omega\tau)}{(\omega\tau)^2+1}\Delta T\left[cos(\omega t)+\omega\tau sin(\omega t)-e^{-\frac{t}{\tau}}\right]. \tag{3.37}$$

In the limit when $\omega\tau \ll 1$, equation (3.37) becomes

$$\sigma^{tot}(t) = KE\,(\omega\tau)\,\Delta T\left[cos(\omega t)-e^{-\frac{t}{\tau}}\right]. \tag{3.38}$$

Equation (3.38) implies that stress becomes zero in the limit when the viscous creep relaxation time constant is short when compared with the time constant of the temperature perturbation.

In the limit when $\omega\tau \gg 1$, equation (3.37) becomes

$$\sigma^{tot}(t) = KE\Delta T sin(\omega t) = KE\theta_s. \tag{3.39}$$

Equation (3.39) implies that stress is proportional to θ_s, when the viscous creep relaxation time constant tends toward infinity (no creep relaxation).

Chapter 4

Estimating geophysical sea-ice strength of landlocked sea ice from in-situ observations in the Canadian Arctic Archipelago

In this chapter, we estimate the sea-ice geophysical compressive strength (P^*) from the critical loads acting on sea ice during the time around the landlock onset in M'Clintock Channel in the Canadian Arctic Archipelago (CAA). Around the time of landlock onset, the sea ice, as simulated by a viscous plastic sea-ice model, transitions back and forth between its viscous and plastic states. Observed sea-ice drift from three buoys deployed in M'Clintock Channel in the CAA are used to derive an observation-based estimate of the sea-ice mechanical properties. This paper will be submitted for publication to the Journal of Geophysical Research, Ocean this Winter.

Estimating geophysical sea-ice strength of landlocked sea ice from in-situ observations in the Canadian Arctic Archipelago

Y. Hata [1], L. B. Tremblay [1] and F. Dupont [2]

[1] Department of Atmospheric and Oceanic Science, 805 Sherbrooke Street West,

McGill University, Montreal, Quebec, Canada. H3A 0B9

[2]Canadian Meteorological Centre, Environment and Climate Change Canada,

Dorval, Quebec, Canada

Abstract

The geophysical scale sea-ice compressive and shear strength parameter is not well constrained by observation; yet it is crucial to simulate the timing of landlock ice onset and breakup. We estimate P^* by calculating the loads (i.e. surface air-ice and basal ice-ocean stresses) during the time it transits from mobile to landlock sea ice. If the surface stresses acting on the ice induce motion, we know that the internal strength of sea ice was exceeded. This provides an upper bound on the mechanical strength. If the surface stresses acting on the ice are not large enough to induce motion, we know that the internal strength of sea ice was not exceeded. This provides a lower bound on the mechanical strength. We test this idea using output diagnostic from the Regional Ice Operation Prediction System (RIOPS). Results from this "proof of concept" give an estimate of P^* equal to 22 ± 7.8 kN/m^2, in accord with the known value used in the model. We then estimate P^* from sea-ice drift data from buoys deployed in the Canadian Arctic Archipelago (M'Clintock Channel) in 2008, 2009 and 2013, together with surface forcing from reanalysis surface stress and RIOPS basal stress data. Results from this analysis suggest a value of P^* equal to 94.4 ± 8.8 kN/m^2 (more than three times the value used in current sea-ice model) for one drifter deployed in 2013 when the sea ice in the M'Clintock Channel was mainly composed of first-year ice. The method, however, fails to give a meaningful estimate in other years when some multi-year ice was still present at the end of the previous summer melt period. We hypothesize that this is due to uncertainties in the effective ice thickness of the pack ice when a mixture of multi-year and first-year ice is present, large uncertainties in ice-ocean surface stress associated with large spatial gradients in ice-ocean surface stress associated with tidal current and we cannot rule out the possibility of large error in the surface air-ice surface stresses in the Canadian Meteorological Center's Global Deterministic Prediction System Reforecast (CGRF) used to to make the estimate. Further analysis to understand and quantify those uncertainties are left for future work.

4.1 Introduction

Landfast sea ice is defined as sea ice that is immobile for a specified time interval, and extends from a coastline or a region of grounded sea ice [*Barry et al.*, 1979]. Landfast ice covers 1.8 × 10^6 km^2 (∼20 %) of the Arctic Ocean and has an average annual duration of more than seven months [*Yu et al.*, 2014]. It is important for local Inuit communities who use landfast ice as hunting and fishing platforms [*George et al.*, 2004], for local ecosystem by altering pattern of migration and nutritional status for fish and marine mammals [e.g. *Tynan and DeMaster*, 1997; *Macdonald et al.*, 1995], for high-latitude climate by moving the location of deep water formation further offshore at the edge of the continental shelf [*Itkin et al.*, 2015], and moving the location of ice edge to a higher latitude at the end of the melt season [*Reimnitz et al.*, 1994]. In the East Siberian, Laptev, and Kara seas, the landfast sea ice extends northward as far as 500 km from the coasts despite offshore wind [*Reimnitz et al.*, 1994]. This broad extent is due to tensile strength of sea ice, the presence of offshore islands and associated ice arches [*König Beatty and Holland*, 2010], and grounding of sea ice in shallow waters [*Selyuzhenok et al.*, 2015; *Lemieux et al.*, 2015; *Haas et al.*, 2005]. Along the Alaskan coast, the landfast sea-ice extent is much smaller, around 50-km wide [*Barry et al.*, 1979]; this narrow band of landfast sea ice is stable due to ice anchoring on the ocean floor at its outer edge along the ∼20-m isobaths (the stamukhi zone) [*Mahoney et al.*, 2007]. In the Canadian Arctic Archipelago (CAA), the sea ice is landlocked (i.e. attached to shore on all sides) and is stable mainly because of its compressive strength [*Melling*, 2002].

Olason [2016] successfully simulated landfast sea ice in the Kara Sea using a viscous plastic sea-ice model with a truncated Coulombic yield curve, a maximum bulk viscosity 10^5 times larger than the value commonly used in the community, and a sea-ice compressive strength parameter (P^*) ranging between 36 and 52 kN/m^2 — again larger than the P^* value commonly used in the community [27 kN/m^2: *Hibler*, 1979; *Hunke and Dukowicz*, 1997]. These P^* values are in accord with estimates from satellite derived sea-ice drift and surface wind stress derived from reanalysis data [*Tremblay and Hakakian*, 2006]. On the other hand, comparisons between simulated and observed sea-ice thickness and probability density function (PDF) of sea-ice deformation suggest that a smaller P^* should be used in the context of a standard viscous-plastic sea-ice rheology [*Bouchat and Tremblay*, 2017; *Miller et al.*, 2005]. This highlights the uncertainties on the exact value of the geophysical scale sea-ice strength parameter that should be used at those spatial resolution ($\sim$ 10 km) in current sea-ice models.

The CAA, also called the North American Polar Continental Shelf, consists of many small islands. The multi-year sea ice from the Arctic Ocean flows into the CAA via the strait of the Queen Elizabeth Islands in the north (between Prince Patrick Island and Axel Heiberg), migrates south in the Viscount Melville Sound and M'Clintock Channel and flows out of the CAA through the M'Clure Strait in the Fall (in the case of Viscount Melville Sound) or melts locally (in the case of M'Clintock Channel) [*Howell et al.*, 2013]. First-year ice forms between multi-year ice floes or over open ocean (Victoria Strait or the eastern CAA south of Parry Channel), and can be promoted to multi-year ice mainly in the north and west or melt in the following summer [*Stephen E. L. et al.*, 2008].

The CAA is covered by landlocked sea ice for an average of nine months each year and an average maximum extent of 538 $\times$ 10^3 km^2 [*Yu et al.*, 2014]. Landlocked sea ice in the CAA can be simulated using current sea-ice dynamics models in Global Climate Models, since the intricate topography results in small wind and ocean fetches, thus, the compressive and shear strengths of sea ice is sufficient to maintain a stable landlocked sea-ice cover [*Sou and Flato*, 2009]. However, the timing of landlock onsets and breakups is not yet well simulated [*Lemieux et al.*, 2015].

The focus of this study is to provide better constrains on the sea-ice mechanical properties using observed landlock onset and breakup dates. To this end, we first present a proof of concept of the method using diagnostics (sea-ice drift and concentration, surface wind stress, and water drag) from the Regional Ice Operational Prediction System (RIOPS) from Environment and Climate Change Canada (ECCC).

We then apply the same method to observed sea-ice drift from the three drifting buoys deployed in the CAA in 2007, 2009, and 2013. The method, originally proposed by *Pritchard* [1976] and later used by *Tremblay and Hakakian* [2006], is based on estimates of the critical loads acting on sea ice of a known thickness during the time it transits from mobile to landlock season.

The manuscript is organized as follows. In Section 4.2, we describe the buoy data, the ice/ocean diagnostics from RIOPS, the atmospheric field from the Canadian Meteorological Centre's (CMC) Global deterministic prediction system ReForecasts (CGRF), and a 1D sigma-coordinate thermodynamic sea-ice model. In Section 4.3, we describe the method used to estimate the sea-ice compressive strength. The proof of concept using RIOPS diagnostics is presented in Section 4.4.1. In Section 4.4.2 and 4.5, results and discussions from the buoy data analysis are presented. Section 4.6 summarizes the main conclusions from this study and proposed avenues for future work.

4.2 Data

4.2.1 Surface Velocity Profiler (SVP)

This study is based on data from Surface Velocity Profilers (SVP). SVPs are manufactured by MetOcean. It consists of a 40-cm diameter sphere and measures the position of sea ice (at 30-minute or 3-hour interval, depending on the buoy model, see Table 4.1) using a Global Positioning System (GPS) with an accuracy of 10 m and surface air temperature with an accuracy of 0.01 °C. The data are transmitted through Iridium satellite using an Iridium 9602 short burst data transceiver.

In this study, we use data from three SVPs deployed in the CAA in 2007, 2009, and 2013 (see Table 4.1). All three buoys drifted into M'Clintock Channel after the deployments. The two buoys deployed in 2007 and 2009 (referred to as MC07 and MC09, hereafter) were deployed in fall on multi-year ice floes using the logistics of the

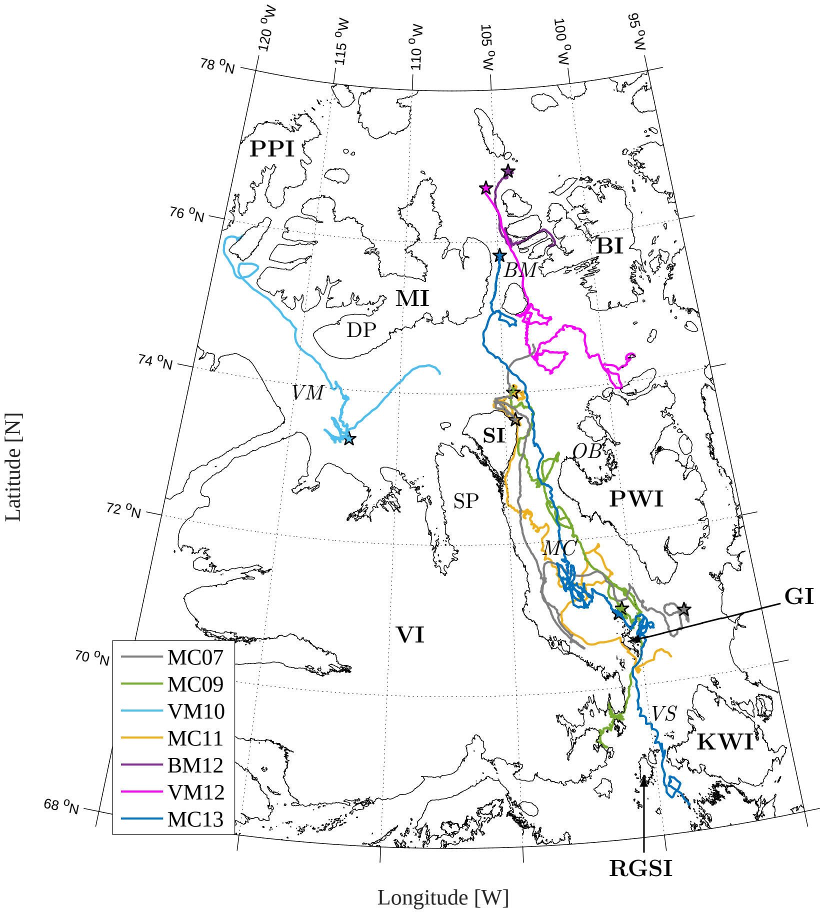

Figure 4.1: Trajectories of the Surface Velocity Profilers (SVP) observed in the CAA. Stars (⋆) indicate the buoy position during landlock seasons. The following is the acronyms of abbreviations in the figure. BI: Bathurst Island, BM: Byam Martin Channel, DP: Dundas Peninsula, GI: Gateshead Island, KWI: King William Island, MC: M'Clintock Channel, MI: Melville Island, OB: Ommanney Bay PPI: Prince Patrick Island, PWI: Prince of Wales Island, RGSI: Royal Geographical Society Island, SI: Stefansson Island, SP: Storkerson Peninsula, VI: Victoria Island, VM: Viscount Melville Sound, VS: Victoria Strait.

Amundsen icebreaker as part of the ArcticNet program between Byam Martin Island and Stefansson Island. The buoy deployed in 2013 (referred to as MC13, hereafter) was deployed in early spring on first-year landlock ice using the logistic (Twin Otter) of the Polar Continental Shelf Program in the south Byam Martin Channel (Figure 4.1 and Table 4.1). MC07 and MC09 transmit data every three hours; MC13 transmits data every 30 minutes.

Table 4.1: Data summary of SVPs deployed in the Canadian Arctic Archipelago between 2007 and 2013: buoy identification name; sampling frequency (hour); deployment date and location; and date and location of buoy death. The names of each buoys are related with the year of deployment and the main drift location.

SVP Name	Sampling Frequency [hour]	Start location	Start date	End location	End date
MC07	3.0	74.63°N 103.44°W	9 Oct 2007	70.91°N 98.09°W	11 Jul 2009
MC09	3.0	74.06°N 104.59°W	7 Aug 2009	69.32°N 102.07°W	22 Oct 2009
VM10	3.0	74.26°N 108.08°W	10 Oct 2011	75.84°N 118.85°W	3 Sep 2008
MC11	0.5	74.00°N 104.56°W	10 Apr 2011	70.32°N 98.84°W	7 Oct 2011
BM12	0.5	76.92°N 104.20°W	30 Apr 2012	75.90°N 102.25°W	12 Aug 2012
VM12	0.5	76.71°N 105.53°W	30 Apr 2012	74.72°N 94.97°W	2 May 2013
MC13	0.5	75.81°N 104.49°W	7 May 2013	68.36°N 98.99°W	11 Aug 2015

4.2.2 The Regional Ice-Ocean Prediction System (RIOPS)

Data from RIOPS are used for a proof of concept of the method developed to determine the geophysical mechanical strength properties of sea ice in the CAA. The RIOPS is a system composed of a sea-ice model with a mixed-layer ocean model that resolves tides. The model domain includes the Arctic Ocean, the North Atlantic, and the CAA [for details see *Lemieux et al.*, 2016]. Lateral boundaries in the North Atlantic (∼ 25°N) and the Bering Strait (∼ 65°N) are closed. The spatial resolution ranges from two to three km in the CAA. RIOPS produces four times 48-hr forecast everyday, and is initialized at 00z everyday with the 24-hour run from the previous restart which is nudged to the analysis of the Global Ice Ocean Prediction System [GIOPS, *Smith et al.*, 2016] — a system that includes a high-resolution (1/4°) global coupled ice-ocean model and assimilation of ice concentration field using the three dimensional variation (3DVAR) approach. The system is forced with the combined atmospheric field from the Regional (10 km spatial resolution) and Global (25 km resolution) Deterministic

Prediction System (RGDPS), because the RIOPS domain is slightly larger than the domain of Regional Deterministic Prediction System (RDPS). The analyses presented in this study are based on 15 months of RIOPS simulation from October 2014 to December 2015.

4.2.3 The Canadian Meteorological Centre's (CMC) Global deterministic prediction system ReForecasts (CGRF)

The Canadian Meteorological Centre's Global deterministic prediction system reforecast [*Smith et al.*, 2013] is a reforecast dataset simulated with the Global Deterministic Prediction System (GDPS) based on the Global Environmental Multiscale (GEM) atmospheric model [*Côté et al.*, 1998a; *Côté et al.*, 1998b]. The spatial resolution of the atmospheric fields is 0.45° and 0.3° in longitude and latitude before 14 February 2011, and 0.35° and 0.225° in longitude and latitude after. This is comparable to other standard global reanalysis, such as MERRA (0.5° × 0.625°), NCEP-DOE Reanalysis 2 (2.0° × 1.75°), and ERA-Interim (∼0.7° × ∼0.7°). To produce the CGRF dataset, the GDPS is run daily for 30-hour reforecast. The first 6-hour forecasts are used for spin up of the dynamics and hydrological cycle. In the following, we calculate the surface air-ice drag from CGRF wind velocity and we use CGRF atmospheric fields for the forcing of a 1D sigma-coordinate thermodynamic sea-ice model [*Huwald et al.*, 2005] to calculate the sea-ice thickness of first-year ice in the CAA.

4.2.4 The Canadian Ice Service (CIS) gridded sea-ice concentration

The sea-ice concentration in gridded format, which has a resolution of 0.25°, is compiled from the weekly regional ice charts of Canadian Ice Service (CIS) that ice categories is in Egg Code. The data include total sea-ice concentrations, and concentrations of multi-year ice, first-year ice, young ice, new ice, and icebergs. The data are available weekly since 1960. The ice charts, from which the gridded dataset is derived, are based on remotely sensed information, surface observations, airborne and ship reports, operational model results, and nowcast. We use the sea-ice concentration data in M'Clintock Channel to study the influence of multi-year ice concentration on the timing of landlock onset.

4.2.5 1D sigma-coordinate thermodynamic sea-ice model

The sea-ice thickness of first-year ice used to estimate sea-ice mechanical strength from ice velocity observed with SVP is calculated using a 1D sigma-coordinate thermodynamic sea-ice model [*Huwald et al.*, 2005]. In this model, the advections of mass and energy, which are associated with relayering when sea ice grows and melts, occurs naturally using a sigma-coordinate transformation for the ice and the snow. The model also includes penetration of shortwave radiation and a brine pocket parameterization [*Bitz and Lipscomb*, 1999]. The model was validated against observations from the Surface Heat Budget of the Arctic Ocean (SHEBA) experiment [*Uttal et al.*, 2002] with maximum error equal to 5 cm (2.5%) in the ice thickness when forced with observed atmospheric radiative and turbulent fluxes and solid precipitation rates. In the following, we use the sea-ice thickness simulated with this model forced with CGRF atmospheric data of the same years as the buoy observations.

4.3 Methodology

The 2D momentum equation of sea ice is written as:

$$\rho_i h_i \frac{d\boldsymbol{u_i}}{dt} = -\rho_i h_i f \boldsymbol{k} \times \mathbf{u_i} + \boldsymbol{\tau_a} + \boldsymbol{\tau_w} - \rho_i h_i g \nabla \boldsymbol{H} + \nabla \cdot \boldsymbol{\sigma}, \tag{4.1}$$

where ρ_i, h_i, $\boldsymbol{u_i}$ are the density, thickness, and velocity of sea ice, f is the Coriolis parameter, $\boldsymbol{k}$ is a unit vector normal to the ice surface, $\boldsymbol{\tau_a}$ and $\boldsymbol{\tau_w}$ are the air and water drags, g is the gravitational acceleration, $\boldsymbol{H}$ is the sea surface height, and $\boldsymbol{\sigma}$ (σ_{ij}) is the internal ice stress (normal or shear) acting on a plane perpendicular to the

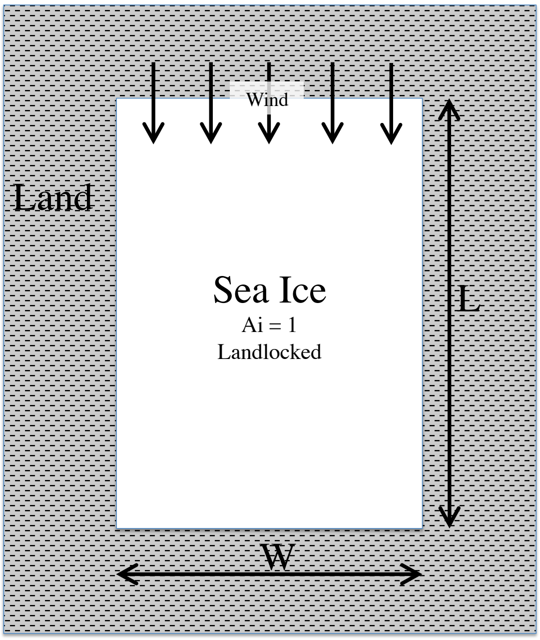

Figure 4.2: Idealized channel of width W and length L. The channel is covered with landlock ice of thickness h_i and concentration $A = 1$. The wind is blowing parallel to the long axis of the channel.

i axis and in the j direction.

For the case of a rectangular domain fully covered with sea ice (sea-ice concentration $A_i \sim 1$) when wind blows parallel to the long axis of a channel (see Figure 4.2), we can write the force balance in the direction of the wind as:

$$\tau LW = 2\sigma_s L + \sigma_n W, \tag{4.2}$$

or

$$\tau L = 2\sigma_s \frac{L}{W} + \sigma_n, \tag{4.3}$$

where τ is the sum of the air (τ_a) and water (τ_w) drag, σ_s is the shear stress at the coasts parallel to the long axis, σ_n is the normal stress at the downwind coast, L is the length of the channel, and W is the width of the channel. In the above, we have assumed that the sea-ice tensile strength is small or that the ice has failed in tension on the upwind wall and the internal ice stress is zero.

When the sea ice is in the plastic regime, equation (4.3) becomes:

$$\tau L \geq 2S\frac{L}{W} + P, \tag{4.4}$$

where S and P are the sea-ice shear and compressive strengths, respectively. The inequality sign comes from the fact that the acceleration term is omitted from equation (4.3). Assuming an elliptical yield curve with aspect ratio ($e = \frac{P}{2S}$) and $A_i = 1$, we write [*Hibler*, 1979]:

$$\tau\, L \geq \frac{P^*}{e} h_i \frac{L}{W} + P^* h_i = P^*\ h_i \left[\frac{1}{e}\ \frac{L}{W} + 1\right], \tag{4.5}$$

where

$$P = P^* h_i, \tag{4.6}$$

$$S = S^* h_i = \frac{P^*}{2e} h_i, \tag{4.7}$$

and h_i is the mean sea-ice thickness. Rearranging terms we get,

$$P^* \leq \tau\, L \left\{ h_i \left[\frac{1}{e}\ \frac{L}{W} + 1\right]\right\}^{-1}. \tag{4.8}$$

When the loads acting on the sea ice are not strong enough to produce deformations (i.e. when the sea ice is in the viscous regime), equation (4.4) can be written as:

$$\tau\, L < 2S\frac{L}{W} + P, \tag{4.9}$$

or

$$P^* > \tau\, L \left\{ h_i \left[\frac{1}{e}\ \frac{L}{W} + 1\right]\right\}^{-1}. \tag{4.10}$$

In equations (4.8) and (4.10), the surface stress terms ($\tau = \tau_a + \tau_w$) can be written using standard bulk formulations [e.g. *McPhee*, 1975] as:

$$\tau_a = C_{da}\rho_a |U_a|^2, \tag{4.11}$$

$$\tau_w = C_{dw}\rho_w |U_w - U_i|^2, \tag{4.12}$$

where C_{da} and C_{dw} are the air-ice and ocean-ice drag coefficients, ρ_a and ρ_w are air and ocean water densities, and $|U_a|$ and $|U_w - U_i|$ are the surface wind and basal ocean current speeds relative to sea ice. Note that we neglect the sea-ice velocity in front of the wind speed and the wind and ocean turning angles are neglected. Substituting equations (4.11) and (4.12) into equations (4.8) and (4.10), we obtain:

$$P^* \begin{cases} \leq \left[C_{da}\rho_a|U_a|^2 + C_{dw}\rho_w|U_w - U_i|^2\right] L \left\{h_i \left[\frac{1}{e}\,\frac{L}{W} + 1\right]\right\}^{-1}, & \text{plastic regime,} \\ > \left[C_{da}\rho_a|U_a|^2 + C_{dw}\rho_w|U_w - U_i|^2\right] L \left\{h_i \left[\frac{1}{e}\,\frac{L}{W} + 1\right]\right\}^{-1}, & \text{viscous regime.} \end{cases} \tag{4.13}$$

In order to determine the sensitivity of the method to the choice of the five free parameters L, W, e, C_{da}, and C_{dw}, we take the derivatives of equation (4.8) with respect to each four parameters:

$$\frac{\partial P^*}{\partial L} = \frac{\tau\,(W\,e)^2}{h_i\,(L + W\,e)^2}, \tag{4.14}$$

$$\frac{\partial P^*}{\partial W} = \frac{\tau\,L^2\,e}{h_i\,(L + W\,e)^2}, \tag{4.15}$$

$$\frac{\partial P^*}{\partial e} = \frac{\tau\,L^2\,W}{h_i\,(L + W\,e)^2}, \tag{4.16}$$

$$\frac{\partial P^*}{\partial C_{da}} = \rho_a|U_a|^2 \frac{eLW}{h_i\,(L + W\,e)}. \tag{4.17}$$

$$\frac{\partial P^*}{\partial C_{dw}} = \rho_w|U_w - U_i|^2 \frac{eLW}{h_i\,(L + W\,e)}. \tag{4.18}$$

For typical values of $\tau \sim 10^{-1}$, $L \sim 500$ km, $W \sim 100$ km, $h_i \sim 2$ m, $e \sim 2$, $C_{da} \sim 3.5 \times 10^{-3}$,$C_{dw} \sim 5.5 \times 10^{-3}$, $U_a \sim 5$ m/s, $U_i \sim 0.05$ m/s, $\rho_a \sim 1.2$ kg/m^3, and $\rho_w \sim 1030$ kg/m^3, the sensitivities of P^* are equal to:

$$\frac{\partial P^*}{\partial L} \sim 2.5 \times 10^{-2}[N/m^3] \tag{4.19}$$

$$\frac{\partial P^*}{\partial W} \sim 0.8[N/m^3] \tag{4.20}$$

$$\frac{\partial P^*}{\partial e} \sim 2 \times 10^{4}[N/m^2] \tag{4.21}$$

$$\frac{\partial P^*}{\partial C_{da}} \sim 2 \times 10^{6}[N/m^2] \tag{4.22}$$

$$\frac{\partial P^*}{\partial C_{dw}} \sim 1.8 \times 10^{6}[N/m^2] \tag{4.23}$$

Therefore, a 10 % error in L, W, e, C_{da}, and C_{dw} (∼110 km, 10 km, 0.2, 3.5 $\times 10^{-4}$ and 5.5 $\times 10^{-4}$) leads to 10 %, 30 %, 15 %, 2.5 %, and 4 % error in P^* (∼2.75 kN/m^2, 8 kN/m^2, 4 kN/m^2, 0.7 kN/m^2, and 1.1 kN/m^2), respectively.

4.4 Results

In the following, we test the methods to derive P^* using simulated fields from RIOPS. We, then, apply the method to real sea-ice drift data observed with the buoys in M'Clintock Channel. Finally, we discuss shortcoming and uncertainties associated with the P^*.

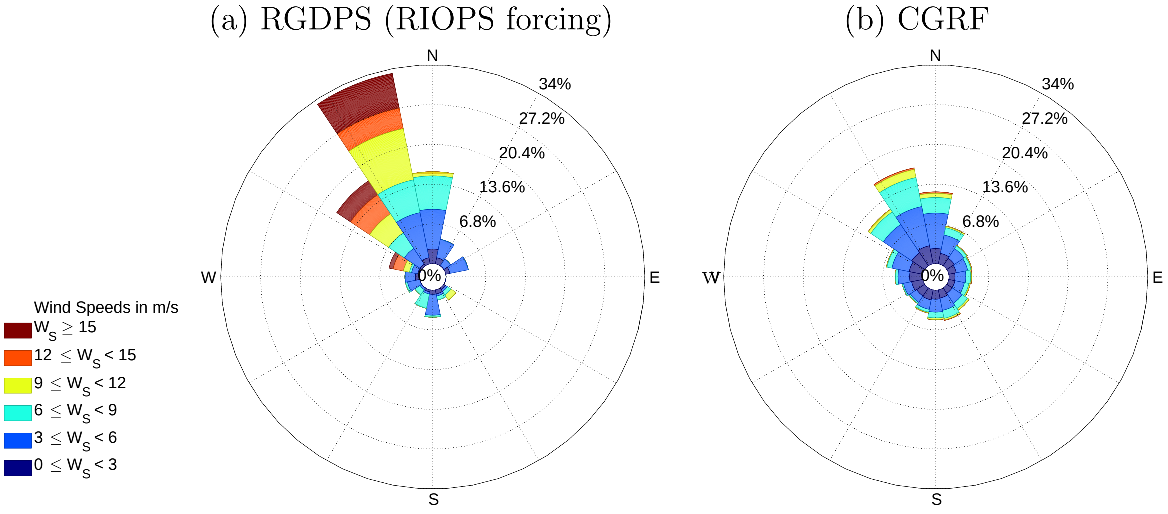

Figure 4.3: Wind rose of (a) 40-m wind from RGDPS (RIOPS forcing) from December 2014 to January 2015 in M'Clintock Channel, and (b) 10-m wind from CGRF from January 2007 to December 2012 in M'Clintock Channel.

4.4.1 Proof of Concept

Surface winds in M'Clintock Channel are mainly aligned with the long axis of the channel due to orographic effect [*Samelson and Barbour*, 2008]. In fact, 33 % of the 40-m wind used to force RIOPS are south-southeastward, and more than 63 % of the strong wind (higher than 15 m/s) are south-southeastward (see Figure 4.3 a). In the following, we use only the cases where the wind blows parallel (± 20°) to the long axis of the channel. We define the sign of the surface wind stress as positive when the wind velocity component along the long axis (y-axis in Figure 4.6 f) is south-southeastward (i.e. predominant direction of wind and ice velocity)

In M'Clintock Channel, the ocean drag is not negligible. In fact, the magnitude of the ocean and air drags are comparable in all seasons (see Figure 4.4 a). This is due to significant tidal currents that are much larger than the mean current (0.35 cm/s). The semi-diurnal tides have a period of 12.7 hr and are modulated by longer period variability of 13.7 days associated with spring-neap tides. The tidal signal in the water drag term is important especially in the winter when the ice is landlock (ice velocity is equal to zero). In the summer, the internal ice stresses are negligible, and the ice-ocean

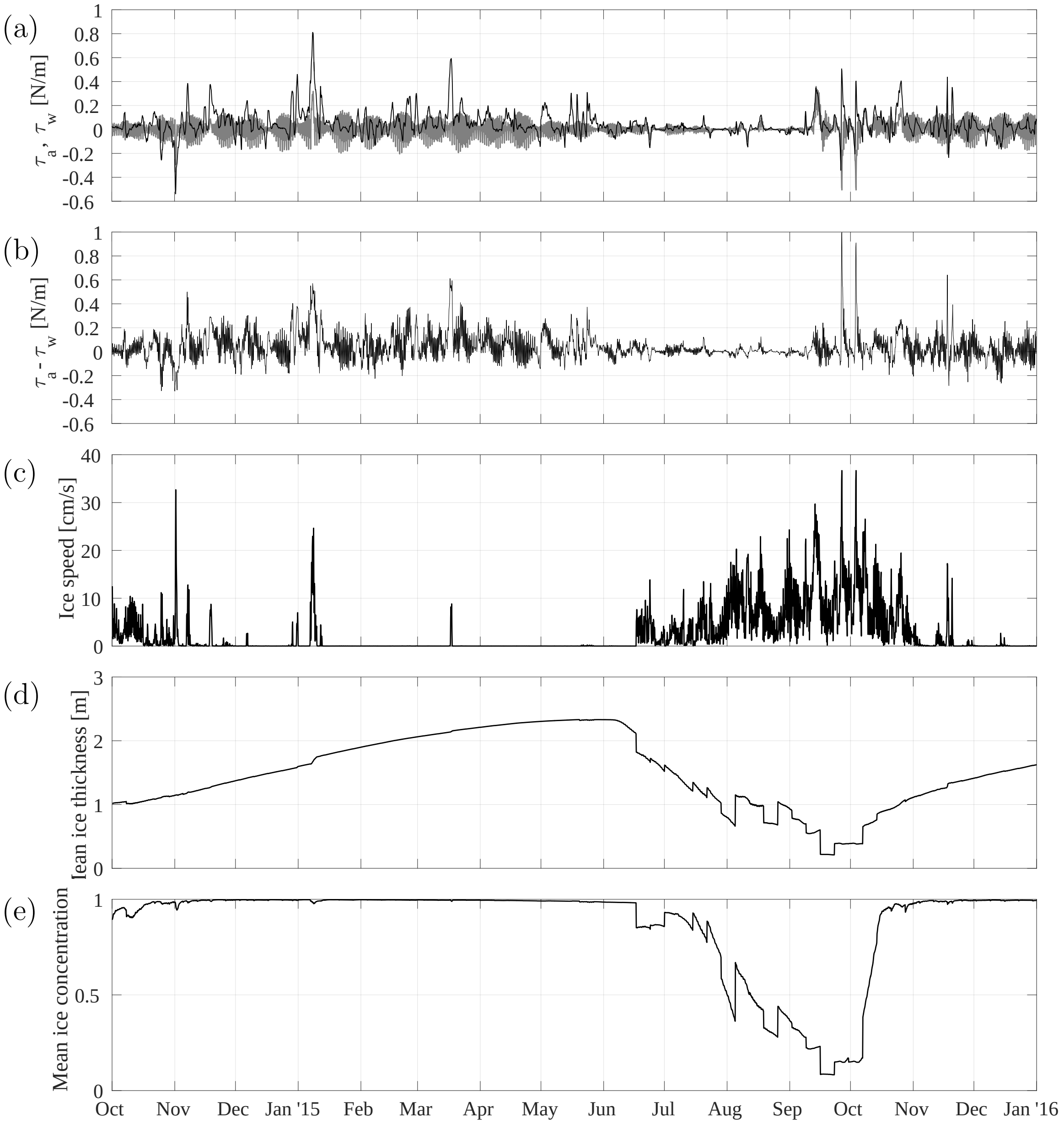

Figure 4.4: Time series of RIOPS (a) surface winds (black line) and ocean drag (grey line), positive when the y-axis components (along the channel axis, see Figure 4.6 f) are positive; (b) sum of wind surface drag and ocean drag; (c) ice speed; (d) sea-ice thickness; and (e) sea-ice concentration for the time window covering from October 2014 to December 2015. The data shown are spatially averaged over the M'Clintock Channel (see Figure 4.6 e)

drag and the air-ice drag are in balance. For this reason, the sea ice moves in order to make the ice-ocean drag equal to air-ice drag (i.e. sea-ice velocity gains tidal signal) and the tidal signal in the water drag becomes small (see Figure 4.4a).

The simulated sea-ice drift by RIOPS shows a period of continuous drift from the Fall to approximately 10 November 2014, followed by a period of intermittent sea-ice drift from 10 November 2014 to 12 January 2015 (see Figure 4.4 c). In the following, we refer to the time period between three weeks before and one week after the landlock onset (here 12 January 2015) as the transition phase because this includes the time of intermittent drift. During the transition phase (from 22 December to 19 January), the mean sea-ice concentration in M'Clintock Channel remains above 0.98, and the sea-ice thickness increases from 1.34 m to 1.81 m, the maximum wind velocity is 22.6 m/s south-southeastwards, and the maximum observed ice speed is 10.8 cm/s towards south-southeast (see Figure 4.5). The sea ice thickens more rapidly when the ice moves (e.g. 7 - 9 January, 2015, see Figure 4.5) than by thermodynamic process alone because thicker ice flows in the domain from the north or sea ice deforms (ridges) in the south.

During the transition phase, the sea ice becomes landlock on 12 January 2015. The sea ice is landlock until it breaks up on 17 June 2015 (see Figure 4.4 c). Note that we include in the landlock ice season short lived (less than one day) ice motion caused by anomalously large surface stresses when the ice pack is otherwise fast (e.g. March 17, 2015). The mean ice thickness in M'Clintock Channel during the landlock season increases from 1.75 m to 2.33 m on 20 May 2015 when the melt onset occurs. The ice break-up occurred 28 days after the melt onset. This was followed by a drop of ice concentration to value approximately equal to 0.85 (see Figure 4.4). Thus, the break-up occurs due to decrease of sea-ice concentration (i.e. the sea-ice exports toward south or the sea-ice edge moves to north), not only due to the thinning of sea ice.

When sea ice first forms in M'Clintock Channel, it drifts southward until the onset of the landlock ice season. Northwest of Gateshead Island, the sea ice ridges due to land-ice interactions, and the ice thickness reaches approximately 3 m (Figure 4.6 c). This is double the ice thickness in the centre of the channel, where the ice thickens

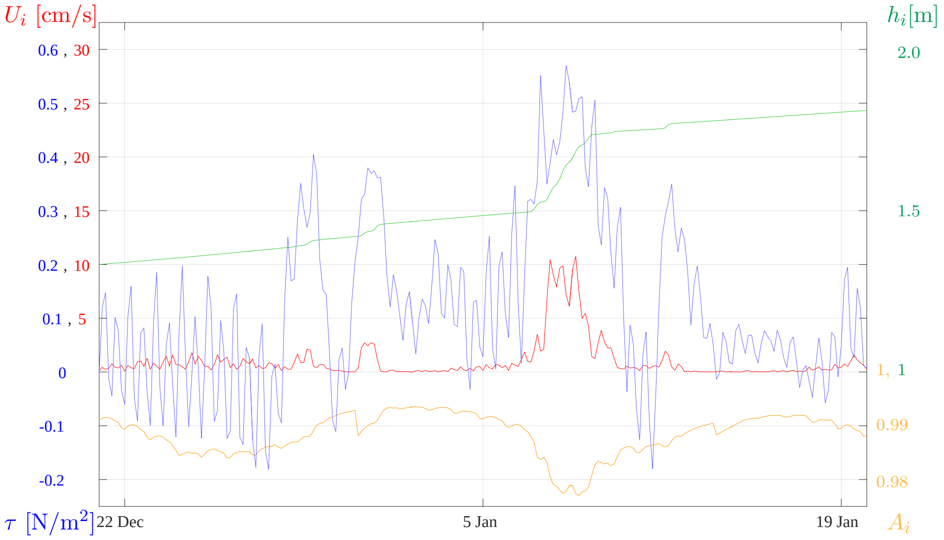

Figure 4.5: Time series of sum of surface wind and ocean drag ($\tau = \tau_a + \tau_w$ in blue), positive when the y-axis components (along the channel axis, see Figure 4.6 f) are positive, ice speed (U_i in red), ice concentration (A_i in orange), and ice thickness (h_i in green) for the time window covering from three weeks before and one week after the onset of landlock ice (i.e. transition phase). The data shown are spatially averaged over the M'Clintock Channel (see Figure 4.6 e). The axis label colours correspond with the line colours on the figure.

mainly via thermodynamic processes. The thicker ice acts as a lateral boundary and defines a 'new' channel with a width (W) of 150 km from Storkerson Peninsula to the Prince of Wales Island west of Ommanney Bay (see Figure 4.1 and 4.6 g). The shear stresses on the east and west coastlines of this new channel remains close to the yield condition (maximum) even after the onset of the landlock season (see Figure 4.6 b and g). In this analysis, we define the length of the channel as the distance from the south shore of Bathurst Island in the Austin Channel where the normal stresses are nearly zero to the north shore of Royal Geographical Society Island in Victoria Strait where the maximum normal stress is observed (L = 780 km, see Figure 4.6 a). The exact location of the end of the channel, where sea-ice deformations will take place, depends on the presence of multi-year ice in the region north of Victoria Strait which will act as a solid boundary where the ice drift speed is zero (see for instance, Figure 4.6 c and h). The spatial distribution of the mean normal stress (σ_I) shows that the compressive stress increases gradually from south of Bathurst Island to Stefansson Island and some

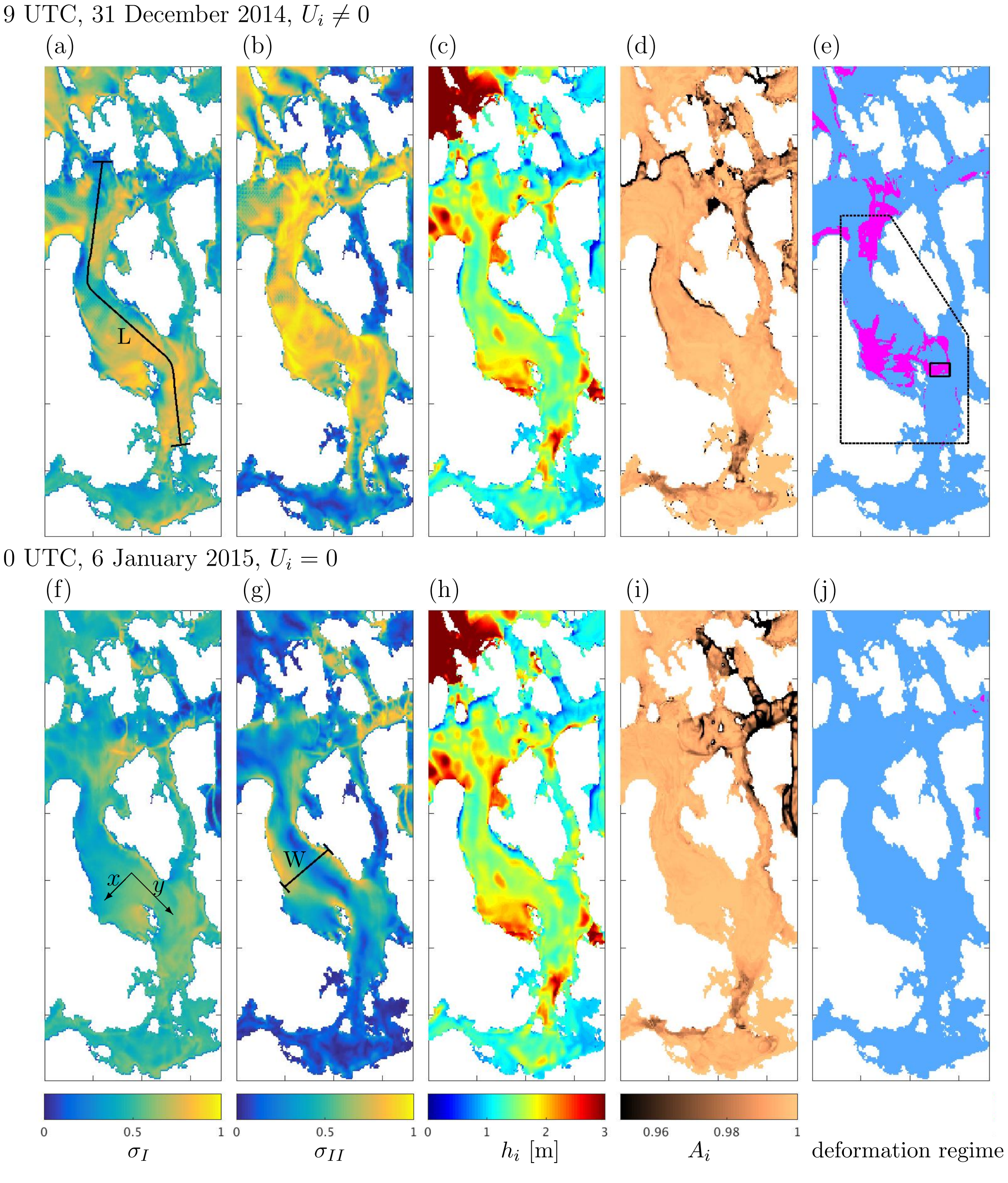

Figure 4.6: Normalized (a, f)normal stress (σ_I) and (b, g) maximum shear stress (σ_{II}), (c, h) ice thickness (h_i), (d, i) sea-ice concentration (A_i), and (e, j) sea-ice deformation regime (magenta: plastic, blue: viscous) in M'Clintock Channel during the transition phase (top row) at 9 UTC 31 December 2014 when average ice speed is non-zero, and (bottom row) at 0 UTC 6 January 2015 when the average ice speed is zero. All data are from RIOPS. The black dotted line in panel (e) marks the domain over which the wind, ocean current, sea-ice velocity, and sea-ice concentration are averaged, and the black solid square is the domain over which the ice thickness is averaged for the P^* estimate. The length L and width W (see Figure 4.2 and equation (4.2)) are defined on panels (a) and (g), respectively.

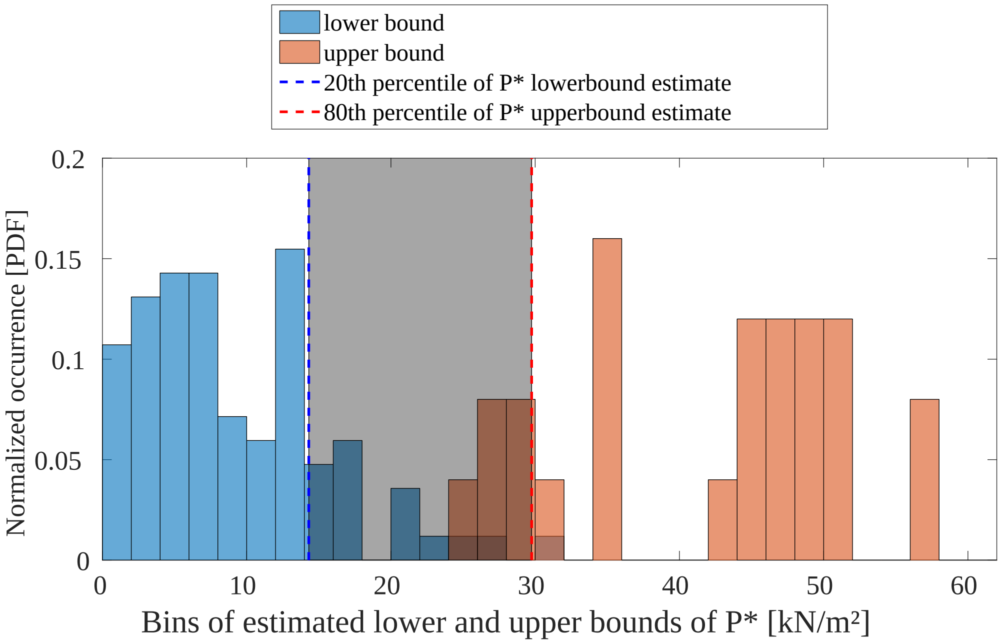

Figure 4.7: Histogram of lower (blue) and upper (red) bounds estimates of sea-ice compressive strength (P^*) derived from RIOPS data averaged over M'Clintock Channel for the transitional period from 10 November 2014 to 31 January 2015. The histogram is normalized such that the integral of the area under the curve is equal to one. Grey shading indicates the range of the P^* estimate.

stress is carried to the region south of Stefansson Island, where the normal stress again increases until King William Island (See Figure 4.1 and 4.6 a). The transmission of normal stress along the length of the channel is observed for all wind event along the axis of the channel whether the ice is in the viscous or plastic regime (see Figure 4.6 a and f).

Using equation (4.13), we calculate upper or lower bounds of $P*$ every three hour during the transition phase (see Figure 4.7) with the RIOPS data when ice moves or is still. In this equation, we calculate the surface air-ice and ice-ocean stresses using the spatially averaged wind and ocean current over the entire M'Clintock Channel (see Figure 4.6 e). Note that we use the average sea-ice thickness over a smaller region north of Victoria Strait (Figure 4.6 e) in equation (4.13). This is done because the thinner ice in this region will fail first and set the timing of the landlock ice onset. The smaller domain is located in the region where the wind fetch is longest and the plastic deformations in compression occur frequently (Figure 4.6 e).

To account the uncertainties given with the assumptions we made to simplify the force balance, we cut 20% highest and lowest values which is obtained for lower and upper bounds respectively. Therefore, we define 80th percentile of lower bound as the reference value of lowest value the P^* possibly be (P^*_{min}), and 20th percentile of upper bound as the reference value of highest value the P^* possible be (P^*_{max}), instead of using infimum and supremum. We obtained 14.3 kN/m^2 for P^*_min, whereas 29.7 kN/m^2 for P^*_{max} (see Figure 4.7). This range includes the P^* value of 27.5 kN/m^2 that is used in the RIOPS. In the following section, we apply this method to in-situ buoy data in order to estimate the sea-ice mechanical strength (see section 4.4.2).

4.4.2 Buoy Data Analysis

We now apply the method described in Section 4.3, using in-situ sea-ice drift observations to identify the transition between the drifting and fast ice. The wind used for this analysis is from the Canadian Meteorological Centre's Global deterministic prediction system reforecast (CGRF) of Environment and Climate Change Canada (see Section 4.2.3). Note that the wind of CGRF is the wind at 10-m from the surface, and different from the 40-m wind of RGDPS (the RIOPS forcing) used for the proof of concept presented in Section 4.4.1. In principle, this analysis should be conducted using the same wind forcing as used in the proof of concept. This is kept for future work and will be done prior to submission to the journal. In the following, the thickness of first-year ice is calculated using the 1D sigma-coordinate thermodynamic model of *Huwald et al.* [2005] forced with CGRF atmospheric fields at the buoy location. Note that we must rely on an estimate of the mean ice thickness from the sigma-coordinate thermodynamic model. In all ice thickness simulations presented following, we assume a constant (in time) climatological snow depth of 15 cm [*Warren et al.*, 1999].

Similar to the RGDPS surface wind forcing, the CGRF 10-m surface wind stresses are mainly aligned with the long axis of the M'Clintock Channel due to orographic effect [*Samelson and Barbour*, 2008]. 20 % of the 10-m wind are south-southeastward,

(a) MC07

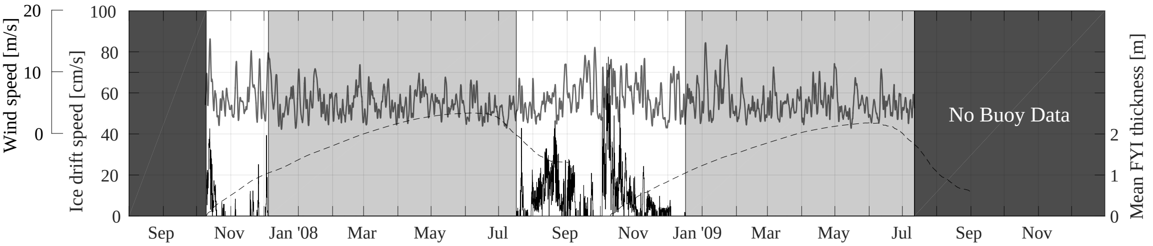

(b) MC09

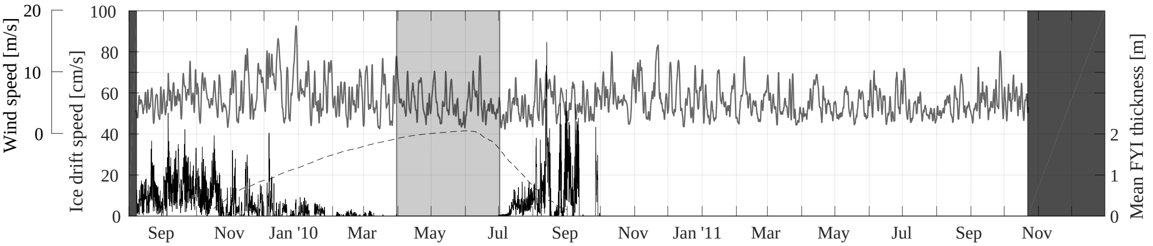

(c) MC11

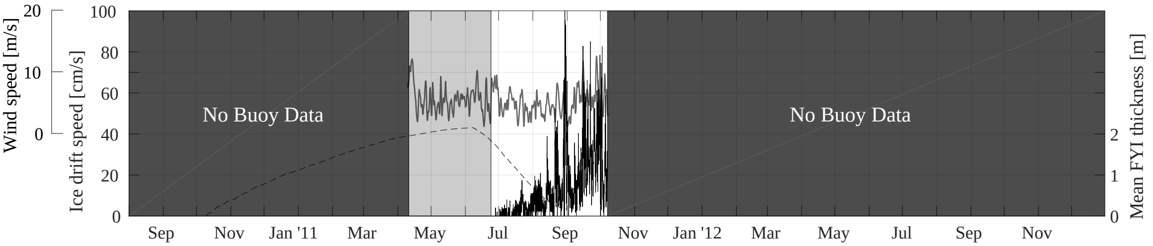

(d) MC13

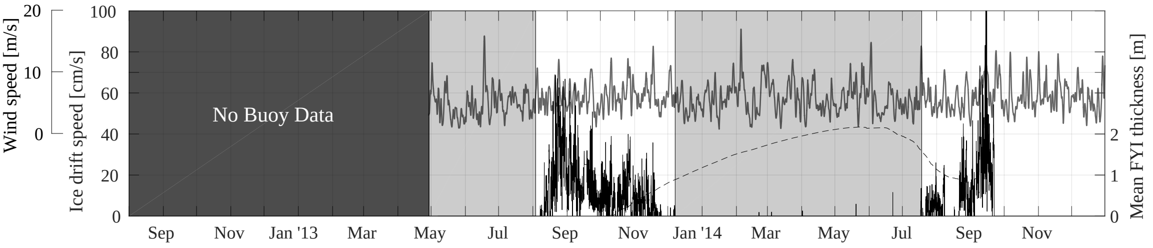

Figure 4.8: Time series of drift speed (black solid line), mean FYI thickness (black dotted line), and 1-day averaged CGRF wind speed (grey thick line) for (a) MC07, (b) MC09, (c) MC11, (d) MC13, (e) VM10, (f) BM12, and (g) VM12. Light shading indicates the landlock season; dark shading indicates no buoy data. Mean FYI thickness is simulated with the 1D thermodynamics model of *Huwald et al.* [2005] forced with the CGRF atmospheric field (air temperature, specific humidity, SW radiation, LW radiation) around the landlock location of each buoy.

(e) VM10

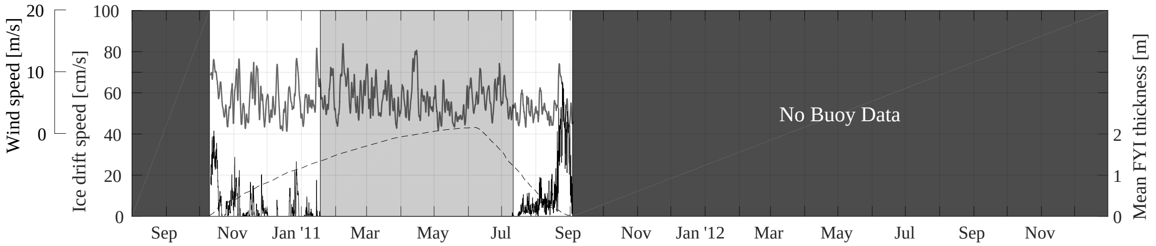

(f) BM12

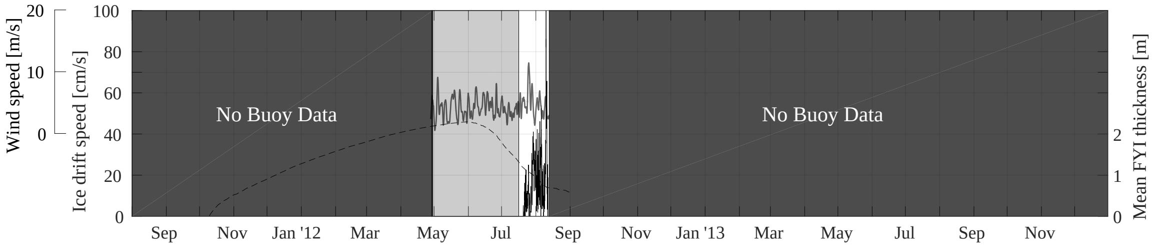

(g) VM12

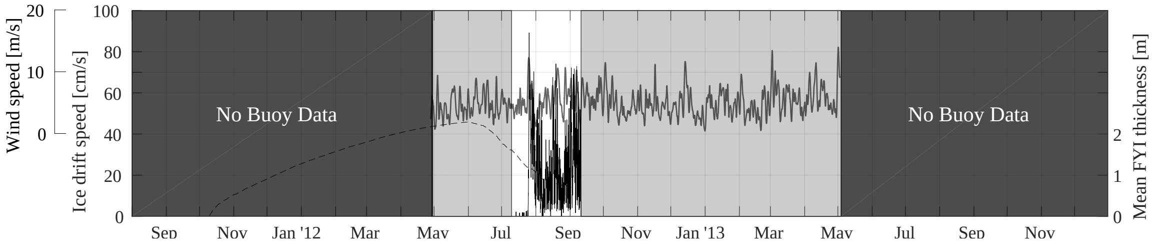

Figure 4.8: (Cont.)

and more than 40 % of the strong wind events (> 10 m/s) are south-southeastward (see Figure 4.3 b). In the following, we again only use cases when the wind blows almost parallel to the long axis of the channel (± 20°) and define positive velocity when the wind is south-southeastward.

Prior to 2014 (recall that our buoys were deployed in 2008, 2009, 2013), RIOPS data are only available as 4-day mean fields. For this reason, we use the same high frequency ocean current simulated for 2014 for our sea-ice compressive strength estimates, assuming that the interannual variability in ocean-ice stress is small. This assumption will be tested by looking at more recent RIOPS model output made available by Environment and Climate Change Canada. This is kept for future work. In the following, the total ocean current is defined as the superposition of the mean flow and two sinusoids as seen in the RIOPS ocean currents in M'Clintock Channel in winter (see detail in Section 4.4.1). The amplitudes of two tides are calculated from the

Table 4.2: Data summary of SVPs (continued): buoy identification name, date of landlock ice onset and break up, buoy position during the landlock ice season.

Buoy ID	Onset		Breakup		landlock position
	Date	hi [cm]	Date	hi [cm]	
MC07	4 Dec ’07	104.50	17 Jul ’08	197.00	73.81°N 105.93°W (VMS)
	16 Dec ’08	104.63	–	–	70.75°N 96.61°W (MCT)
MC09	10 Mar ’10	188.59	27 Jun ’10	188.59	71.04°N 100.58°W (MCT)
VM10	18 Jan ’11	134.24	6 Jul ’11	136.47	73.36°N 112.27°W (VMS)
MC11	–	–	24 Jun ’11	183.81	74.00°N 104.56°W (VMS)
BM12	–	–	17 Jul ’12	128.56	76.92°N 104.20°W (BMC)
VM12	–	–	11 Jul ’12	158.64	76.71°N 105.53°W (BMC)
MC13	–	–	3 Aug ’13	144.44	75.81°N 104.49°W (BMC)
	7 Dec ’13	88.91	13 Jul ’14	175.64	70.97°N 100.71°W (MCT)

ocean water velocity data of RIOPS, with semidiurnal (12.7 hours) and spring-neap (14 days) tidal periods. Note that we do not know the a priori phase of the tidal signal. In the following, we presents only the result using the phase of tides chosen by applying the methods described in Section 4.3 for all phases and find the phases that minimize the uncertainty in P^*.

The observed sea-ice drifts from MC07, MC09, and MC13 are southward in M’Clintock Channel. These southward sea-ice drifts in M’Clintock Channel are in accord with available ocean current meter measurements [*Fissel et al.*, 1988; *Barry*, 1993], modelled CAA ocean circulation [*Wang et al.*, 2012], and RIOPS dataset. In all three buoy dataset, the landlock ice season is present (see Figure 4.8 a and d, and Table 4.2). The landlock ice onset is relatively consistent from year to year (two onsets observed with MC07 on 4 December 2007 and 16 December 2008, and one onset observed with MC13 on 7 December 2013), except for 2009-10 winter when the landlock ice season started only on 10 March 2010 (see Figure 4.8 b). The simulated first-year ice thickness in the winter of 2009-10 is comparable to other winters (2008-09 or 2013-14). This buoy spent its winter (until March) in continuous motion just north of a small island (Gateshead Island) where tidal forcing is believed to be more important. On the other hand, the date of landlock ice breakup events that are measured with the buoys, is more consistent (17 July, 27 June and 13 July in 2008, 2010 and 2014 observed with MC07, MC09 and MC13, respectively. See Table 4.2). Note that the second landlock break-up event of MC07 is not observed since the buoy stop transmitting data on 8 July 2009 before the sea ice started moving.

The locations of buoys MC09 and MC13 during the landlock ice seasons of 2009-10 and 2013-14, respectively, are within 10 km of each other just north of Gateshead Island (see Figure 4.1); yet one buoy continued to drift back and forth with tides until 10 March while the other buoy was fast in December – note that the mean ice thickness for both winters are similar in magnitude. In this region, large gradient in surface current velocity in the offshore direction are present because of the narrowing of the Channel (see Figure 4.15 c). Considering this large spatial variability in surface ocean current, we hypothesize that one buoy only a few kilometres away from another may have seen considerably different ocean forcing, delaying the onset of landlock ice for MC09.

In fact, MC09 drifted within a radius of only 7 km between middle of December and March (before the landlock ice onset that year). A Fourier analysis of the drift speed during that period has a peak at $\sim$ 14 days period, suggesting that spring/neap tides are responsible for this motion (result not shown). The average wind in winter (Dec-Jan-Feb) in M'Clintock Channel was larger in 2009-10 than 2013-14. The average CGRF winter wind in M'Clintock in 2009-10 was 7.2 m/s and the one in 2013-14 was 5.9 m/s. This may have helped keep the buoy in motion but the fact that we see a peak at 14 days in the Fourier Transform suggests that the reason of the continued motion is linked with the basal ice-ocean stresses. These two buoys in the same location but with very different behaviour suggest that we are near a threshold in term of the

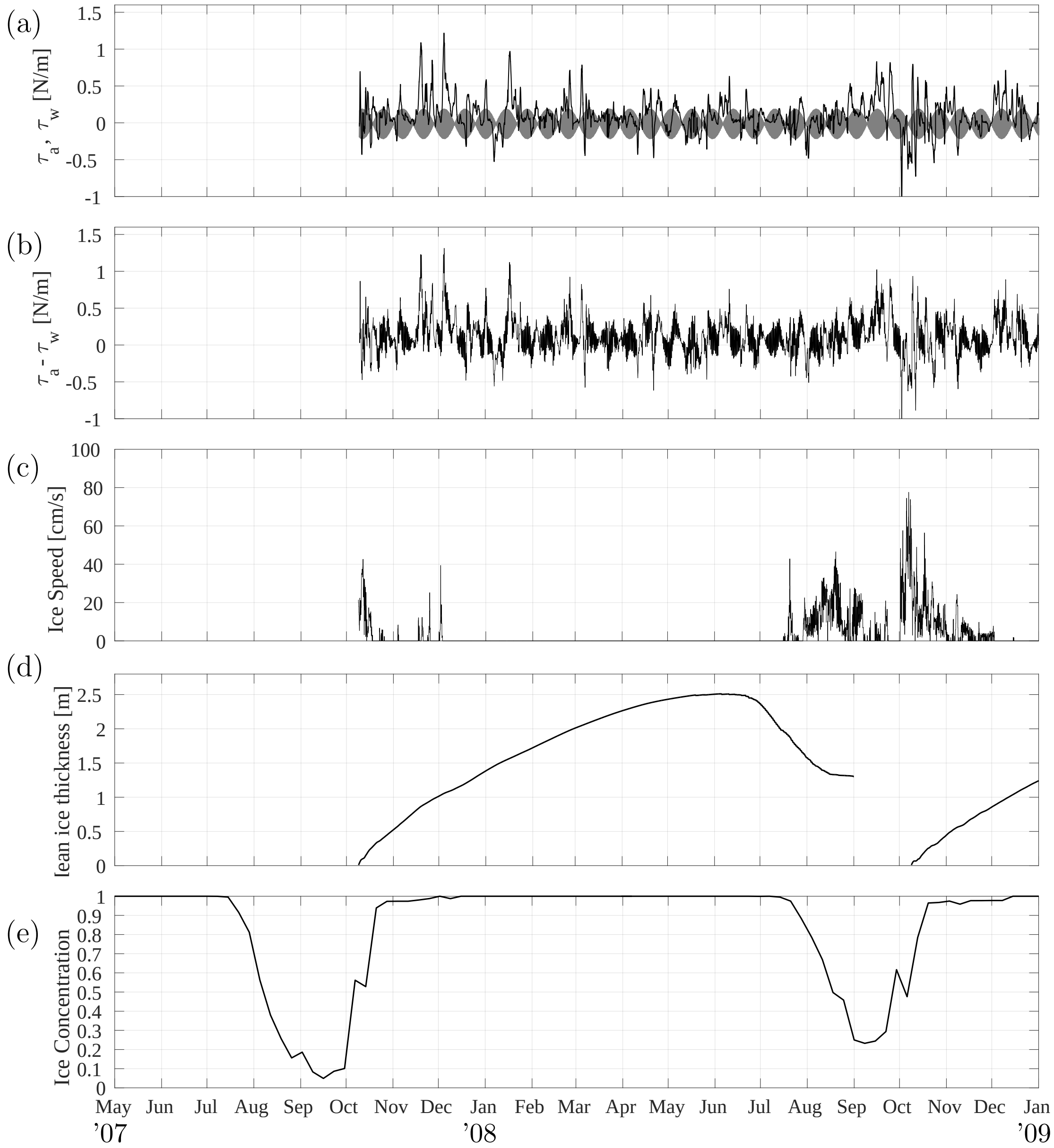

Figure 4.9: Time series of (a) wind surface (τ_a, black line) and ocean drag (τ_w, grey line), positive when the y-axis components (along the channel axis, see Figure 4.6 f) are positive; (b) sum of wind surface and ocean drag ($\tau_a + \tau_w$); (c) ice drift speed observed with MC07; (d) sea-ice thickness; and (e) sea-ice concentration in M'Clintock Channel in the year of MC07 (2007 May -2008 Dec). τ_a is calculated from CGRF wind data, and τ_w is calculated with the ocean current estimated from the 2014 RIOPS data. The ice thickness is simulated with the 1D thermodynamic model of *Huwald et al.* [2005] forced with the CGRF atmospheric field around the landlock location of each buoy. The sea-ice concentration is from the Canadian Ice Service gridded product. τ_a, and A_i are averaged over M'Clintock Channel (see Figure 4.6 e).

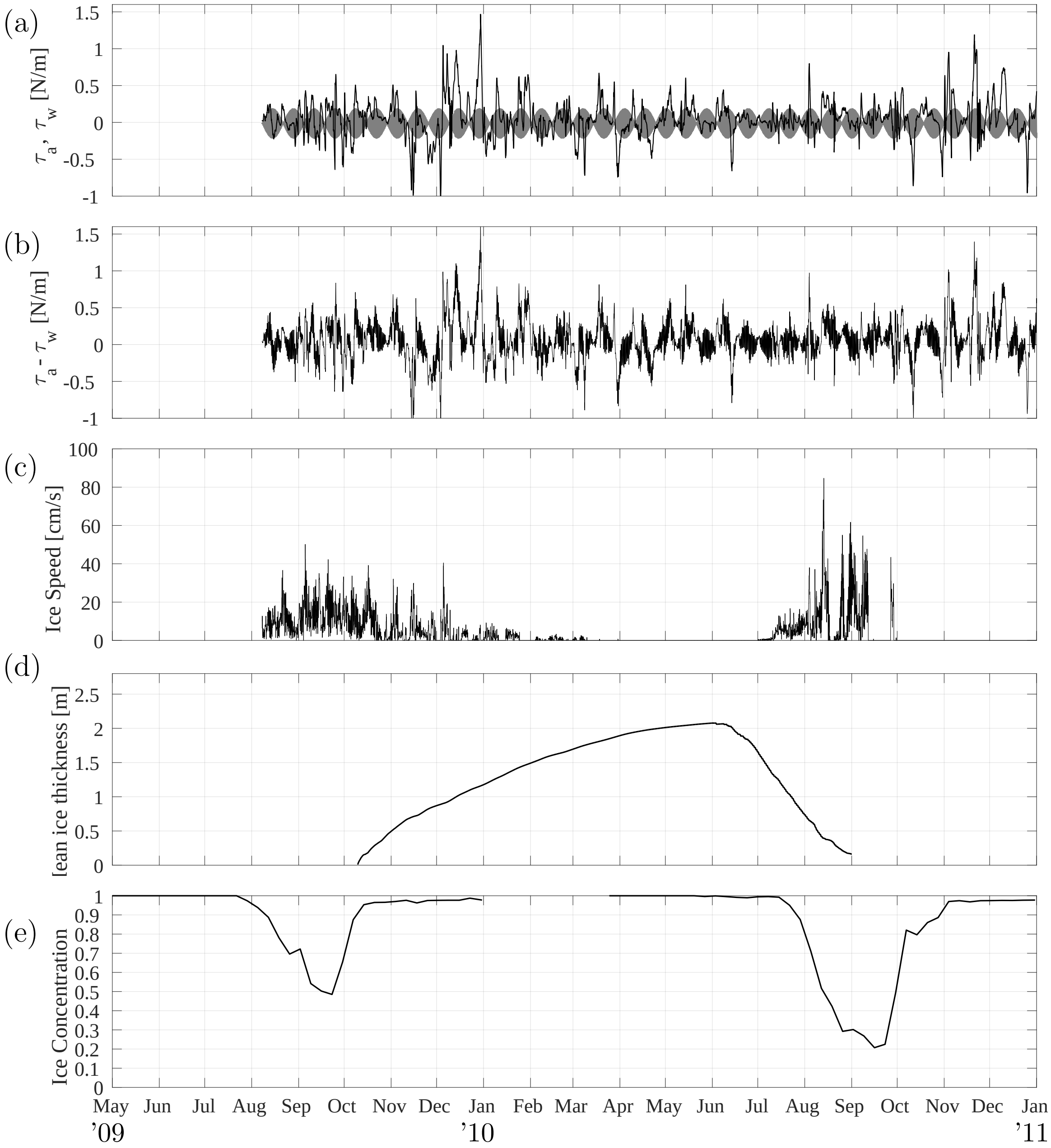

Figure 4.10: Time series of (a) wind surface (τ_a, black line) and ocean drag (τ_w, grey line), positive when the y-axis components (along the channel axis, see Figure 4.6 f) are positive; (b) sum of wind surface and ocean drag ($\tau_a + \tau_w$); (c) ice drift speed observed with MC09; (d) sea-ice thickness; and (e) sea-ice concentration in M'Clintock Channel in the year of MC09 (2009 May -2010 Dec). τ_a is calculated from CGRF wind data, τ_w is calculated with the simple ocean current estimated from the 2014 RIOPS data. The ice thickness is simulated with the 1D thermodynamic model of *Huwald et al.* [2005] forced with the CGRF atmospheric field around the landlock location of each buoy. The sea-ice concentration is from the Canadian Ice Service gridded product. τ_a, and A_i are averaged over M'Clintock Channel (see Figure 4.6 e).

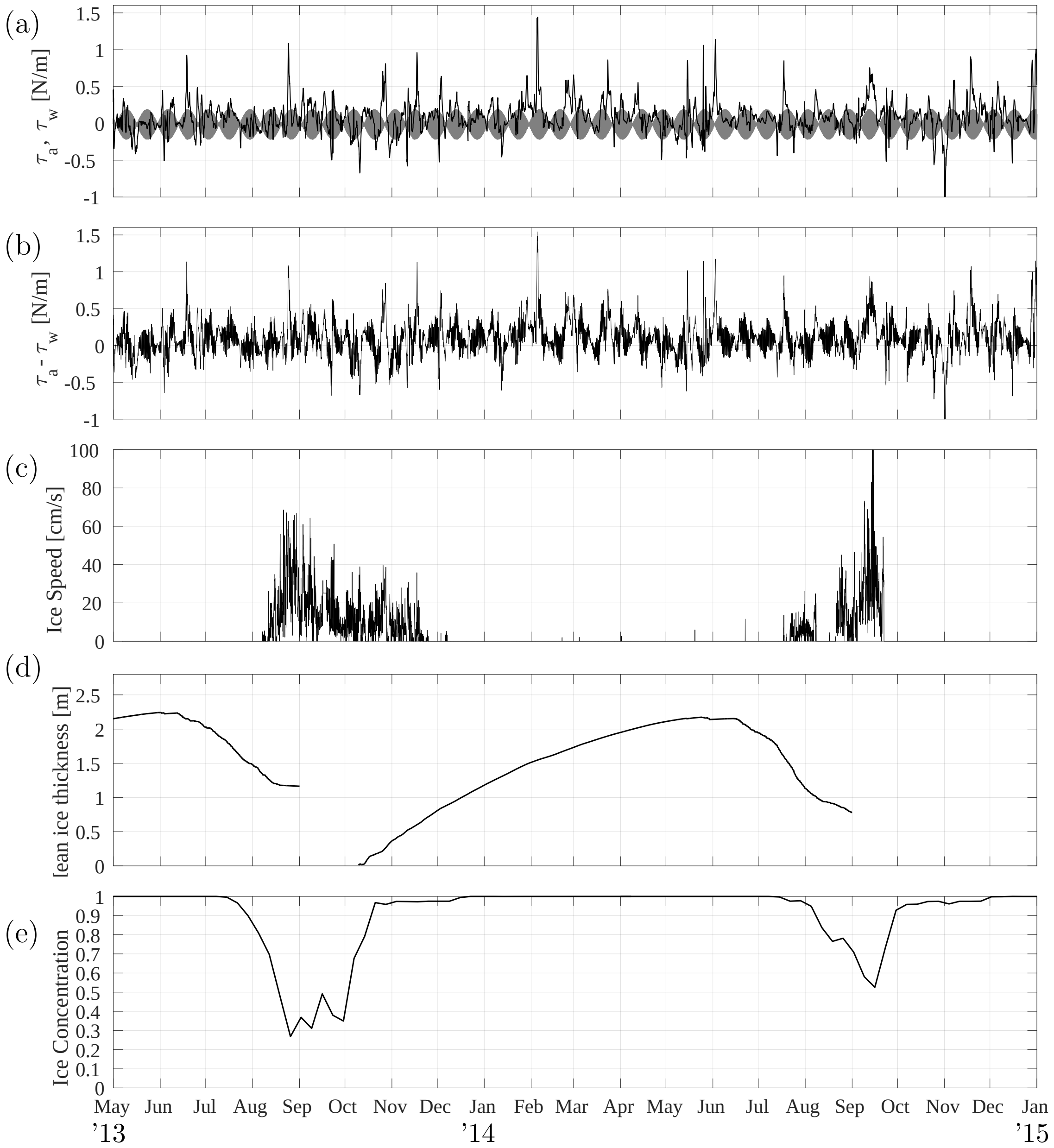

Figure 4.11: Time series of (a) wind surface (τ_a, black line) and ocean drag (τ_w, grey line), positive when the y-axis components (along the channel axis, see Figure 4.6 f) are positive; (b) sum of wind surface and ocean drag ($\tau_a + \tau_w$); (c) ice drift speed observed with MC13; (d) sea-ice thickness; and (e) sea-ice concentration in M'Clintock Channel in the year of MC13 (2013 May -2014 Dec). τ_a is calculated from CGRF wind data, τ_w is calculated with the simple ocean current estimated from the 2014 RIOPS data. The ice thickness is simulated with the 1D thermodynamic model of *Huwald et al.* [2005] forced with the CGRF atmospheric field around the landlock location of each buoy. The sea-ice concentration is from the Canadian Ice Service gridded product. τ_a, and A_i are averaged over M'Clintock Channel (see Figure 4.6 e).

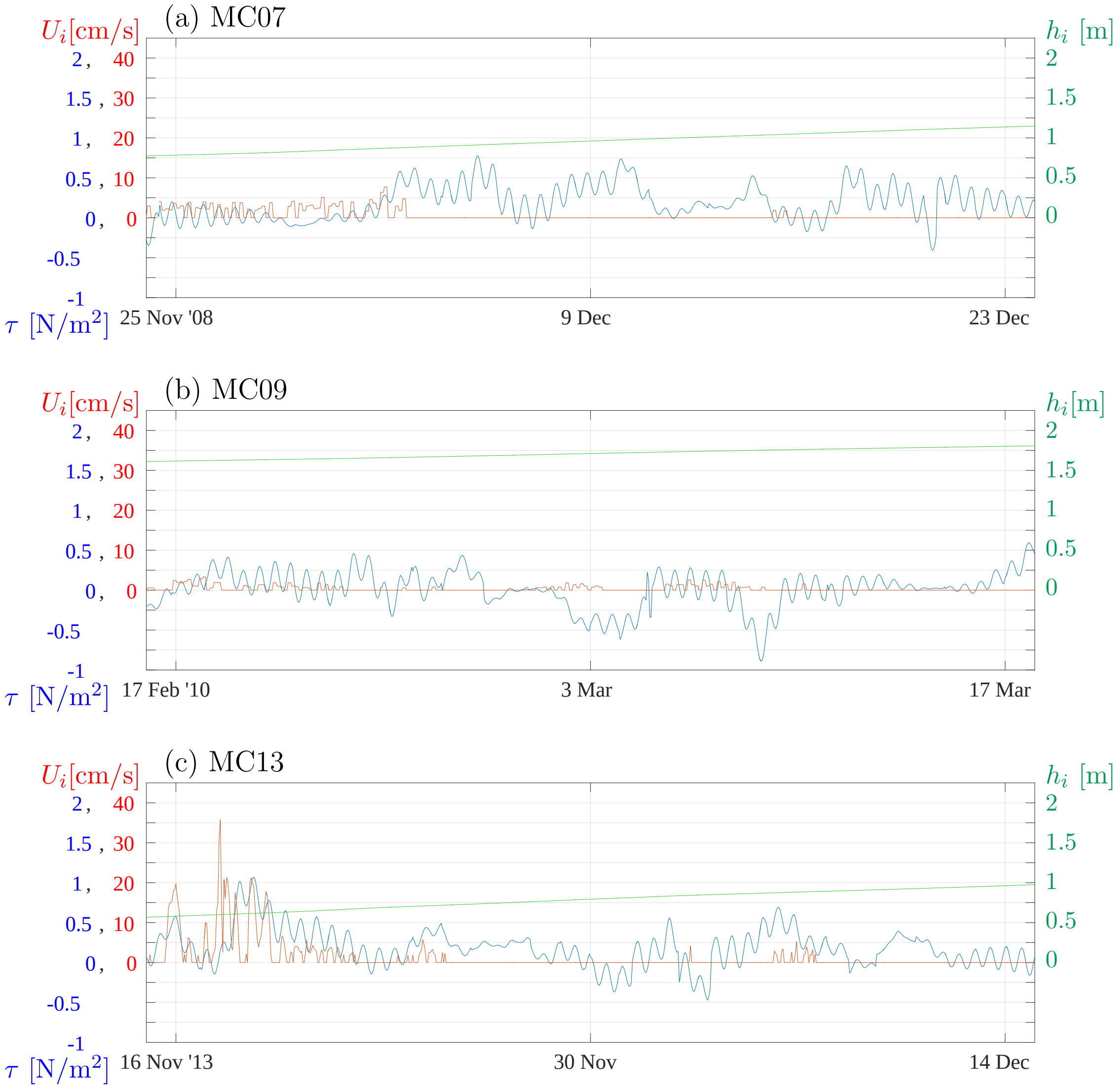

Figure 4.12: Time series of sum of surface wind and ocean drag ($\tau = \tau_a + \tau_w$ in blue) along the channel axis, positive in south-southeastward; ice speed (U_i in red); and mean ice thickness (h_i in green) for the time window covering from three weeks before and one week after the onset of landlock ice (i.e. transition phase). The axis label colours correspond with the line colours on the figure. τ_a is calculated from the CGRF wind data correspond with the time window, τ_w is calculated with the simple ocean current estimated from the 2014 RIOPS data. The ice thickness is simulated with the 1D thermodynamic model of *Huwald et al.* [2005] forced with the CGRF atmospheric field around the landlock location of each buoy. τ_a is averaged over M'Clintock Channel (see Figure 4.6 a, thick solid line). Each panels show the data for (a) MC07, (b) MC09, and (c) MC13.

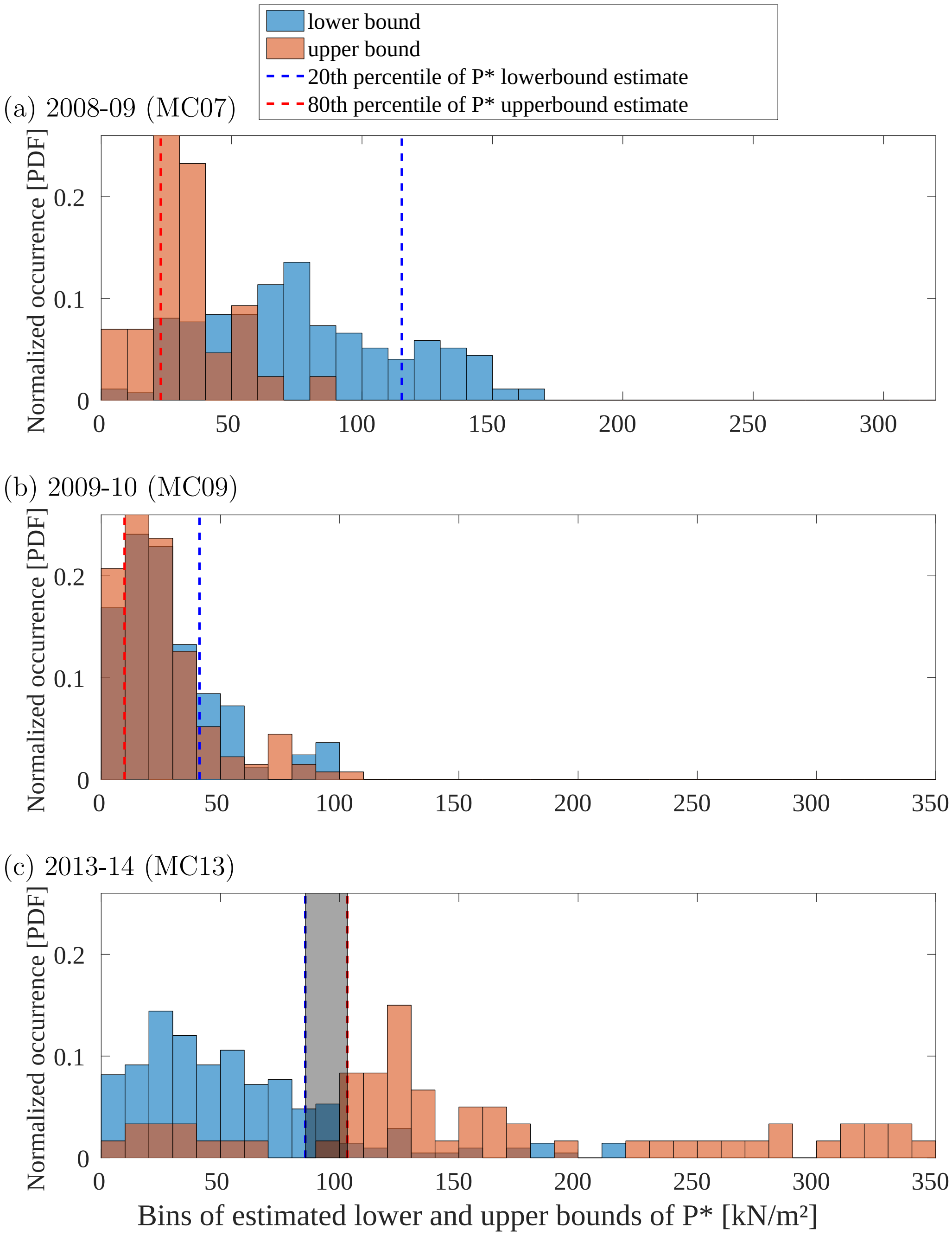

Figure 4.13: Histograms of lower (blue) and upper (red) bounds estimates of sea-ice compressive strength (P^*) for the time window covering three weeks before and one week after the landlock onset (i.e. transitional period) of (a) MC07, (b) MC09, and (c) MC13. Calculations are done with the CGRF wind averaged over M'Clintock Channel; the simple ocean current that including the annual mean, and semidiurnal and spring/neap tides derived from the 2014 RIOPS data; and the mean ice thickness simulated with the 1D thermodynamic model of *Huwald et al.* [2005] forced with the CGRF atmospheric field around the landlock location of each buoy. The histograms are normalized such that the integral of the area under the curve is equal to one.

mechanical loading that is necessary to induce motion during winter. This could be used to provide a narrow constraint on our estimate of the mechanical strength of sea ice (left for future work).

In the following, we present lower and upper bound estimates derived from the in-situ sea-ice drift. As mentioned above the ocean drag on the ice is taken from the RIOPS model output (2014-15 winter) and the sea-ice thickness during the transition period is calculated using the 1D thermodynamic model of *Huwald et al.* [2005].

The analysis using in-situ buoy data does not show clear separation between the upper and lower bounds of sea-ice compressive strength estimates – except for MC13 where a separation between the lower and upper bound histograms indicates a P^* value of approximately 94.4 ± 8.8 kN/m^2 (see Figure 4.13 c). The analysis of MC07 and MC09, on the other hand, show either white noise (MC09) with no clear peak in the lower and upper bound estimates or a peak where the lower bound estimates are higher than the upper bound estimate. Clearly, this is unphysical and suggest that the ocean drag from one given year is not representative of another year or a problem exists in the wind forcing. This is discussed in more details in the next section.

4.5 Discussion

As seen above, the histograms of upper and lower bounds derived from buoy data are not all internally consistent. In order to understand better the results, we first look at the wind forcing used to calculate the total surface stresses acting on the sea ice during the transition period. To this end, we look at the correlation between the daily mean ice drift speed and the surface wind stresses during the month of September when the ice is in freedrift, and the wind velocity ($\mathbf{u}_a$) should have strong correlation with respect to the relative ice-ocean velocity ($\mathbf{u}_i - \mathbf{u}_w$) (see equation (4.1) with internal ice stress term set to zero). In fact, the September dataset from RIOPS shows a perfect positive linear relationship ($r = 1.0$) between the spatially averaged (over M'Clintock Channel, see Figure 4.6 e) diurnal relative sea-ice speed ($|\mathbf{u}_i - \mathbf{u}_w|$) and

(a) 2008

Total SIC in Sep MY SIC in Dec

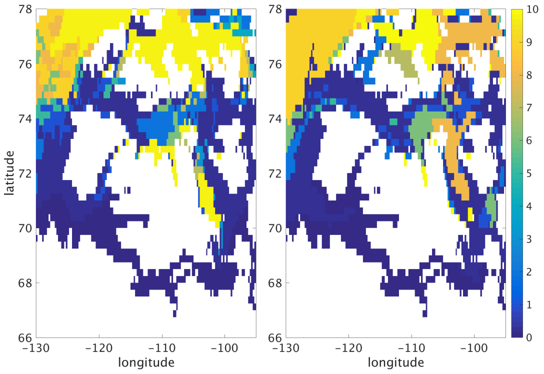

(b) 2009

Total SIC in Sep MY SIC in Dec

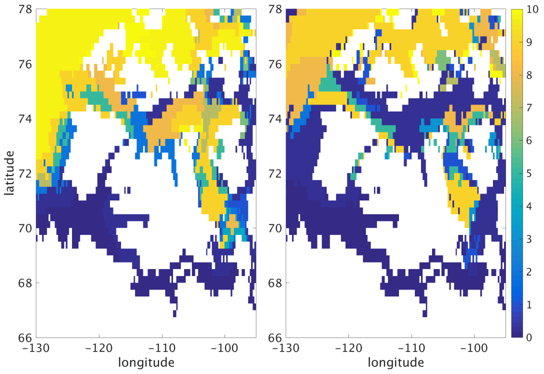

(c) 2010

Total SIC in Sep MY SIC in Dec

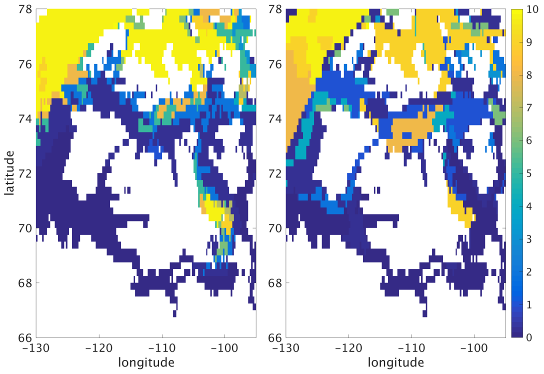

(d) 2011

Total SIC in Sep MY SIC in Dec

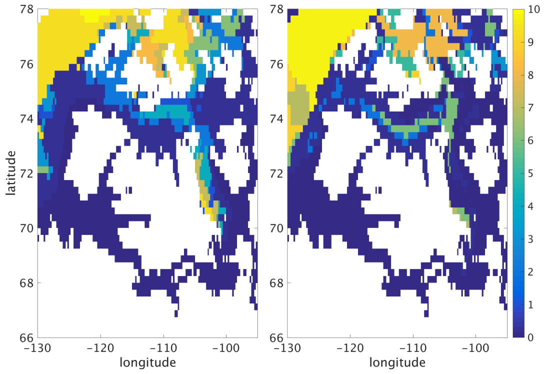

(e) 2012

Total SIC in Sep MY SIC in Dec

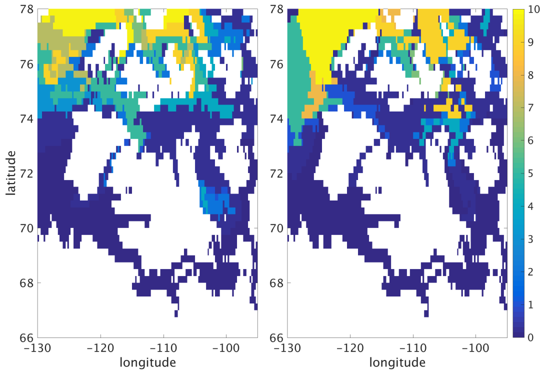

(f) 2013

Total SIC in Sep MY SIC in Dec

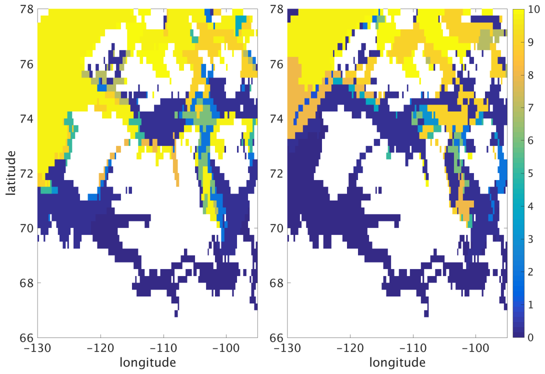

Figure 4.14: Total sea-ice concentrations (SIC) on 9 September (near the time of the minimum sea-ice extent), and multi-year sea-ice concentration on 16 December (around the onset of landlock sea ice) in (a) 2008, (b) 2009, (c) 2010, (d) 2011, (e) 2012, (f) 2013 from the Canadian Ice Service gridded product.

wind speed ($|\mathbf{u}_a|$). Thus, we expect that the strong correlation between the observed ice speed and the CGRF wind speed during summer in M'Clintock Channel at least when the temporal resolution of the data is as low as diurnal. Table 4.3 shows high (statistically significant) correlation between the two variables ($|\mathbf{u}_a|$ from CGRF, and $|\mathbf{u}_i|$ from observations), when they are averaged over time period longer than the tidal period, for MC13 where the histogram shows a clearer separation between the lower and upper bound, and very weak (statistically significant) and near zero (non statistically significant) correlation for MC09 and MC07, respectively. Note that the ocean current is not included when we calculate the correlation between ice and wind speed. This is done because ocean current is not available for those years and RIOPS data demonstrate significantly strong correlation between ice and wind speeds ($r = 0.91$) in September even without ocean current.

Table 4.3: Correlation coefficient and significance level between daily mean CGRF winds (spatially averaged over M'Clintock Channel) and observed sea-ice drift speed in September. The temporal averaging is used to remove the tidal signal in the sea-ice drift time series.

Buoy ID	year	correlation efficient (r)	p-value
MC07	2008	-0.15	0.43
MC09	2009	0.38	0.04
MC13	2013	0.69	$\ll 0.05$

One possible cause of the weak (or lack of) correlation between the wind speed and buoy drift could be the presence of larger amount of multi-year ice (MYI) preventing freedrift in M'Clintock Channel even in September. The presence of multi-year ice at the end of the summer could explain the lack of correlation between sea-ice drift and surface winds since sea-ice interactions would no longer be negligible. In 2008 and 2009 September, when we see weak or lack of correlation present between wind and buoy speed, the buoys were indeed in a region of high multi-year ice concentration (as per the gridded ice chart from CIS – see Figure 4.14 a and b). In contrast, in September 2013, when we see a high correlation between wind and ice speed, drifted near the centre of M'Clintock Channel, where the sea-ice concentration is lower than

0.6 (see Figure 4.14 f, left panel; and 4.15 a). Furthermore, the ice speed of MC13 were faster (18 cm/s) than the other two buoys (5 cm/s and 15 cm/s observed with MC07 and MC09) in September, despite the lower average wind speed (5.6 m/s in September 2013) compare to the average wind speed in 2008 and 2009 (7.2 m/s and 6.4 m/s, respectively). Therefore, we conclude that the high sea-ice concentration is one of the cause of the low correlation between ice and wind speed.

The high SIC in September implies high MYI concentration in December during the transition phases to landlock seasons. The gridded ice chart from CIS, indeed, shows high MYI concentration in M'Clintock Channel in December 2008 and 2009, as well as, September SIC (see Figure 4.14 a and b). When large quantity of MYI is present in a region, the P^* estimate derived from the surface stresses must be divided by the thickness of the MYI – as opposed to the thickness of the first year ice, which is grown only thermodynamically. Given the large uncertainty in the thickness of MYI used in our P^* estimates, we test of the sensitivity of our upper and lower bound estimates to our choice of h_i. When we increase the ice thickness by 1 m for the P^* estimate from MC09, the magnitude of upper and lower bounds decreases and the shape of histograms remains almost the same. Therefore, increasing ice thickness does not lead to a clearer separation between lower and upper bound estimates (see Figure 4.17 a). This is also true when the ice thickness is increased by 2 m, 5m, and even 10m.

The second possible cause of the weak (or lack of) correlation between ice and wind speed is that the observed sea-ice velocity at the buoy location may not be representative of the mean sea-ice velocity over the entire channel. The sea-ice velocity in September varies in space due to the spatial distribution of sea ice as we have seen above. It also varies due to the topography of the Channel (e.g. ice flows faster in the narrower part of channel, see Figure 4.15 b). The temporal mean of standard deviation of RIOPS ice speed in M'Clintock Channel in September 2015 is 11.75 cm/s (mean ice speed is 16.6 cm/s). Furthermore, the correlations for each individual grids are not high as well in RIOPS (see Figure 4.16 b), compare to the high correlation between ice

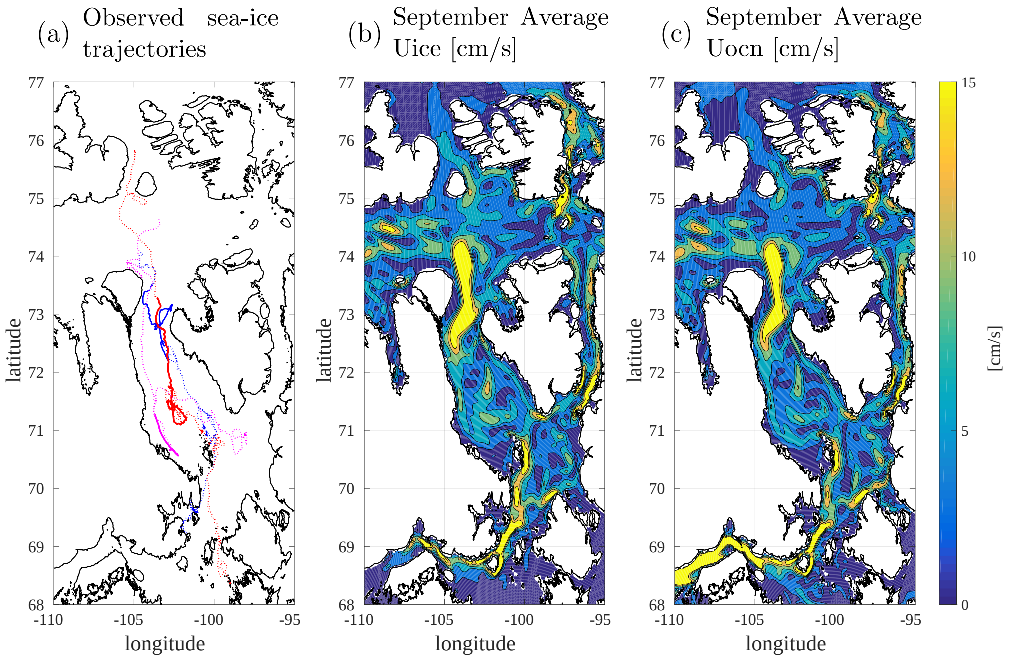

Figure 4.15: (a) The sea-ice drift observed with MC07 (2007 - 2008, magenta), MC09 (2009 -2010, blue), and MC13 (2013 -2014, red). The dotted lines show the sea-ice drift from the deployment time to the last communication of the buoy, and the solid lines show the drift observed in September. (b) The ice and (c) ocean currents speed in M'Clintock Channel and the surrounding regions from RIOPS in September 2015.

and wind speeds averaged over M'Clintock Channel ($r = 0.91$). In fact, MC08 spent more time in a region of low correlation between ice drift speed and surface wind stress because of larger ocean current (see Figure 4.15 c) and the presence of land to the east, when compared with MC13 that spent most of its time in the centre of the channel where the correlation between drift and surface wind stresses is higher (see Figure 4.16 a and b). Thus, the correlation between ice and wind speed depends on the path the buoys take or the location where the observations are taken.

Given that there are large uncertainties in the magnitude of the ocean current, we test the sensitivity of our upper and lower bound estimates to the ocean current strength. To this end, we increase the RIOPS ocean basal stress (τ_w) by a factor of two (Figure 4.17 b). Increasing the amplitude of the tidal signal stretches the histograms of both upper and lower bounds to higher value while keeping the lower values the same. Due to the tidal signal, ocean stress can be very close to zero, and those small ocean stresses remain small and have minor effects on the estimate of upper and lower

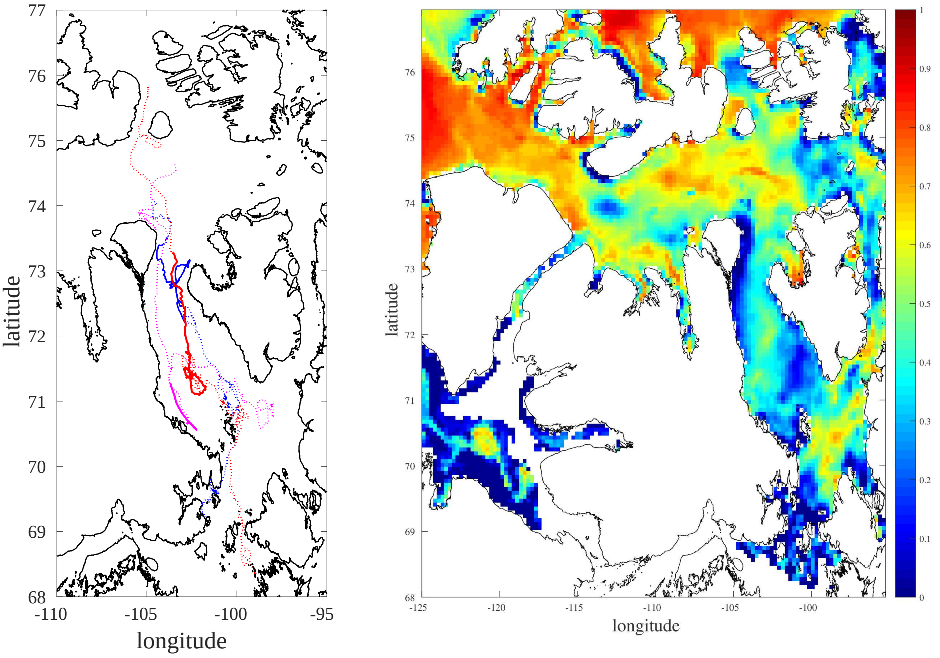

Figure 4.16: (a) The sea-ice drift observed with MC07 (2007 - 2008, magenta), MC09 (2009 -2010, blue), and MC13 (2013 -2014, red). The dotted lines show the sea-ice drift from the deployment time to the last communication of the buoy, and the solid lines show the drift observed in September. (b) Correlation coefficient between RIOPS ice and wind speeds for each grid in the CAA in September 2015.

bounds. Therefore, we still do not see a clearer separation of the upper and lower bound estimates (see Figure 4.17 b). This is also true when the ocean current is increased by a factor of five and ten. Further investigation is needed to quantify the influence of use of the point measurement for the mean ice speed on P^* estimate, other than the uncertainties in ocean current (i.e. land effect).

Another possible source of error is the surface wind stress derived from CGRF. The results suggest that the accuracy of the wind data may not be adequate in M'Clintock Channel in some year, since the strength of correlation between buoy ice speed (point measurement) and CGRF wind data (spatially averaged) change considerably year to year (or location to location) (see Table 4.3). To examine the accuracy of CGRF, our future work includes: comparing the CGRF surface wind with different reanalysis datasets (e.g. The Arctic System Reanalysis (ARS), The Modern-Era Retrospective Analysis for Research and Applications (MERRA), National Energy Research Supercomputing Center of the Department of Energy (NCEP-DOE) Reanalysis 2, European

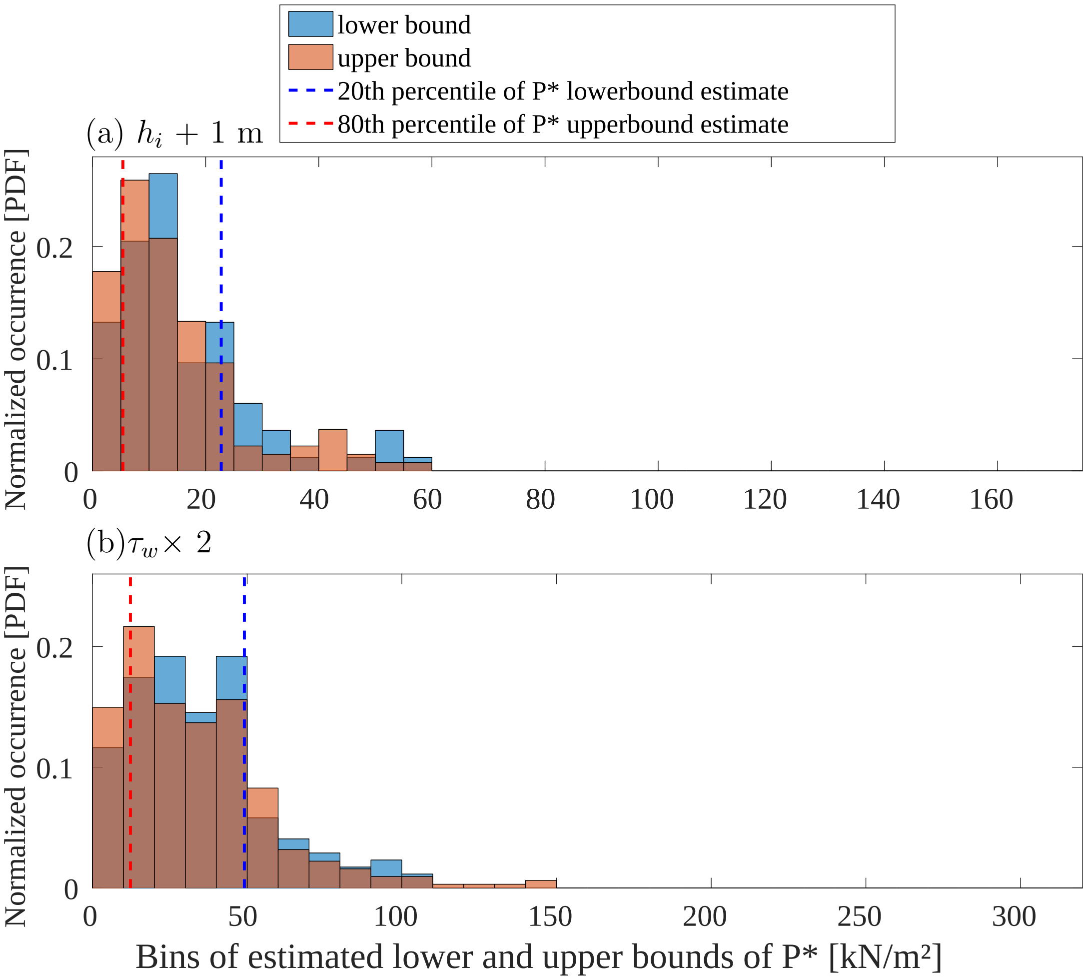

Figure 4.17: Histograms of lower (blue) and upper (red) bounds estimates of sea-ice compressive strength (P^*) for the time window covering three weeks before and one week after the landlock onset (i.e. transitional period) of MC09. The same as Figure 4.13 b, except using (a) the ice thickness increased by 1 m, and (b) the tide amplitude is increased by a factor of two from the amplitude derived from the 2014 RIOPS data. Note that the range of the bins have been changed in panel (a).

Centre for Medium-Range Weather Forecasts Reanalysis (ERA-Interim)) for different location and time, and estimating P^* with the same method with the wind data from the different reanalysis.

4.6 Conclusion, and future work

In this project, we attempt to derive the geophysical scale compressive strength of sea ice from buoy measurements made in the Canadian Arctic Archipelago (CAA). To this end, we estimate the force balance on sea ice using surface wind stresses from reanalysis data, basal ice-ocean stresses from a coupled ice-ocean model (which includes tides) forced with the same reanalysis data, and an estimate of the sea-ice thickness from a 1D thermodynamic model also forced with the same reanalysis. In order to test the method, we first calculate the force balance using diagnostics from the fully coupled ice-ocean model of the Regional Ice Operation Prediction System (RIOPS). Results from this proof of concept experiment show a P^* estimate of 22.0 ± 7.8 kN/m^2, in general accord with the actual P^* used in the model simulation of 27.5 (within 20 % error).

Applying the same method to buoy data from in-situ measurements, together with ice-ocean surface stresses from RIOPS and surface atmospheric field from Canadian Meteorological Center's Global Deterministic Prediction System Reforecast (CGRF), we obtain a sea-ice compressive strength estimate of 94.4 ± 8.8 kN/m^2 for one buoy drift data (MC13) collected in M'Clintock Channel in 2013-2014. For this year, the correlation between the observed ice speed and CGRF wind speed in summer is high, because little sea ice was present in the summer (i.e. few multi-year ice in winter) and MC13 drifted through a region where the correlation between ice and wind speed is high (i.e. low ocean currents and little effect from the proximity to land). Therefore, the assumptions of a uniform ice-ocean drag and no land effect are met.

The P^* estimates derived from the buoy drift data in 2007 and 2009 (MC07, MC09) lead to unphysical results, presumably due to the presence of multi-year ice in the

Channel and the associated uncertainty in ice thickness, and also due to uncertainties in ocean current and the nearby presence of land. Furthermore, the analysis raises some questions which concern errors in the wind forcing from the CGRF during the year 2008 and 2009, which could prevent an accurate estimate of the sea-ice compressive strength during those years.

In order to address these issues, future work includes a repetition of the analysis with wind products from different reanalyses (e.g. The Arctic System Reanalysis [ARS], The Modern-Era Retrospective Analysis for Research and Applications [MERRA], National Energy Research Supercomputing Center of the Department of Energy [NCEP-DOE] Reanalysis 2, European Centre for Medium-Range Weather Forecasts Reanalysis [ERA-Interim]). The CGRF wind and estimated ocean currents should then be replaced by 3-hourly RIOPS wind and ocean currents. Note that the 3-hourly RIOPS data are not currently available and will be produced. Further investigations of the cause of very late landlock onset observed in 2009 (MC09), together with the data that demonstrate that another buoy just a few kilometres away (but in a region of weaker tidal currents) observed landlock onset earlier, may allow us to narrow the range of the P^* estimate.

Chapter 5

Conclusion

5.1 Summary

In this thesis, I present analyses of in-situ observations with the buoys deployed in the Canadian Arctic Archipelago (CAA) from two types of sea-ice buoy: an Ice Stress Buoy (ISB) and a Surface Velocity Profilers (SVP). The ISB recorded sea-ice internal stress for ten month from 10 October 2013 TO 17 August 2014. The data was used to identify the source of internal stress in the CAA and is presented in Chapter 2. The predominant source of internal stresses are induced by changes in surface air temperature in the CAA. The thermal stresses are anisotropic after the ice become landlocked on 18 January 2011 — in contrast with previous studies in which the thermal stresses are assumed to be isotropic. We developed a 1.5D model to simulate thermal stresses taking into account land confinement. The model simulations are in good agreement with observations. It is presented in Chapter 3. Each three SVP recorded the position for 15 to 20 months; the sea-ice drift is derived from the half-hourly or three-hourly position data. The observed sea-ice velocity is used to estimate the geophysical scale sea-ice strength parameter and presented in Chapter 4. The three SVP recorded the position for 15 to 20 months; the sea-ice drift is derived from the half-hourly or three-hourly position data. This work lays the foundation for a three-dimensional ice dynamics model that considers both thermal and dynamic stresses.

In Chapter 2, we perform a correlation analysis on the stress data with wind speed and air temperature, and separate the total internal stress into thermal stress and dynamic stress. We find that the dominant source of internal stress observed by the buoy in the Viscount Melville Sound is thermally induced. Also, we observe dynamic stresses much less frequently in the CAA than in the Arctic Ocean. The observed thermal stresses in the CAA are as large as the dynamic stress, and can potentially cause or trigger sea-ice deformation/motion. We also demonstrate that thermal stress in sea ice in the CAA during the landfast season has an anisotropic character. To the best of our knowledge, this is the first time that anisotropic thermal stresses have been reported in sea ice.

From the stress angle data, we also conclude that the cause of the anisotropy in landlocked sea-ice stress is land confinement. The compressive stress is larger in the direction normal to the coastline than in the direction parallel to the coastline when the air temperature increases. Furthermore, the viscous behaviour of sea ice is observed in the residual stresses measured at the end of the seasonal cycle in temperature when it returns to 0 °C, with residual compressive stress that relaxes to near zero after eight days: the viscous relaxation time scale.

The correlation between air temperature and the maximum and minimum principal stresses are -0.76 and -0.63, respectively. The correlation is maximum with a 26-hour time lag. This suggests that the time scale required for the heat from the atmosphere to reach the stress sensor at a depth of 55 cm is about one day. Even the difference between the maximum and minimum principal stresses, which indicates the anisotropy in internal stress, correlates with air temperature. The direction of the minimum principal stress (maximum compressive stress) is perpendicular to the coastline when warming occurs, and is parallel to the coastline when the cooling occurs. This suggests that the anisotropy in thermal stress is caused by land confinement. The fact that the anisotropy in thermal stress is so large implies that thermal stresses should be considered in future, in order to accurately predict the deformation of sea ice and landfast ice break up in the CAA. We argue that the development of a model that includes internal thermal stresses is required to accurately predict landfast ice onset and break up in the CAA.

In Chapter 3, we present a 1.5D anisotropic sigma-coordinate thermal stress model of landlocked sea ice in the CAA. This model is designed to simulate thermal stresses in landlocked sea ice. In this model, the sea-ice strain perpendicular to the long axis of the channel is set to zero. This boundary condition leads to anisotropy in the thermal stresses with larger stresses in the direction perpendicular to the long axis of the channel. From this, we can surmise that when the ice expands or contracts in a channel, given that the aspect ratio of the channel is large, the presence of the land will be felt more strongly perpendicular to the long axis of the channel. For this reason, during cooling events, land will prevent ice from shrinking and will induce larger tensile stresses in that direction. The model is forced with in-situ observed air temperature from the ice stress buoy in the Viscount Melville Sound in the CAA. The result matches well with the observation. The root mean square errors in the major and minor principal stresses between the simulation and the observation are both $\sim 15\%$ of total stresses.

The simulated difference between principal stresses (i.e. anisotropic thermal stress induced with land confinement) is also in good general agreement with the observations. The error does not increase significantly as long as a minimum of one and three layers of snow and ice are used in the 1D thermodynamic model. This implies that the vertical resolution of current models is sufficient to include thermal stresses. The model sensitivity to snow depth is high, and including the temperature dependence in Young's modulus improves the model results when very rapid temperature changes are present. These sensitivity studies highlight the importance of properly simulated snow depth over sea ice and temperature dependence of the sea-ice physical properties.

In Chapter 4, we estimate the sea-ice geophysical compressive strength from the critical loads acting on sea ice during the time of landlock onset in M'Clintock Channel in the CAA. The observed sea-ice velocity is used to distinguish between plastic or viscous deformation in a standard viscous-plastic (VP) sea-ice model. When the ice velocity is non-zero, compressive sea-ice failure (e.g. ridging) occurs in the domain where the maximum compressive sea-ice strength is reached and ridging is present; when the ice velocity is zero, no compressive failure occurs. Therefore, we can associate non-zero ice velocity with plastic regime, and zero ice velocity with viscous regime in compression. The observed sea-ice velocity data from three sea-ice buoys are presented and used to derive estimates of the compressive strength of sea ice based on the observations. Two out of three buoy drift data give unphysical estimates of P^* due to errors in wind forcing and uncertainties in ice-ocean basal stresses. A successful result provides an estimate of sea-ice compressive strength parameter (P^*) of 94.4 ± 8.8 kN/m^2. This is much larger than the value commonly used in the sea-ice models ($P^* = 27.5$ kN/m^2). To verify this result and obtain reliable estimation of P^*, more observations are needed.

5.2 Future work

From the results presented in this thesis, we suggest that thermal stress should be included in sea-ice dynamic-thermodynamic models. The sea-ice internal stress we observe in the CAA demonstrates that thermal stress is as important as dynamics stresses, and that the thermal stress can have an important impact on the sea-ice dynamics model simulations (see Chapter 2). We develop a 1.5D thermal stress model that takes into account the land confinement that causes anisotropic thermal stresses in a channel (see Chapter 3). We propose adding this 1.5D thermal stress model to an existing sea-ice model in order to improve the simulation of sea-ice motion. This would require the development of a new yield criterion based on the vertically varying internal stresses (both dynamic and thermal) in sea ice. This will be achieved by adjusting the strengths and comparing the simulated drift with observed ice drift and/or strain rates (e.g. the RADARSAT Geophysical Processor System (RGPS)). We expect that the derived sea-ice strengths will be closer to the value obtained from the laboratory experiments [e.g. *Cox et al.*, 1984], which are, in general, much higher than the effective strength used commonly in the sea-ice models. For example, the sea-ice compressive strength often used in the sea-ice models is 27.5 kN/m^2, while the laboratory experiments derive the compressive strength value of more than 700 kN/m^2 [e.g. *Cox et al.*, 1984].

Finally, future work includes a parameterization of the sea-ice strength with respect to sea-ice temperature. Previous experiments in the field by *Johnston* [2006] illustrate a reduction in the sea-ice borehole strength caused by warming. Johnston's findings – that ice porosity increase is the primary cause of the sea-ice weakening during warming period – are relevant to our work going forward. To parameterize the sea-ice strength with respect to ice temperature, we first need observations from different ice temperature environments. The observations needed for this purpose include ice velocity, and temperature when the ice concentration is close to one. The observations of air and ice temperatures, ice thickness, wind and ocean current velocity, as well as, sea-ice speed are also necessary for an estimation of sea-ice strength. Using those observations, together with the method presented in Chapter 4, will allow for a parameterization of sea-ice strength based on temperature.

Appendix A

Estimating thin ice onset from the fading of inertial oscillations from sea-ice motion

A.1 Motivation

Satellite or aircraft ice thickness products have accuracy ranging from 20 cm [APP-x, *Key et al.*, 2016] to 10 cm [SMOS, CryoSat-2, *Tian-Kunze et al.*, 2014; *Laxon et al.*, 2013], depending on products. Should the sea ice that is thinner than the accuracy of the satellite and aircraft products is detected and input to an operational system, the timing when the sea ice reaches the critical thicknesses for shipping, hunting platform, and other activities, could be forecasted more accurately with longer lead times. Thus, redeeming the existing satellite and aircraft ice thickness products regarding detecting thin sea ice with an alternative scheme is useful.

To this end, we suggest the methodology that estimating the timing of thin ice (∼5 cm) onset from the observed ice drift in this chapter. In the following, we show that the inertial oscillation can be observed in the sea-ice drift until the minimum sea-ice thickness reaches 5 cm. Using this criteria, we demonstrate estimating the timing of thin ice onset from observed sea-ice velocity in M'Clintock Channel and Viscount

Melville Sound in the CAA from 2008 to 2013 with the SVP.

A.2 Method

We use the time when the ice transitions from a drift with inertial oscillation to a drift without inertial oscillation to estimate the timing of thin ice (~ 5 cm) onset during fall in the CAA. Note that the force balance in the y-direction is one order of magnitude smaller than in the x-direction. The uncertainty in the forcing, therefore, prevents us to calculate a compressive strength estimate. Instead, we use a similar force balance as described in Section 4.3 to infer the timing of thin sea-ice onset (~ 2 cm), when the pack ice transits from a drift with to without inertial Oscillations (IO).

The force balance in the y-direction (perpendicular to the channel long axis) can be written as:

$$\rho_i h_I \frac{\partial v_i}{\partial t} = \rho_i h_I f u_i + \frac{\partial \sigma_{22}}{\partial y} = 0, \tag{A.1}$$

or

$$\frac{\partial \sigma_{22}}{\partial y} = -\rho_i h_I f u_i, \tag{A.2}$$

where σ_{22} is the normal stress on a plain along the channel long axis, ρ_i is sea-ice density, h_I is the mean ice thickness (~ 1 m, figure 4.4 c, around the time observes sea-ice motion), u_i and v_i are x- and y-components of sea-ice velocity, and f is the Coriolis parameter. We assume above that the wind and ocean drags, and the acceleration term in the y-direction are negligible. Integrating equation (A.2) from one coastline ($y = 0$) to the other ($y = L_y$), we obtain:

$$\sigma_{22}(y = L_y) = \rho_i h_I f u_i L_y, \tag{A.3}$$

assuming $\sigma_{22}(y = 0) = 0$. When inertial oscillation are present in the sea-ice drift, sea ice must deform (plastically) to accommodate the nearly-circular motion. For a Viscous-Plastic (VP) sea-ice model, the normal stress σ_{22} resisting such motion can be parameterized as $P^* h_i e^{[-C(1-A_i)]}$ [*Hibler*, 1979], where P^* is sea-ice compressive strength parameter, h_i is the thin ice thickness, C is the ice concentration parameter ($= 20$), and A_i is sea-ice concentration. I.e. $\sigma_{22} > P^* h_i e^{[-C(1-A_i)]}$. When inertial oscillations are not present in the sea-ice drift, the internal sea-ice stresses prevent such motion and $\sigma_{22} < P^* h_i e^{[-C(1-A_i)]}$. Therefore, we rewrite Eq. (A.3) as:

$$\begin{cases} P^* h_i e^{[-C(1-A)]} < \rho_i h_I f u_i L_y, \text{ when inertial signals are present in ice drift,} & \text{(A.4a)} \\ P^* h_i e^{[-C(1-A)]} > \rho_i h_I f u_i L_y, \text{ when no inertial signal is present in ice drift,} & \text{(A.4b)} \end{cases}$$

where h_i is the thin ice thickness, and h_I (~ 1 m, figure 4.4**c** around the time observes sea-ice motion) is the mean ice thickness. We can rewrite the above equations as,

$$\begin{cases} h_i > \dfrac{\rho_i h_I f u_i L_y}{P^*}, \text{ when inertial signals are present in the ice drift,} & \text{(A.5a)} \\ h_i < \dfrac{\rho_i h_I f u_i L_y}{P^*}, \text{ when no inertial signals are present in the ice drift,} & \text{(A.5b)} \end{cases}$$

when we assume ice concentration is approximately 100 %. The simple scale analysis of above equation shows that $O(\frac{\rho_i h_I f u_i L_y}{P^*}) \approx 2 \times 10^{-2}$, therefore $O(h_i) \approx 2 \times 10^{-2}$ m or 2 cm. From the timing when inertial oscillations are no longer present in the sea-ice drift field, we can estimate the onset of thin ($\sim$ 2cm) ice on open water, which otherwise is difficult to detect using satellite data.

A.3 Results

The sea-ice drift observed with the SVPs show the inertial oscillation in M'Clintock Channel and in the east of Viscount Melville Sound (see Figure 4.1). The frequency of inertial oscillation is $\sim$ 12.4 hr at the latitude of 75° N. This frequency is comparable to the frequency of the semidiurnal tide of 12.7 hr. Thus, looking simply the $\sim$ 12-hr frequency signals in the ice velocity is not sufficient to detect inertial signals. To this end, we separate the power of signals into the clockwise and counter-clockwise components using the wavelet analysis suggested by *Liu and Miller* [1996]. The tidal signal has no rotation, i.e. the peak in power would appear in both clockwise and counter-clockwise components. The inertial signal has clockwise rotation, i.e. the peak in power would appear in only clockwise component. Thus, the presence of inertial signal can be known from the difference in the strength of power between clockwise and counter-clockwise components around the frequency of 12 hr or the period of 2 day^{-1}.

The difference in wavelet power between clockwise and counter-clockwise components at the period of 2 day^{-1} ($\Delta P_{(f=2)}$) ranges between -0.27 and +0.60. The negative value indicates that the ice velocity has counter-clockwise motion, which is presumably caused by the atmospheric forcing. The magnitude of power associated with counter-clockwise motion signals are below 0.09 excluding extreme outliers. Thus, the positive value that is smaller than 0.09 could be signal due to the atmospheric forcing. For this reason, we define the $\Delta P_{(f=2)}$ larger than 0.09 is the inertial signal.

The inertial signal presented in sea-ice velocity for average 36 days in summer. The wavelet analysis of the ice velocity observed with MC07, MC09, and MC13 show that the inertial signal died out on 19 October 2008, 13 October 2009, and 25 October 2013, respectively (see Figure A.1 c, A.2 c, A.7 c). Thus, from the three inertial signal cessation events, we estimate the timings of the thin ice onset when the the thinnest sea ice around the instrumented floe becomes around 2-cm thick are on 19 October 2008, 13 October 2009, and 25 October 2013 in M'Clintock Channel. However, the corresponding mean sea-ice concentrations derived from the gridded sea-ice concentration data of the CIS in M'Clintock channel are 9.65, 9.65, and 9.58 (see Figure 4.9e, 4.10e, and 4.11e), suggesting that the inertial oscillation cessation events may had occurred due to the stress term becomes important. We need further investigations to elaborate this to the possible method for thin ice onset.

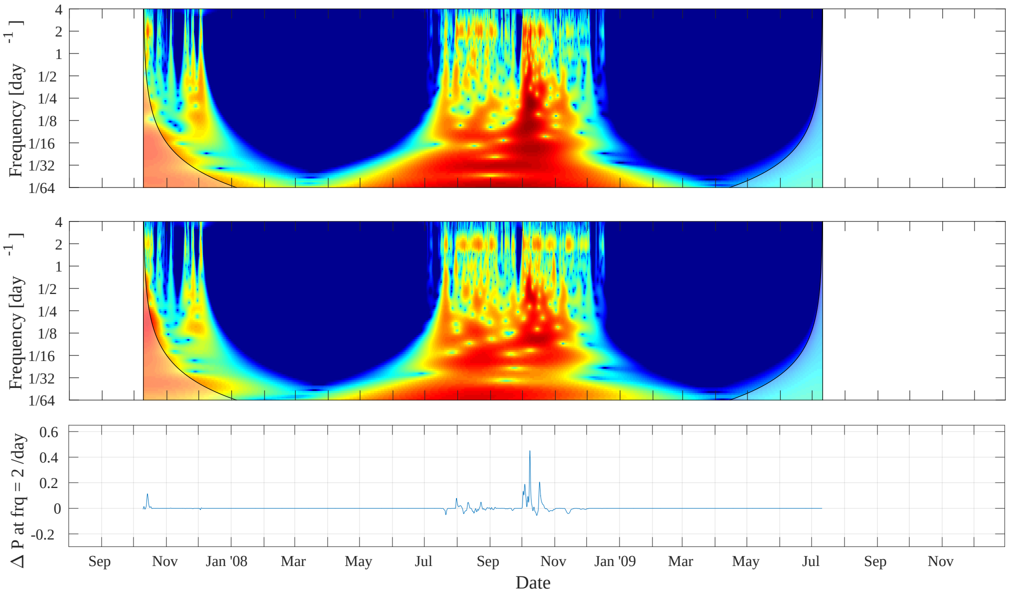
(a) clockwise

(b) counter-clockwise

(c) $\Delta P_{(f=2day^{-1})}$

Figure A.1: The (a) clockwise and (b) counter-clockwise components of the wavelet spectrum of the sea-ice velocity observed with MC07. The (c) difference in power of clockwise and counterclockwise components at the frequency of 2 day^{-1} is also shown to see when we stop observing internal oscillations in sea-ice velocity. A lighter shade in (a) and (b) shows the cone of influence subject to edge effects. The analysis is done using the method shown by *Liu and Miller* [1996].

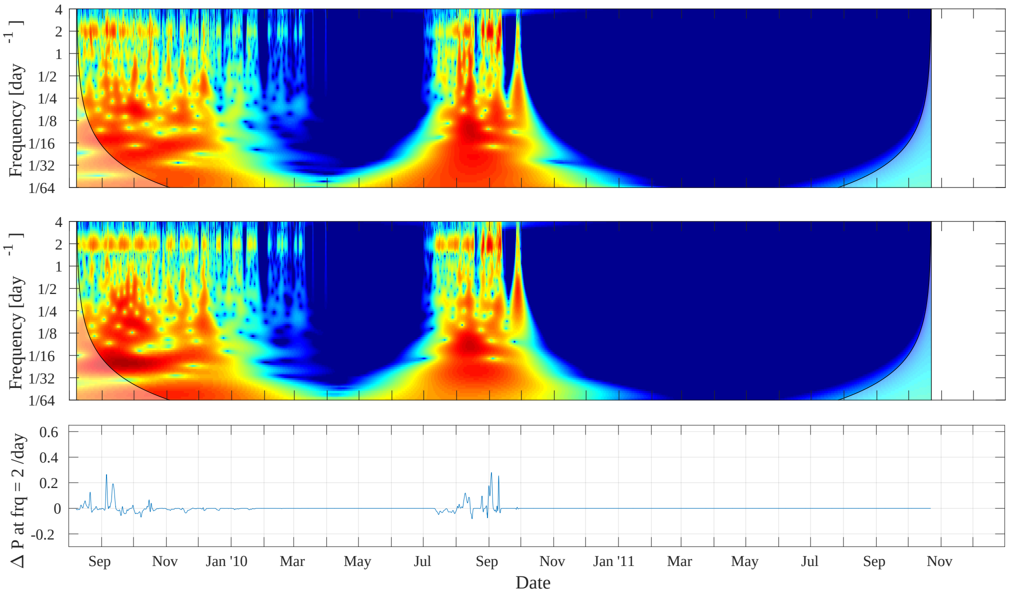
(a) clockwise

(b) counter-clockwise

(c) $\Delta P_{(f=2day^{-1})}$

Figure A.2: The same as figure A.1 except using the data obtained with MC09.

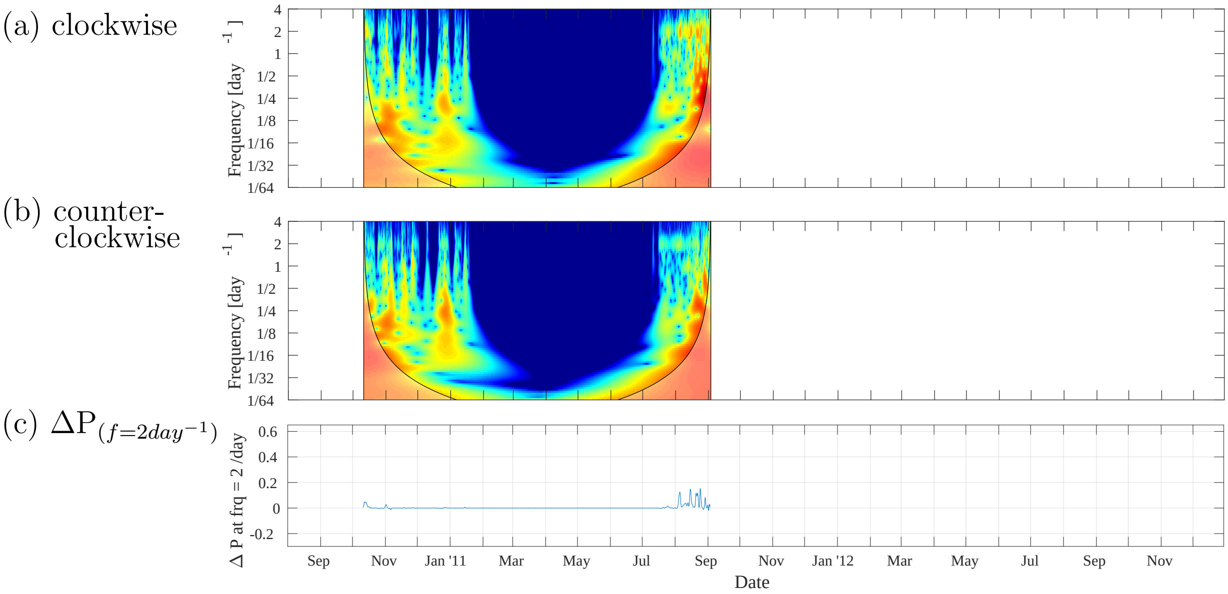

Figure A.3: The same as figure A.1 except using the data obtained with VM10.

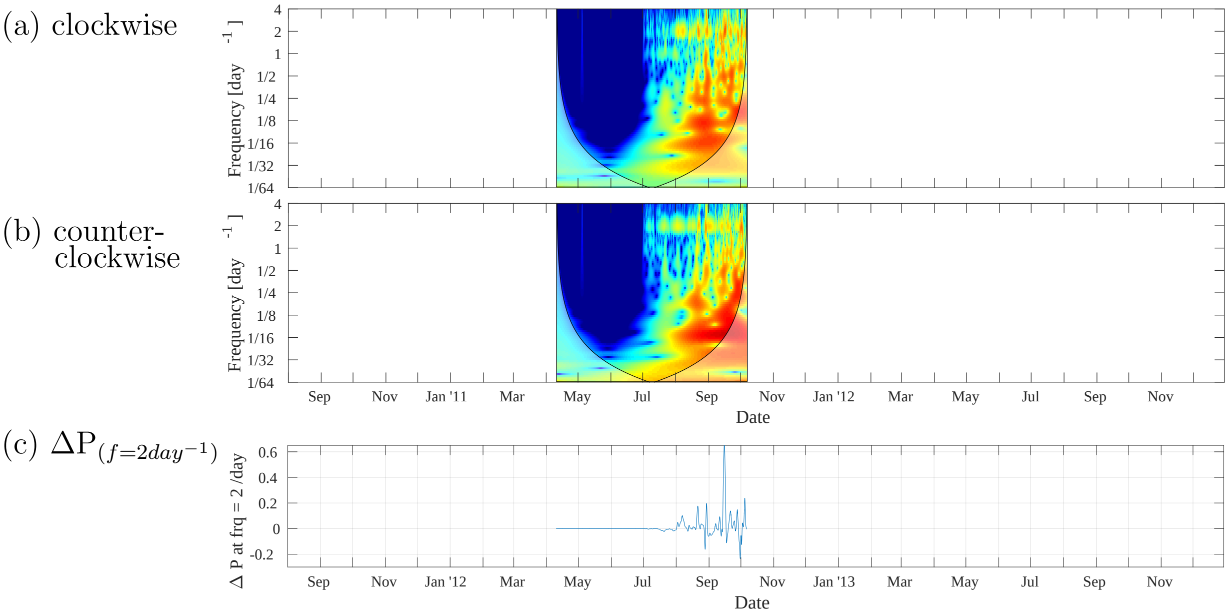

Figure A.4: The same as figure A.1 except using the data obtained with MC11.

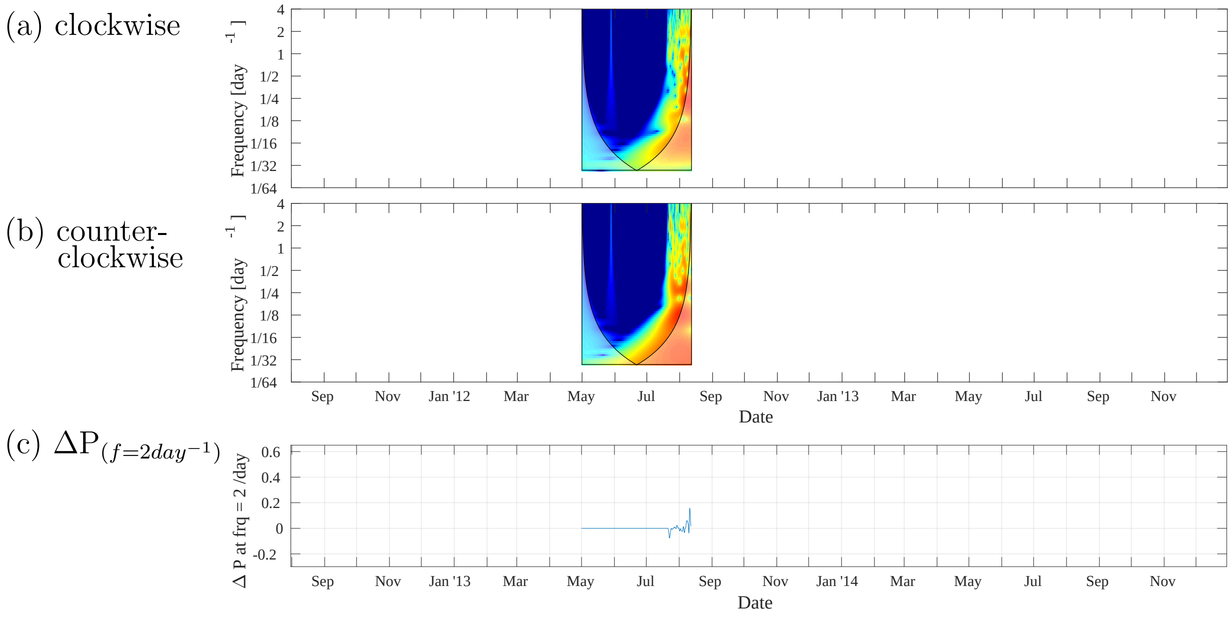

Figure A.5: The same as figure A.1 except using the data obtained with BM12.

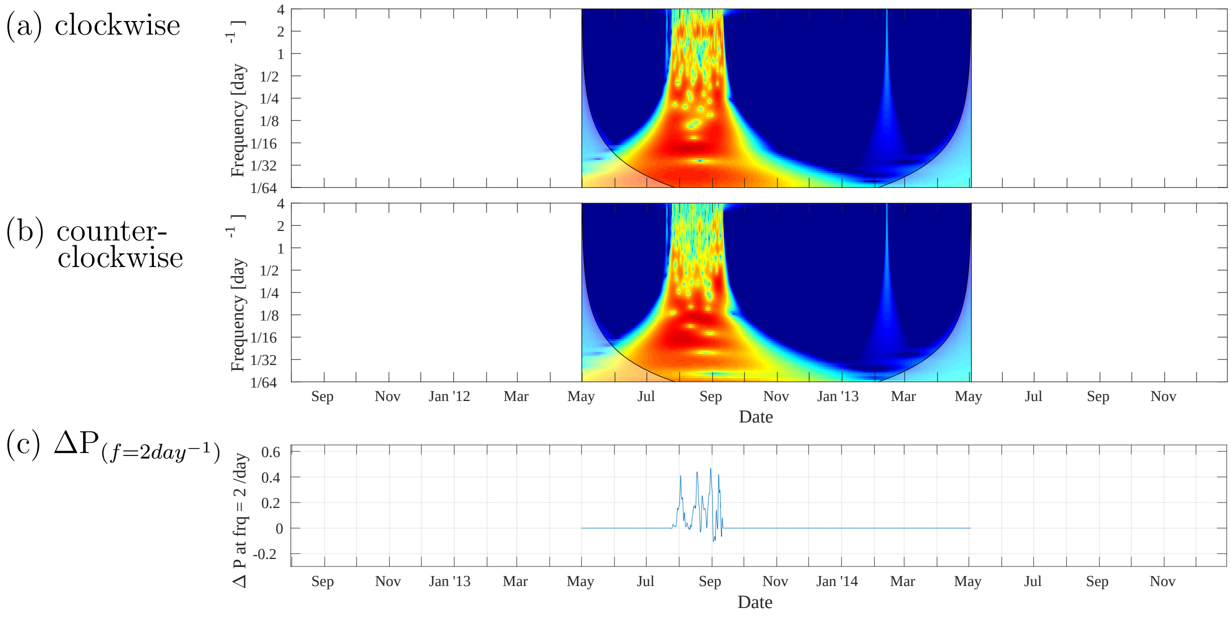

Figure A.6: The same as figure A.1 except using the data obtained with VM12.

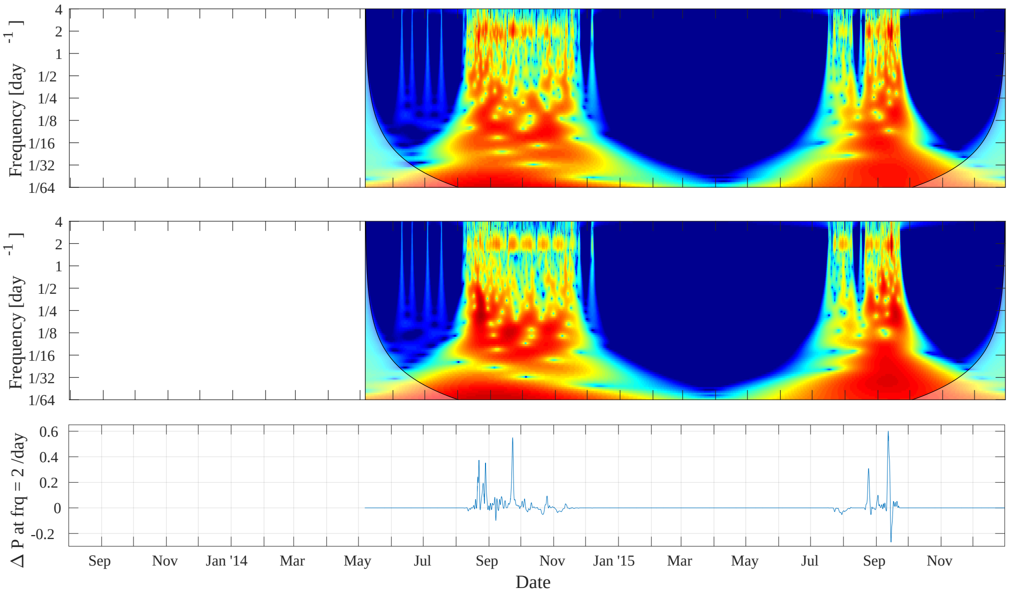

(a) clockwise

(b) counter-clockwise

(c) $\Delta\mathrm{P}_{(f=2day^{-1})}$

Figure A.7: The same as figure A.1 except using the data obtained with MC13.

Bibliography

Andreas, E. L., T. W. Horst, A. A. Grachev, P. O. G. Persson, C. W. Fairall, P. S. Guest, and R. E. Jordan (2010), Parametrizing turbulent exchange over summer sea ice and the marginal ice zone, *Quarterly Journal of the Royal Meteorological Society*, *136*(649), 927–943, doi:10.1002/qj.618.

Arrigo, K. R., D. K. Perovich, R. S. Pickart, Z. W. Brown, G. L. van Dijken, K. E. Lowry, M. M. Mills, M. A. Palmer, W. M. Balch, F. Bahr, N. R. Bates, C. Benitez-Nelson, B. Bowler, E. Brownlee, J. K. Ehn, K. E. Frey, R. Garley, S. R. Laney, L. Lubelczyk, J. Mathis, A. Matsuoka, B. G. Mitchell, G. W. K. Moore, E. Ortega-Retuerta, S. Pal, C. M. Polashenski, R. A. Reynolds, B. Schieber, H. M. Sosik, M. Stephens, and J. H. Swift (2012), Massive phytoplankton blooms under arctic sea ice, *Science*, *336*(6087), 1408–1408, doi:10.1126/science.1215065.

Barry, R., R. Moritz, and J. Rogers (1979), The fast ice regimes of the beaufort and chukchi sea coasts, alaska, *Cold Regions Science and Technology*, *1*(2), 129 – 152, doi:http://dx.doi.org/10.1016/0165-232X(79)90006-5.

Barry, R. G. (1993), Canada's cold seas, in *Canada's Cold Environment*, edited by French and O.Slaymaker, chap. 2, pp. 29–61, McGill Queen's University Press, Canada.

Bitz, C. M., and W. H. Lipscomb (1999), An energy-conserving thermodynamic model of sea ice, *Journal of Geophysical Research: Oceans*, *104*(C7), 15,669–15,677, doi: 10.1029/1999JC900100.

Bogorodsky, V. V., V. P. Gavrilo, A. V. Gusev, Z. M. Gudkovich, and A. P. Polyakov (1972), Stressed ice cover state due to thermal wave and related underwater noise in the ocean, *Proceeding Ice Symposium*, pp. 28–33.

Bouchat, A., and B. Tremblay (2017), Using sea-ice deformation fields to constrain the mechanical strength parameters of geophysical sea ice, *Journal of Geophysical Research: Oceans*, doi:10.1002/2017JC013020.

Bouillon, S., and P. Rampal (2015), Presentation of the dynamical core of nextsim, a new sea ice model, *Ocean Modelling*, *91*, 23 – 37, doi:http://dx.doi.org/10.1016/j.ocemod.2015.04.005.

Cherepanov, N. V. (1971), Spatial arrangement of sea ice crystal structure, *Probl. Arktiki Antarktiki*, *38*, 137–140.

Comfort, G., and R. Ritch (1990), Field measurement of pack ice stresses, in *Proc. 9th International Conference of Offshore Mechanics and Arctic Engineering*, pp. 177–181.

Comfort, G., R. Ritch, and R. M. W. Frederking (1992), Pack ice stress measurements, in *Proc. 11th International Conference of Offshore Mechanics and Arctic Engineering*, pp. 245–253.

Comiso, J. C. (2003), Warming trends in the arctic from clear sky satellite observations, *Journal of Climate*, *16*(21), 3498–3510, doi:10.1175/1520-0442(2003)016⟨3498:WTITAF⟩2.0.CO;2.

Coon, M., G. A. Maykut, R. S. Pritchard, D. A. Rothrok, and A. S. Thorndike (1974), Modelling the pack ice as an elastic plastic material, *AIDJEX Bulletin*, *24*, 1–105.

Coon, M., R. Kwok, G. Levy, M. Pruis, H. Schreyer, and D. Sulsky (2007), Arctic Ice Dynamics Joint Experiment (AIDJEX) assumptions revisited and found inadequate, *Journal of Geophysical Research*, *112*, C11S90, doi:10.1016/j.physd.2011.07.005.

Côté, J., S. Gravel, A. Méthot, A. Patoine, M. Roch, and A. Staniforth (1998a), The operational cmc–mrb global environmental multiscale (gem) model. part i: Design considerations and formulation, *Monthly Weather Review*, *126*(6), 1373–1395, doi: 10.1175/1520-0493(1998)126⟨1373:TOCMGE⟩2.0.CO;2.

Côté, J., J.-G. Desmarais, S. Gravel, A. Méthot, A. Patoine, M. Roch, and A. Staniforth (1998b), The operational cmc–mrb global environmental multiscale (gem) model. part ii: Results, *Monthly Weather Review*, *126*(6), 1397–1418.

Cox, G. F. (1984), A preliminary investigation of thermal ice pressures, *Cold Regions Science and Technology*, *9*, 221 – 229.

Cox, G. F. N., and J. B. Johnson (1983), Stress measurement in ice, *Tech. Rep. 83-23*, Cold Regions Research and Engineering Laboratory, Hanover, N.H.

Cox, G. F. N., J. A. Richter-Menge, W. F. Weeks, M. Mellor, and H. Bosworth (1984), Mechanical Properties of Multi-Year Sea Ice. Phase I. Test Results, *Tech. Rep. 84-9*, Cold Regions Research and Engineering Laboratory, Hanover, N.H.

Croasdale, K. R., G. Comfort, R. M. W. Frederking, B. W. Graham, and E. L. Lewis (1988), A pilot experiment to measure arctic pack-ice driving forces, in *Proc. 9th International Conference on Port and Ocean Engineering under Arctic Conditions*, pp. 381–395.

Curry, J. A., J. L. Schramm, and E. Ebert (1994), Sea ice-albedo climate feedback mechanism, *Journal of Climate*, *8*(2), 240–247.

Evans, R. J., and N. Untersteiner (1971), Thermal Cracks in Floating Ice Sheets, *Journal of Geophysical Research*, *76*(3), 694–703.

Fissel, D., J. Birch, H. Melling, and R. A. Lake (1988), Non-tidal flows in the northwest passage, in *Canadian technical report of hydrography and ocean sciences*, Department of Fisheries and Oceans, Sidney, BC, Canada.

George, J. C. C., H. P. Huntington, K. Brewster, H. Eicken, D. W. Norton, and R. Glenn (2004), Observations on shorefast ice dynamics in Arctic Alaska and the responses of the Iñupiat hunting community, *Arctic*, *57*(4), 363–374.

Gimbert, F., D. Marsan, J. Weiss, N. C. Jourdain, and B. Barnier (2012), Sea ice inertial oscillations in the Arctic Basin, *The Cryosphere*, *6*(5), 1187–1201.

Girard, L., S. Bouillon, J. Weiss, D. Amutrano, T. Fichefet, and V. Legat (2011a), A new modeling framework for sea-ice mechanics based on elasto-brittle rheology, *Ann. Glaciol.*, *52*(57).

Girard, L., S. Bouillon, J. Weiss, D. Amutrano, T. Fichefet, and V. Legat (2011b), A new modeling framework for sea-ice mechanics based on elasto-brittle rheology, *Annals of Glaciology*, *52*(57), 123–132.

Greversen, R. G., T. Mauritsen, M. Tjernstróm, E. Källén, and G. Svensson (2008), Vertical structure of recent Arctic warming, *Nature*, *541*, doi:10.1038/nature06502.

Haas, C., W. Dierking, T. Busche, and J. Hölemann (2005), Envisat asar monitoring of polynya processes and sea ice production in the laptev sea, in *Proceedings, ESA Envisat Symposium, Salzburg, September 2004*.

Hata, Y., and L. B. Tremblay (2015a), Anisotropic internal thermal stress in sea ice from the canadian arctic archipelago, *Journal of Geophysical Research: Oceans*, *120*(8), 5457–5472, doi:10.1002/2015JC010819.

Hata, Y., and L. B. Tremblay (2015b), A 1.5-d anisotropic sigma-coordinate thermal stress model of landlocked sea ice in the canadian arctic archipelago, *Journal of Geophysical Research: Oceans*, *120*(12), 8251–8269, doi:10.1002/2015JC010820.

Hibler, W. D., III (1977), A viscous sea ice law as a stochastic average of plasticity, *Journal of Geophysical Research*, *82*(27), 3932–3938.

Hibler, W. D., III (1979), A dynamic sea ice model, *Journal of Physical Oceanography*, *9*, 815–846.

Holloway, G., and A. Proshutinsky (2007), Role of tides in Arctic ocean/ice climate, *Journal of Geophysical Research: Oceans*, *112*(C4), n/a–n/a, doi:10.1029/2006JC003643.

Howell, S. E. L., T. Wohlleben, M. Dabboor, C. Derksen, A. Komarov, and L. Pizzolato (2013), Recent changes in the exchange of sea ice between the arctic ocean and the canadian arctic archipelago, *Journal of Geophysical Research: Oceans*, *118*(7), 3595–3607, doi:10.1002/jgrc.20265.

Hunke, E., and W. Lipscomb (2008), *Cice: The los alamos sea ice model, documentation and software user's manual, version 4.0*, Los Alamos National Laboratory Tech, Los Alamos, N. M.

Hunke, E. C. (2014), Sea ice volume and age: Sensitivity to physical parameterizations and thickness resolution in the {CICE} sea ice model , *Ocean Modelling*, *82*, 45 – 59, doi:10.1016/j.ocemod.2014.08.001.

Hunke, E. C., and J. K. Dukowicz (1997), An elastic-viscous-plastic model for sea ice dynamics, *Journal of Physical Oceanography*, *27*, 1849–1867.

Hunke, E. C., W. H. Lipscomb, A. K. Turner, N. Jeffery, and S. Elliott (2013), *CICE: the Los Alamos Sea Ice Model Documentation and Software User's Manual Version 5.0 LA-CC-06-012*.

Hutchings, J. K., C. Geiger, A. Roberts, J. Richter-menge, and B. Elder (2010), On the Spatial and Temporal Characterization of Motion Induced Sea Ice Internal Stress, in *International Conference and Exhibition on Performance of Ships and Structures in Ice*, pp. 1–8.

Huwald, H., L. B. Tremblay, and H. Blatter (2005), A multilayer sigma-coordinate thermodynamic sea ice model: validation against Surface Heat Budget of the Arctic Ocean (SHEBA)/Sea Ice Model Intercomparison Project Part 2 (SIMIP2) data, *Journal of Geophysical Research*, *110*, C05010, doi:10.1029/2004JC002328.

Itkin, P., M. Losch, and R. Gerdes (2015), Landfast ice affects the stability of the arctic halocline: Evidence from a numerical model, *Journal of Geophysical Research: Oceans*, *120*(4), 2622–2635, doi:10.1002/2014JC010353.

Ji, S.-Y., A.-L. Wang, J. Su, and Q.-J. Yue (2011), Experimental studies on elastic modulus and flexural strength of sea ice in the Bohai sea, *Journal of Cold Regions Engineering*, *25*(4), 182–195, doi:10.1061/(ASCE)CR.1943-5495.0000035.

Johnson, J. B., and R. C. Metzner (1990), Thermal expansion coefficients for sea ice, *Journal of Glaciology*, *36*(124), 343 – 349.

Johnston, M. (2006), A comparison of physical properties and strength of decaying first-year ice in the Arctic and sub-Arctic, *Annals of Glaciology*, *44*, 154–162, doi:10.3189/172756406781811664.

Key, J., X. Wang, Y. Liu, R. Dworak, and A. Letterly (2016), The avhrr polar pathfinder climate data records, *Remote Sensing*, *8*(3), doi:10.3390/rs8030167.

König Beatty, C., and D. M. Holland (2010), Modeling landfast sea ice by adding tensile strength, *Journal of Physical Oceanography*, *40*, 185–198, doi:10.1175/2009JPO4105.1.

Kovacs, A., and R. M. Morey (1978), Radar anisotropy of sea ice due to preferred azimuthal orientation of the horizontal c axes of ice crystals, *Journal of Geophysical Research*, *83*(C12), 6037 –6046.

Kwok, R., G. Spreen, and S. Pang (2013), Arctic sea ice circulation and drift speed: Decadal trends and ocean currents, *Journal of Geophysical Research: Oceans*, *118*(5), 2408–2425, doi:10.1002/jgrc.20191.

Laxon, S. W., K. A. Giles, A. L. Ridout, D. J. Wingham, R. Willatt, R. Cullen, R. Kwok, A. Schweiger, J. Zhang, C. Haas, S. Hendricks, R. Krishfield, N. Kurtz, S. Farrell, and M. Davidson (2013), Cryosat-2 estimates of arctic sea ice thickness and volume, *Geophysical Research Letters*, *40*(4), 732–737, doi:10.1002/grl.50193.

Lemieux, J.-F., and B. Tremblay (2009), Numerical convergence of viscous-plastic sea ice models, *Journal of Geophysical Research*, *114*, C05009, doi:10.1029/2008JC005017.

Lemieux, J.-F., B. Tremblay, S. Thomas, J. Sedláček, and L. A. Mysak (2008), Using the preconditioned Generalized Minimum RESidual (GMRES) method to solve the sea-ice momentum equation, *Journal of Geophysical Research*, *113*, C10004, doi:10.1029/2007JC004680.

Lemieux, J.-F., B. Tremblay, J. Sedláček, P. Tupper, S. Thomas, D. Huard, and J.-P. Auclair (2010), Improving the numerical convergence of viscous-plastic sea ice models with the Jacobian-free Newton–Krylov method, *Journal of Computational Physics*, *229*(8), 2840–2852, doi:10.1016/j.jcp.2009.12.011.

Lemieux, J.-F., L. B. Tremblay, F. Dupont, M. Plante, G. C. Smith, and D. Dumont (2015), A basal stress parameterization for modeling landfast ice, *Journal of Geophysical Research: Oceans*, *120*(4), 3157–3173, doi:10.1002/2014JC010678.

Lemieux, J.-F., C. Beaudoin, F. Dupont, F. Roy, G. C. Smith, A. Shlyaeva, M. Buehner, A. Caya, J. Chen, T. Carrieres, L. Pogson, P. DeRepentigny, A. Plante, P. Pestieau, P. Pellerin, H. Ritchie, G. Garric, and N. Ferry (2016), The regional ice prediction system (rips): verification of forecast sea ice concentration, *Quarterly Journal of the Royal Meteorological Society*, *142*(695), 632–643, doi:10.1002/qj.2526.

Lewis, J. K. (1993), A model for thermally-induced stresses in multi-year sea ice, *Cold Regions Science and Technology*, *21*, 337–348.

Lewis, J. K. (1995), A conceptual model of the impact of flaws on the stress state of sea ice, *Journal of Geophysical Research: Oceans*, *100*(C5), 8829–8835, doi:10.1029/95JC00686.

Lewis, J. K., and J. A. Richter-Menge (1998), Motion-induced stresses in pack ice, *Journal of Geophysical Research*, *103*(C10), 21,831, doi:10.1029/98JC01262.

Lewis, J. K., W. B. Tucker, III, and P. J. Stein (1994), Observations and modeling of thermally induced stresses in first-year sea ice, *Journal of Geophysical Research*, *99*(C8), 16,361–16,371, doi:10.1029/94JC01242.

Liu, P. C., and G. S. Miller (1996), Wavelet transforms and ocean current data analysis, *Journal of Atmospheric and Oceanic Technology*, *13*(5), 1090–1099.

Macdonald, R. W., D. W. Paten, E. C. Carmack, and A. Omstedt (1995), The freshwater budget and under-ice spreading of Mackenzie River water in the Canadian Beaufort Sea based on salinity and $^{18}O/^{16}O$ mearsurements in water and ice, *Journal of Geophysical Research*, *100*(C1), 895–919, doi:10.1029/94JC02700.

Mahoney, A., H. Eicken, A. G. Gaylord, and L. Shapiro (2007), Alaska landfast sea ice: Links with bathymetry and atmospheric circulation, *Journal of Geophysical Research*, *112*, C02001, doi:10.1029/2006JC003559.

Manabe, S., and R. J. Stouffer (1996), Low-frequency variability of surface air temperature in a 1000-year integration of a coupled atmosphere-ocean-land surface model, *Journal of Climate*, *9*(2), 376–393, doi:10.1175/1520-0442(1996)009⟨0376:LFVOSA⟩2.0.CO;2.

McPhee, M. G. (1975), Ice-ocean momentum transfer for the AIDJEX ice model, *AIDJEX Bulletin*, *29*, 93–111.

Melling, H. (2002), Sea ice of the northern Canadian Arctic Archipelago, *Journal of Geophysical Research*, *107*(C11), 3181, doi:10.1029/2001JC001102.

Miller, P. A., S. W. Laxon, and D. L. Feltham (2005), Improving the spatial distribution of modeled Arctic sea ice thickness, *Geophysical Research Letters*, *32*(18), L18,503, doi:10.1029/2005GL023622.

Milne, A. R. (1972), Thermal tension cracking in sea ice: A source of underice noise, *Journal of Geophysical Research*, *77*(12), 2177–2192, doi:10.1029/JC077i012p02177.

Olason, E. (2016), A dynamical model of kara sea land-fast ice, *Journal of Geophysical Research: Oceans*, *121*(5), 3141–3158, doi:10.1002/2016JC011638.

Overland, J. E., and M. Wang (2009), Large-scale atmospheric circulation changes are associated with the recent loss of arctic sea ice, *Tellus A*, *62*(1), 1–9, doi:10.1111/j.1600-0870.2009.00421.x.

Parsons, B. L., J. B. Snellen, and B. Hill (1986), *Physical modeling and the fracture toughness of sea ice*, Institute for Marine Dynamics.

Prinsenberg, S., and R. Pettipas (2008), Ice and ocean mooring data statistics from Barrow Strait, central section of NW passage in Canadian Arctic Archipelago, *Internat. J. Offshore Polar Engineering*, *18*, 277–281.

Pritchard, R. S. (1976), An estimate of the strength of Arctic pack ice, *AIDJEX bull.*, *34*, 94–113.

Reimnitz, E., D. Dethleff, and D. Nürnberg (1994), Contrasts in Arctic shelf sea-ice regimes and some implications :Beaufort Sea versus Laptiv Sea, *Marine Geology*, *119*, 215–225.

Richter-Menge, J. A. (1997), Towards improving the physical basis for ice-dynamics models, *Annals of Glaciology*, *25*, 177–182.

Richter-Menge, J. A., and B. C. Elder (1998), Characteristics of pack ice stress in the Alaskan Beaufort Sea, *Journal of Geophysical Reserch*, *103*(C10), 21,817–21,829, doi:10.1029/98JC01261.

Richter-Menge, J. A., D. K. Perovich, and S. W. Pegau (2001), Summer ice dynamics during sheba and its effect on the ocean heat content, *Annals of Glaciology*, *33*(1), 201–206.

Richter-Menge, J. A., S. L. McNutt, J. E. Overland, and R. Kwok (2002a), Relating arctic pack ice stress and deformation under winter conditions, *Journal of Geophysical Research*, *107*(C10), 8040, doi:10.1029/2000JC000477.

Richter-Menge, J. A., B. Elder, J. Overland, and S. Salo (2002b), In situ sea ice stresses in the western Arctic during the winter of 2001 —2002, in *Proceedings of the 16th IAHR International Symposium on Ice*, vol. 2, p. 423–430.

Samelson, R. M., and P. L. Barbour (2008), Low-level jets, orographic effects, and extreme events in nares strait: A model-based mesoscale climatology, *Monthly Weather Review*, *136*(12), 4746–4759, doi:10.1175/2007MWR2326.1.

Schmidt, G., C. Bitz, U. Mikolajewicz, and L. Tremblay (2004), Ice–ocean boundary conditions for coupled models, *Ocean Modelling*, *7*(12), 59 – 74.

Schmith, T., and C. Hansen (2003), Fram strait ice export during the nineteenth and twentieth centuries reconstructed from a multiyear sea ice index from southwestern greenland, *Journal of Climate*, *16*(16), 2782–2791, doi:10.1175/1520-0442(2003) 016⟨2782:FSIEDT⟩2.0.CO;2.

Schulson, E. M. (1999), The structure and mechanical behavior of ice, *The Journal of The Minerals, Metals and Materials Society*, *51*, 21–27.

Screen, J. A., and I. Simmonds (2010), The central role of diminishing sea ice in recent Arctic temperature amplification , *Nature*, *464*, doi:10.1038/nature09051.

Screen, J. A., I. Simmonds, C. Deser, and R. Tomas (2013), The atmospheric response to three decades of observed arctic sea ice loss, *Journal of Climate*, *26*(4), 1230–1248, doi:10.1175/JCLI-D-12-00063.1.

Selyuzhenok, V., T. Krumpen, A. Mahoney, M. Janout, and R. Gerdes (2015), Seasonal and interannual variability of fast ice extent in the southeastern laptev sea between 1999 and 2013, *Journal of Geophysical Research: Oceans*, *120*(12), 7791–7806, doi: 10.1002/2015JC011135.

Smith, G. C., F. Roy, P. Mann, F. Dupont, B. Brasnett, J.-F. Lemieux, S. Laroche, and S. Bélair (2013), A new atmospheric dataset for forcing ice-ocean models: Evaluation of reforecasts using the Canadian global deterministic prediction system, *Quarterly Journal of the Royal Meteorological Society*, doi:10.1002/qj.2194.

Smith, G. C., F. Roy, M. Reszka, D. Surcel Colan, Z. He, D. Deacu, J.-M. Belanger, S. Skachko, Y. Liu, F. Dupont, J.-F. Lemieux, C. Beaudoin, B. Tranchant, M. Drévillon, G. Garric, C.-E. Testut, J.-M. Lellouche, P. Pellerin, H. Ritchie, Y. Lu, F. Davidson, M. Buehner, A. Caya, and M. Lajoie (2016), Sea ice forecast verification in the canadian global ice ocean prediction system, *Quarterly Journal of the Royal Meteorological Society*, *142*(695), 659–671, doi:10.1002/qj.2555.

Sou, T., and G. Flato (2009), Sea ice in the Canadian Arctic Archipelago: Modeling the past (1950-2004) and the future (2041-60), *Journal of Climate*, *22*(8), 2181–2198, doi:10.1175/2008JCLI2335.1.

Stander, E. D., and M. Bernard (1989), The development of aligned columnar sea ice: a field investigation, *Journal of Glaciology*, *35*(120).

Stephen E. L., H., T. Adrienne, Y. John J., and M. Steve (2008), Multi-year sea-ice conditions in the western canadian arctic archipelago region of the northwest passage: 1968-2006, *Atmosphere-Ocean*, *46*(2), 229–242, doi:10.3137/ao.460203.

Stewart, E., S. Howell, D. Draper, J. Yackel, and A. Tivy (2009), Sea ice in canada's arctic: Implications for cruise tourism, *ARCTIC*, *60*(4), 370–380, doi:10.14430/arctic194.

Strum, M., D. K. Perovich, and J. Holmgren (2002), Thermal conductivity and heat transfer through the snow on the ice of the beaufort sea, *Journal of Geophysical Research*, *107*(C21), doi:10.1029/2000JC000409.

Sukhorukov, K. (1996), Experimental investigations of relaxation properties of sea ice internal stresses, in *Proc. 6th International Offshore and Polar Enginnering Conference*, vol. III, pp. 354–361.

Sulsky, D., and L. Schreyer (2004), MPM simulation of dynamic material failure with a decohesion constitutive model, *European Journal of Mechanics - A/Solids*, *23*, 423–445, doi:10.1016/j.euromechsol.2004.02.007.

Tian-Kunze, X., L. Kaleschke, N. Maaß, M. Mäkynen, N. Serra, M. Drusch, and T. Krumpen (2014), Smos-derived thin sea ice thickness: algorithm baseline, product specifications and initial verification, *The Cryosphere*, *8*(3), 997–1018, doi:10.5194/tc-8-997-2014.

Timco, G., and W. Weeks (2010), A review of the engineering properties of sea ice, *Cold Regions Science and Technology*, *60*, 107–129, doi:10.1016/j.coldregions.2009.10.003.

Timco, G. W., and M. E. Johnston (2002), Sea ice strength during the melt season, in *Proceedings of 16th IAHR International Symposium on Ice.*

Timco, G. W., and S. O'Brien (1994), Flexural strength equation of sea ice, *Cold Reg. Sci. Technol.*, *22*.

Tremblay, L. B. (1996), Modelling Sea Ice as a Granular Material, with Applications to Climate Variability, Ph.D. thesis, McGill Univ., Montreal, Canada.

Tremblay, L. B., and M. Hakakian (2006), Estimating the sea ice compressive strength from satellite-derived sea ice drift and NCEP reanalysis Data*, *Journal of Physical Oceanography*, *36*(11), 2165–2172, doi:10.1175/JPO2954.1.

Tremblay, L.-B., and L. A. Mysak (1997), Modeling sea ice as a granular material, including the dilatancy effect, *Journal of Physical Oceanography*, *27*(11), 2342–2360, doi:10.1175/1520-0485(1997)027⟨2342:MSIAAG⟩2.0.CO;2.

Tsamados, M., D. L. Feltham, and A. V. Wilchinsky (2013), Impact of a new anisotropic rheology on simulations of arctic sea ice, *Journal of Geophysical Research: Oceans*, *118*(1), 91–107, doi:10.1029/2012JC007990.

Tsamados, M., D. L. Feltham, D. Schroeder, D. Flocco, S. L. Farrell, N. Kurtz, S. W. Laxon, and S. Bacon (2014), Impact of Variable Atmospheric and Oceanic Form Drag on Simulations of Arctic Sea Ice*, *Journal of Physical Oceanography*, *44*, doi: 10.1175/JPO-D-13-0215.1.

Tucker, W. B., A. J. Gow, and W. F. Weeks (1987), Physical properties of summer sea ice in the fram strait, *Journal of Geophysical Research: Oceans*, *92*(C7), 6787–6803, doi:10.1029/JC092iC07p06787.

Tucker, W. B., III, and D. K. Perovich (1992), Stress measurements in drifting pack ice, *Cold Regions Science and Technology*, *20*, 119–139, doi:10.1016/0165-232X(92)90012-J.

Tynan, C. T., and D. P. DeMaster (1997), Observations and predictions of Arctic climatic change : Potential effects on marine mammals, *Arctic*, *50*(4), 308–322.

Uttal, T., J. A. Curry, M. G. Mcphee, D. K. Perovich, R. E. Moritz, J. A. Maslanik, P. S. Guest, H. L. Stern, J. A. Moore, R. Turenne, A. Heiberg, M. C. Serreze, D. P. Wylie, O. G. Persson, C. A. Paulson, C. Halle, J. H. Morison, P. A. Wheeler, A. Makshtas, H. Welch, M. D. Shupe, J. M. Intrieri, K. Stamnes, R. W. Lindsey, R. Pinkel, W. S. Pegau, T. P. Stanton, and T. C. Grenfeld (2002), Surface Heat Budget of the Arctic Ocean, *Bull. American Meteorological Society*, *83*(February), 255–276.

Wang, Q., P. G. Myers, X. Hu, and A. B. Bush (2012), Flow Constraints on Pathways through the Canadian Arctic Archipelago, *Atmosphere-Ocean*, *50*(3), 373–385, doi: 10.1080/07055900.2012.704348.

Warren, S. G., I. G. Rigor, N. N. B. Vladimir F. Radionov, Y. I. Aleksandrov, and R. Colony (1999), Snow depth on arctic sea ice, *J. Climate*, *12*, 1814 – 1829.

Weeks, W. F., and A. Assur (1967), The Mechanical Properties of Sea Ice, *Tech. Rep. II-C3*, Cold Regions Research and Engineering Laboratory, Hanover, N.H.

Weeks, W. F., and A. J. Gow (1978), Preferred crystal orientations in the fast ice along the margins of the Arctic Ocean, *Journal of Geophysical Research*, *83*(C10), 5105–5121, doi:10.1029/JC083iC10p05105.

Weeks, W. F., and A. J. Gow (1980), Crystal alignments in the fast ice of Arctic Alaska, *Journal of Geophysical Research*, *85*(C2), 1137–1146, doi:10.1029/JC085iC02p01137.

Weiss, J., E. M. Schulson, and H. L. Stern (2007), Sea ice rheology from in-situ, satellite and laboratory observations: Fracture and friction, *Earth and Planetary Science Letters*, *255*, 1–8, doi:10.1016/j.epsl.2006.11.033.

Wilchinsky, A. V., and D. L. Feltham (2006), Anisotropic model for granulated sea ice dynamics, *Journal of the Mechanics and Physics of Solids*, *54*(6), 1147–1185, doi:10.1016/j.jmps.2005.12.006.

Xie, Y., and D. M. Farmer (1991), Acoustical radiation from thermally stressed sea ice, *Journal of Acoustical Society of America*, *89*(5), 2215 – 2231.

Yu, Y., H. Stern, C. Fowler, F. Fetterer, and J. Maslanik (2014), Interannual variability of arctic landfast ice between 1976 and 2007, *Journal of Climate*, *27*(1), 227–243, doi:10.1175/JCLI-D-13-00178.1.

Zhang, J., and W. D. Hibler, III (1997), On an efficient numerical method for modeling sea ice dynamics, *Journal of Geophysical Research*, *102*(C4), 8691–8702, doi:10.1029/96JC03744.